The Dissertation Committee for Aiting Jiang Certifies that this is the approved version of the following dissertation:

Widely Tunable Terahertz Semiconductor Laser Sources

Committee:

Mikhail A. Belkin, Supervisor

Deji Akinwande

Seth R. Bank

Edward T. Yu

Alexey Belyanin

Widely Tunable Terahertz Semiconductor Laser Sources

by

Aiting Jiang, B.S.; M.S.E

Dissertation

Presented to the Faculty of the Graduate School of

The University of Texas at Austin

in Partial Fulfillment

of the Requirements

for the Degree of

Doctor of Philosophy

The University of Texas at Austin

December 2015

Dedication

To my parents

Acknowledgements

First I want to thank my mother Zhiling Mao and my father Qianlin Jiang for their never ending support. I am blessed to have them in my life.

I would like to give my sincere gratitude to my supervisor, Prof. Mikhail Belkin, for his excellent guidance, caring and patience. His broad knowledge and sharp intuition are the strongest support throughout my research. I have learned enormously from him on both research and personal development as a researcher.

I would like to thank Prof. Edward Yu, Prof. Seth Bank, Prof. Deji Akinwande, and Prof. Alexey Belyanin for serving on my dissertation committee and giving constructive comments. Special thanks to Prof. Belyanin for his useful suggestion on my research.

I appreciate the intensive support on simulation and material growth from our collaborators: Prof. Christian Jirauschek at the Technical University Munich, Prof. Zbigniew Wasilewski at University of Waterloo and Prof. Edmund Linfield at Leeds University. Thank Alpar Matyas for taking care of the EMC simulation and patiently responding my endless questions.

I am grateful to our group members for their training and help in the cleanroom and in the testing lab, especially, Karun Vijayraghavan, Seungyong Jung, Feng Lu, Yifan Jiang, and Jae Hyun Kim. My gratitude also goes to my friends in the MRC building who shared their resources with me: Jingsi Li, Chengqing Hu, Xiaochuan Xu…

Thank Prof. Sanjay Banerjee and our MRC staff for maintaining this cleanroom. Bill Ostler is always willing to help with cleanroom tool issues. Minor issues are usually

cleared quickly so that our processing can go smoothly without too much delay. Also I need to thank Christine Wood for her kind help on administrative issues.

Finally, I want to acknowledge research funding support from National Science Foundation.

Widely Tunable Terahertz Semiconductor Laser Sources

Aiting Jiang, Ph.D.

The University of Texas at Austin, 2015

Supervisor: Mikhail A. Belkin

Terahertz Quantum Cascade Lasers (THz QCLs) and Terahertz Difference Frequency Generation Quantum Cascade Laser sources (DFG-QCLs) are two types of semiconductor THz radiation sources that are compact and amenable to production in mass quantities. THz QCL can generate over 1W of power under cryogenic temperatures, while THz DFG-QCL can be operated under room temperature over 1mW level output. For either case, widely tunable solution is highly desired for spectroscopy applications.

For THz QCLs, operation is still limited to cryogenic temperature and broad tuning is not available. Our experimental study shows that using variable barriers is a viable approach to enhance the design space for THz QCLs. We also propose to tune the spectral output of these devices using an optically projected variable distributed feedback grating. Tuning will be achieved by changing the projected grating period. Preliminary experimental results support the idea but higher pumping light intensity is required for this method to work.

For THz DFG-QCLs, very broad tuning in 1-6 THz range has been demonstrated using rotating diffraction grating in an external cavity setup. Similar tuning range can also be achieved in a monolithic configuration. Based on the previous work which demonstrated an electrical monolithic tuner with 580 GHz tuning range, we design and test in this dissertation a linear array of 10 DFG-QCL devices to cover a 2 THz tuning

range. An independent gain control scheme is developed to achieve high yield (~100%) of individual device. It is implemented via independent current pumping of two electrically isolated sections.

Surface DFB grating and independent current pumping scheme used in our DFG QCLs is found to be useful for mid-IR QCL array sources. We propose a longitudinal integration scheme of multiple grating sections. It enables a single ridge to emit single mode radiation at different wavelengths upon selection. This helps to reduce mid-IR QCL array far field span. We demonstrated single ridge devices that can emit 2 or 3 different wavelengths upon selection.

Table of Contents

List of Tables

List of Figures

Chapter 1: Introduction

1.1 Terahertz Spectral Range

The Terahertz (THz) spectral range is defined as the band of frequencies from 1 THz to 10 THz in the electromagnetic spectrum. It may also be referred to as far-infrared range. This spectral range has its unique features, however, has long been relatively unexplored, in particular due to the lack of compact and convenient radiation sources. As a result, it is often being referred to as the "THz Gap" in the literature (Fig. 1.1).

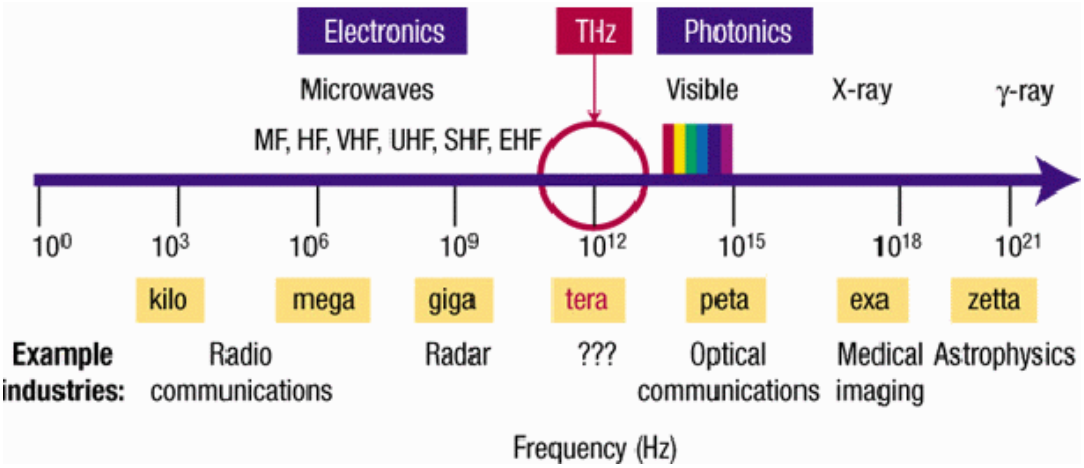

Figure 1.1, The "THz Gap" in the electromagnetic spectrum

Due to its unique features, a multitude of applications exist for THz radiation. THz spectroscopy (imaging) is the most promising one. Many materials exhibit characteristic spectral features in the THz frequency range due to the fact that many molecules have strong rotational and vibrational absorption features in the THz range (particularly, between 1 and 5 THz). THz radiation can also excite intermolecular vibrations. Therefore THz spectroscopy possesses the potential to provide both chemical and structural information thereby identifying chemical/biological substance. On the

other hand, THz radiation has another attractive property of being transmissive for many nonpolar and nonmetallic materials, which allows noninvasive and nondestructive analysis. A lot of applications of THz radiation have been demonstrated: 1) From a security screening point of view, THz imaging system could be used to detect concealed weapon, explosives and drugs.[1] Moreover, stand-off scanning of people with THz wave instead of X-Ray poses no health risk for human body as THz radiation is nonionizing. 2) For medical market, THz has large potential. THz imaging provides good contrast between different types of tissues, and is a sensitive means of detecting cancerous tissues or other diseases.[2] Dentist would like to use THz instead of X-ray for imaging.[3] THz pharma applications include crystalline structure analysis of drugs, solid dosage analysis of tablets etc.[4] 3) THz imaging could be applied in manufacturing industry for fault isolation, defect detection and other quality control purposes.[5, 6] 4) In astronomy, THz spectral range is critical for our understanding of the composition and origin of the solar system, the evolution of matter in our Galaxy, and the star formation history of galaxies over cosmic timescale.[7] 5) THz spectroscopy is also relevant in condensed matter physics to study collective effects in materials such as superconductors. 6) THz wave is also a candidate for outer space communication between satellites with the benefit of higher bandwidth.[8]

1.2 TERAHERTZ SEMICONDUCTOR SOURCE AND TUNABILITY

Research on THz radiation sources, detectors and components has been ongoing for decades to enable THz technologies. Sensitive THz detectors such as liquid helium cooled bolometer have been existed since 1960s. What hinders the development of THz technology is the lack of convenient coherent sources.

Currently, the spectral range 1-5 THz remains one of the least developed spectral regions. Within this range, there currently exists no room temperature THz sources analogous to a diode laser in near-infrared and visible, i.e., compact, inexpensive, broadly-tunable, and suitable for a production in large quantities. As shown in Fig. 1.1, electromagnetic sources are either electronic based or photonic based. Electronics dominates the low frequency end while photonic devices take the high frequency end. Both of them have difficulties to be extended to THz region. On the microwave side of the spectrum, the power generated by solid-state electronic devices, such as transistors, Schottky diode multipliers, and Gunn oscillators, rolls off with frequency owing to transit-time and resistance-capacitance effects. As a result, the available power generated above 2 THz is well below the milliwatt level.[9-11] On the optical side of the spectrum, interband diode lasers have long been designed for operation at visible and near-IR frequencies. Emission wavelength of interband device is determined by material bandgap and cannot be extended to THz since no suitable narrow bandgap material is available. Other photonic devices generating THz radiation at room temperature are limited to optically-pumped gas lasers, free-electron lasers, and frequency down-conversion systems that produce THz radiation from infrared or visible light using difference-frequency generation, parametric down-conversion, or photoconductive switching. [12-16] Free electron lasers and gas lasers are bulky and complex. THz sources based on difference-frequency generation have achieved considerable progress recently with over 1mW of continuous-wave THz output at RT.[15, 16] However, these table-top systems are based on externally-pumped nonlinear crystals and even the most compact ones[15] cannot be compared in terms of miniaturization and suitability of mass production to electrically-pumped semiconductor lasers.

First breakthrough on semiconductor laser type compact source occurred in 1994[17]: Mid-IR Quantum Cascade Laser was invented to break the constraint from material bandgap through using intersubband transition instead of interband transition. This concept was later successfully extended to THz region. In 2002, first THz QCL was demonstrated by Kohler et al. [18], with a peak power up to 2mW at 4.4THz and maximum operating temperature (T_{max}) up to 50K. After a decade of development, spectral coverage has been demonstrated from 0.84–5.0 THz, at maximum temperatures up to 199.5K[19], pulsed, and 117K[20], c.w., and output powers of up to 1W[21], pulsed, and 130mW[22], continuous wave. Current goal is to improve T_{max} to thermoelectric cooler accessible temperature which is around 240K.

On the other hand, since THz QCLs are currently constrained to cryogenic operating temperatures, effort has been made to achieve room temperature semiconductor THz radiation source based on alternative principles. Difference-frequency generation quantum cascade laser (DFG QCL) was demonstrated in 2007 by Beklin et al[23]. THz radiation is generated inside of the mid-infrared QCL cavity by difference frequency mixing between two mid-infrared beams. In contrast to THz QCL, this nonlinear mechanism is not limited to cryogenic temperatures[24]. By introducing Cherenkov phase-matching[25], Belkin group has managed to dramatically improve the performance of these devices[26] to achieve over 0.1 mW of peak power output at room temperature. Recently, Razeghi group used the same technology with improved growth and processing capability to produce devices with 3μW of THz power in continuous-wave and 1.4mW of peak THz power in pulsed operation at room temperature. [27]

To enable application of these sources for THz spectroscopy, a broad tunability, preferably over the entire 1-5 THz range and beyond, is a desired feature for a THz sources. Currently, tuning range of THz QCL is still limited to ~330 GHz[28] and that

tuning is achieved at cryogenic temperatures using a sophisticated MEMS system. For THz DFG-QCLs, nearly 5 THz of tuning from 1 to 6 THz has already been demonstrated[29] using a (bulky) external cavity setup. Both types of sources have drawbacks as convenient spectroscopy sources and require improvement.

1.3 ORGANIZATION OF DISSERTATION

This thesis reports our work on: improving the temperature performance of THz QCLs, exploring the feasibility of broadly tuning a THz QCL via an external optical pumping method, demonstrating high yield THz DFG QCL array to cover a wide spectral range and closely related mid-IR QCL array work.

Chapter 2 starts with the fundamentals of Quantum Cascade Lasers and then reports our work on improving THz QCL T_{max} by introducing variable barrier height active region design. Our results demonstrate that variable barrier heights designs provide a viable alternative to the traditional active region designs with fixed barrier composition. In the fourth section of this chapter, our effort on expanding tuning range of THz QCL is reviewed. We explored a new method based on external optical illumination, which potentially has no limit on tuning range. Although tuning has not been demonstrated yet, future improvement is expected to eventually achieve tuning.

In Chapter 3, we first explain working principles of THz DFG-QCL. Physics of giant nonlinearity and Cherenkov phase matching will be presented. Then a monolithic DFG-QCL device with ~600 GHz electrical tuning will be shown as building block for our array solution. An independent current pumping method is implemented to improve the yield of individual THz DFG QCL devices. A 10-device array continuously tunable from ~1.9 THz to ~3.9 THz was demonstrated with almost 100% individual device yield.

Chapter 4 describes an idea inspired by our THz DFG QCL results. High yield of our DFG QCL devices could be primarily attributed to the implementation of surface DFB grating and independent current pumping scheme. Wavelength selection mechanism of surface DFB grating is clarified in this chapter. Design procedure of a surface grating is also discussed. Results of THz DFG QCL also show the possibility of emitting different mid-IR light from a single device ridge upon selection. Longitudinal integration scheme of mid-IR QCLs is proposed. Proof-of-principle device is demonstrated.

Chapter 2: Widely Tunable Terahertz Quantum Cascade Laser

THz QCL was first demonstrated in 2002.[18] After a decade of development, the maximum operating temperature (T_{max}) of Terahertz (THz) Quantum Cascade Lasers (QCLs) has been improved from 50K[18] to a current record of 199.5K.[19] Current goal is to push T_{max} further towards temperatures accessible by thermoelectric coolers (~240K) or even higher. On the other hand, broadly tunable THz QCL with cryocooling is still not available. In this chapter, fundamentals of THz QCLs will be presented first. Then our work on THz QCL active region with variable barrier height trying to improve the T_{max} further will be reviewed. We also explored a new method expected to achieve widely tunable high power THz sources based on THz QCLs.

2.1 Quantum Cascade Laser Background

Quantum Cascade Laser (QCL) was first demonstrated in 1994[17] to extend emission wavelength of semiconductor laser to longer wavelength. Before the advent of QCL, semiconductor laser wavelength was essentially determined by material bandgap hence limited by the availability of narrow bandgap material system. Lasers based on lead salt and HgCdTe are able to generate light up to ~6μm under cryogenic temperatures.[30] QCL was invented with a completely different operating principle: intersubband transition as compare to the interband transition for laser diode. QCL now

A portion of this work has been published in A. Jiang, A. Matyas, K. Vijayraghavan, C. Jirauschek, Z. R. Wasilewski and M. A. Belkin, "Experimental investigation of terahertz quantum cascade laser with variable barrier heights," Journal of Applied Physics 115(16), 163103 (2014). A. J. performed device processing, measurement and experiment data analysis. K.V. helped with measurement setup. A. M. and C. J. performed simulation. Z. R. W. performed wafer growth. M. A. B. supervised the project.

can cover a wide wavelength range from ~3μm to ~24μm and from ~60μm to ~300μm, especially with room temperature operation capability in mid-IR range.

2.1.1 Intersubband transition vs. interband transition

Traditional laser diodes are based on recombination of electrons in the conduction band and holes in the valence band as shown in Fig. 2.1(a) (from left to right: spatial band diagram, k-space band diagram, joint density of states and gain spectrum). Transition energy is determined by bandgap E_g with small tuning capability by changing the quantum well width. The joint density of states is constant for a quantum well as plotted on the right. The gain spectrum is broad due to different k space dispersion for conduction and valence band.

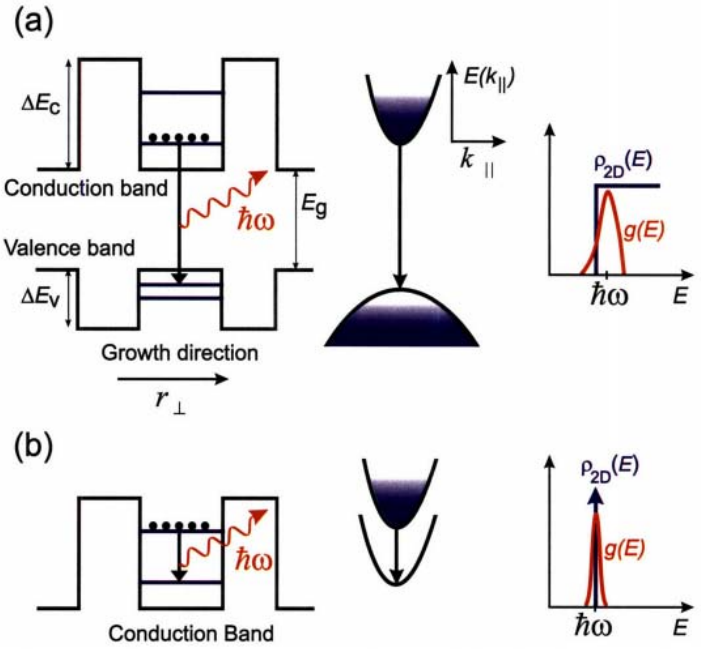

Figure 2.1, Schematic showing (a) interband, and (b) intersubband transition in quantum wells. Left: spatial band diagram; Middle: k- space subband diagram; Right: joint density of state ρ and gain g versus transition energy E. Adapted from: Ref. [31]

In contrast to the interband semiconductor laser, laser emission in QCLs is achieved through the use of intersubband transitions within conduction band (or valence band) as shown in Fig. 2.1(b). Separations between subbands are essentially determined by the width of the quantum well with a theoretical maximum of conduction band offset ΔE_c and a minimum of a few meV which covers the entire mid-IR to THz range. Lasing should be possible if population inversion could be established between the desired subband.

It can be seen from Fig. 2.1(b) that due to the almost same energy dispersion of each of the subbands, the joint density of states hence the gain spectrum is delta-function like for such transition, which suggest a potentially very high gain. However, this feature is diluted by the fact that non-radiative lifetimes for intersuband transition are very short (~1ps) as compared to its interband counterparts (~1ns),[31] mostly due to the longitudinal-optical (LO) phonon scattering. As a result, limited population inversion could be achieved for intersubband transition. To achieve enough gain, multiple modules is needed.

Regarding the material to construct the quantum well structure, III-V semiconductor heterostructure are exclusively used for QCL due to its maturity and flexibility. III-V heterostructures are grown either by Molecular Beam Epitaxy (MBE) or Metal Organic Vapor Phase Epitaxy (MOVPE). Two III-V material systems are predominantly used, InGaAs/InAlAs on InP substrates and AlGaAs/GaAs on GaAs substrates. InGaAs/InAlAs system has a large conduction band offset and is best for mid-IR QCL while AlGaAs/GaAs system is primarily used for THz QCL.

2.1.2 Carrier Transport: Cascade Laser

To achieve population inversion, a pumping or injection scheme is needed. For diode lasers, this is achieved within the depletion region of a pn junction where electrons and holes are injected from opposite sides and then recombine. Intersubband transition is a unipolar process and requires different mechanism for carrier transport. As mentioned before, multiple modules are needed to generate reasonable gain for intersubband transition. Carrier transport in a periodic superlattice with repeating quantum wells or more complicated modules are illustrated in Fig. 2.2. Electrons traverse the entire region through a combination of intersubband transition and quantum tunneling through thin barriers. This is the origin of terminology "quantum cascade laser".

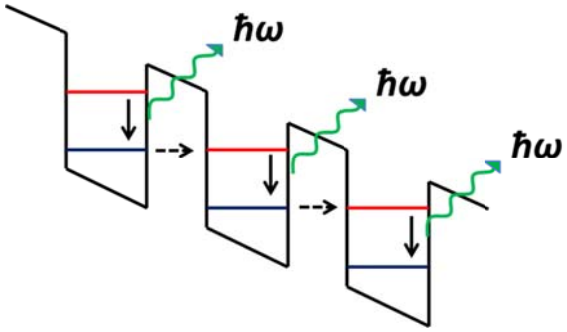

Figure 2.2, Conduction band diagram showing carrier transport in a periodic superlattice: intersubband transition and resonant tunneling. The squiggly arrows represent photon emission and the dashed arrows represent tunneling between quantum wells.

A periodic quantum well structure was first proposed for optical gain generation in 1971.[32] However, this type of laser was not realized until 1990s. The biggest problem that prevents it from practical implementation is the negative differential resistance (NDR) region of its I-V characteristics as shown in Fig. 2.3. NDR is a result of discreet energy level and resonant tunneling. Current pass through the structure peaks at perfect alignment condition and drops as detuned from alignment which leads to an NDR region

(from V_2 to V_3 in Fig. 2.3). An NDR region is inherently unstable for a periodic structure since it will break down into high field domains.

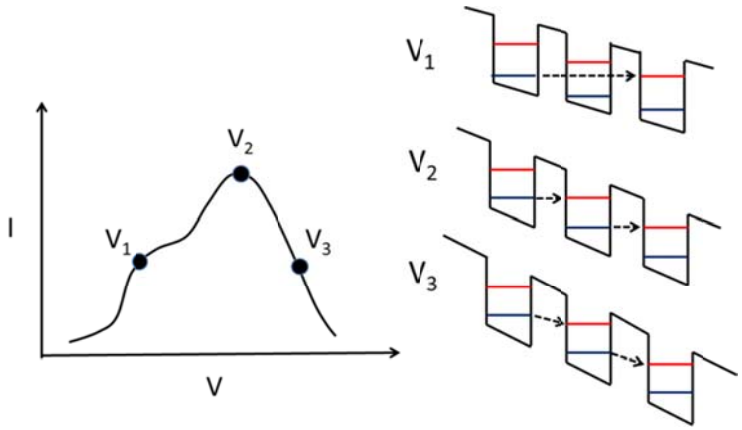

Figure 2.3, Schematic illustrating the origin of NDR in a periodic quantum well structure. Conduction band diagrams on the right correspond to bias conditions indicated on the left.

The first QCL was demonstrated in 1994 by introducing a section termed "injector" to avoid NDR problem.[17] As shown in Fig. 2.4, each active region, where radiative transitions take place, is separated by a doped digitally graded superlattice, in which energy levels are quasi continuous. This injector region eliminates discrete energy alignment conditions in order to prevent NDR before design bias and to enforce a uniform field through the structure. With this innovation, stable electrical pumping becomes possible.

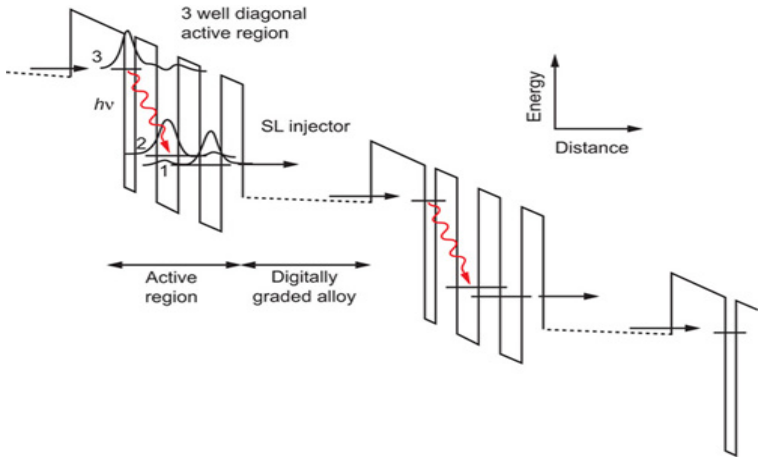

Figure 2.4, Conduction band diagram and electron wavefunction for the first QCL under bias. The squiggly lines represent photon emission. Adapted from Ref. [31]

2.1.3 Population Inversion: Fast Depopulation of Lower Lasing State

As mentioned before, non-radiative interssubband transition lifetime is short on the order of ps. To achieve population inversion, one solution is to use a 3-level lasing system and introduce a fast depopulation process to minimize the lower lasing state lifetime. This could be achieve by resonant LO phonon scattering. As shown in Fig. 2.4, E_{21} is designed to be equal to LO-phonon energy $\hbar\omega_{LO}$~34meV at design bias condition, while $E_{32} >> \hbar\omega_{LO}$ (for mid-IR range only). Consequently, life time τ_3 (~2-5ps) is an order of magnitude greater than τ_2 (~0.2-0.5ps), so that population inversion could be achieved between level 3 and level 2. Bound to continuum design based on scattering within sub-miniband is another depopulation scheme and will be addressed later.

To summarize QCL operation can be understood as a 3-level system shown in Fig. 2.4. Carriers are injected to the upper lasing level 3 through tunneling from injector. Population inversion is achieved by quick depopulation of carriers from lower lasing level 2 to level 1, employing ultrafast electron scattering by optical phonons. At the end

of each stage, carriers are extracted by resonant tunneling to an injector section and then reinjected into next stage. First QCL was demonstrated based on this principle and subsequent improvements are essentially variations and optimizations of this 3-level lasing design. QCL now has accomplished a great success in mid-IR range. Commercial products with room temperature continuous wave operation capability are available for a wide range in mid-IR spectrum. In this chapter, our topic focuses on the THz QCL, which has similar working principle but is not equally successful as its mid-IR counterpart due to some limitations.

2.2 TERAHERTZ QUANTUM CASCADE LASER OVERVIEW

THz QCL was first demonstrated in 2002[18], about 8 years after the invention of mid-IR QCL. Demonstrating long-wavelength QCL is considerably more difficult than the mid-IR for two reasons.

First, because THz photon energies are small (<20 meV), it is difficult to achieve the population inversion necessary for gain. The spacing between level 3 and level 2 in Fig. 2.4 is so small that various scattering process such as electron-electron scattering, interface roughness scattering etc. are activated and tend to even out population inversion that could be achieved. Also, small spacing make selective injection of carriers to upper state difficult. Resonant tunneling has a large possibility to inject carriers to lower lasing states, which is not desired. Additionally, rapid depopulation process will be efficient for both level 2 and 3 hence degrade population inversion. Therefore, active region design has to be optimized to minimize these adverse effects. Moreover, as will be shown later, temperature has to be kept low to obtain population inversion

Besides the active region design, THz waveguide design is equally challenging. In THz range, material loss increases compared to mid-IR range. GaAs based material has significantly lower material loss then InP based material. This is why THz QCLs are mostly made with GaAs. Another primary loss is free carrier loss, which increases proportionally to the square of the wavelength and is much higher compared to mid-IR range. Moreover, THz wavelength increases by a factor of ten relative to mid-IR while the material growth thickness cannot be scaled accordingly. Innovative waveguides are required that minimize the modal overlap with any doped semiconductor cladding layers and tightly confine THz mode within the active region.

To overcome these challenges, three types of THz QCL active region designs and two types of THz waveguides were created to realize THz lasing. Nevertheless, even with these innovations, the highest lasing temperature is still below 200K.

2.2.1 THz QCL Active Region Design

Three types of active regions have been developed for THz QCL (Fig. 2.5). THz QCL active region is grown using GaAs/AlGaAs material system because of its low conduction band offset and low material loss.

Chirped superlattice (CSL) is the structure used in the first THz QCL. It relies on the coupling of several quantum wells to form minibands. Analogous to energy bands in semiconductor, electrons tend to relax to the bottom of the minibands through interminiband scattering. Thus, a population inversion could be set up between the lowest state of the upper miniband 2 and the top state of the lower miniband 1. On the other hand, the minibands widths are designed to be smaller than LO phonon energy so that LO

phonon scattering is not directly involved and will not significantly degrade population inversion.

CSL design later gave way to the bound to continuum (BTC) design. Both structures rely on the scattering within the miniband to depopulate the lower lasing state. The difference is: in CSL, the upper lasing state is at the bottom of the upper miniband while in BTC, the upper lasing state is a defect state in the minigap. Radiative transition in BTC is more diagonal than in CSL, which results in a lower oscillator strength. But a diagonal design improves injection selectivity and upper state lifetime. So BTC showed improved temperature performance compared to CSL design.

The third major active region design is the resonant phonon (RP) design. In a RP design, collector and injector states are designed to be below the lower lasing state by ~E_{LO} to facilitate fast phonon depopulation, same as in mid-IR QCL. However, this scheme is the last one demonstrated among all three. Since the two lasing states are too close to each other, it is difficult to depopulate the lower lasing state without also depopulating the upper state. This problem was solved by designing the lower lasing state into a resonance with the excited state in the adjacent quantum wells, so that it has strong overlap with the extraction stage and is subject to sub-picosecond scattering. In the meantime, the upper lasing state, however, remains localized and has very little overlap with the extraction states, hence its picoseconds lifetime is preserved. RP design typically has a lower oscillator strength (0.5~1) than BTC (1.5~2). But on the other hand, it has the advantage of shorter length of one period, which results in a higher density of radiative transition.

Among these three types, RP design has the best temperature performance. BTC design can generate more gain under low temperature but degrades fast as temperature increases. So the current maximum output power devices are based on a BTC design

while the highest maximum operating temperature T_{max} is reported with devices based on a RP design.

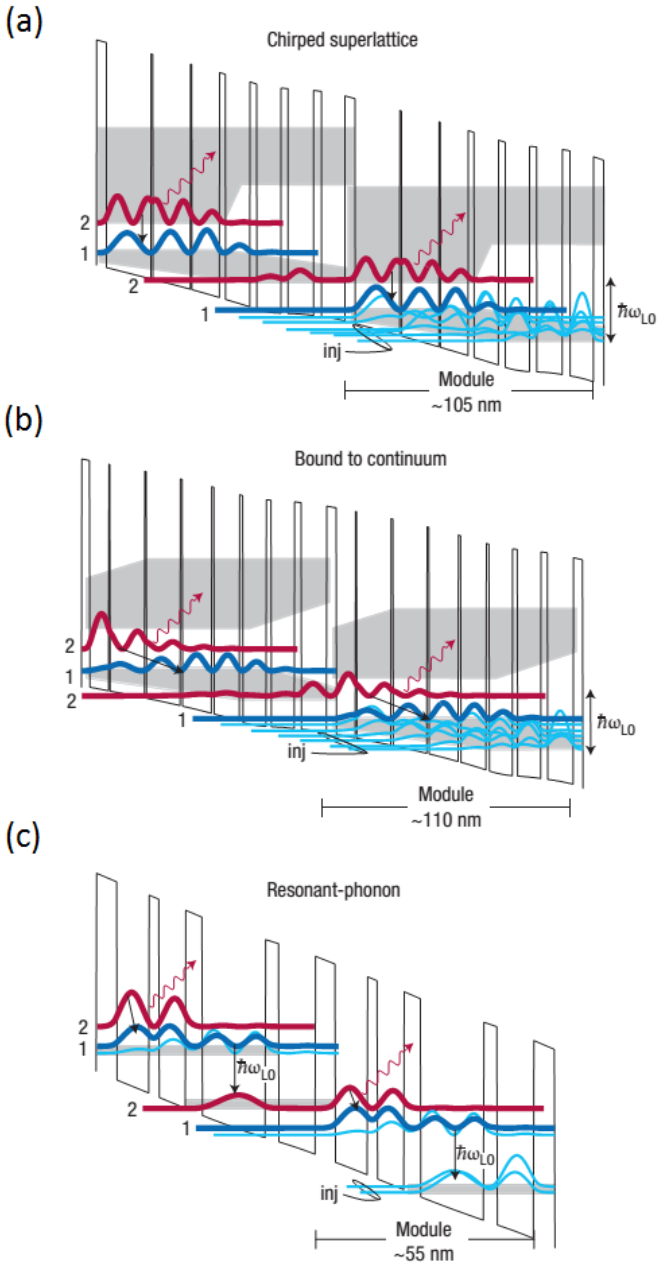

Figure 2.5, Conduction band diagram and electron wavefunction for three types of THz QCL designs: (a) chirped superlattice, (b) bound to continuum, (c) resonant phonon. Adapted from Ref. [33]

2.2.2 THz QCL Waveguide Design

Conventional dielectric waveguide cannot be applied to THz range due to the long wavelength nature of THz. New waveguide structure is required. There are two types of waveguides invented for THz QCL: the semi-insulating surface plasmon (SISP) waveguide and metal-metal (MM) waveguide (Fig. 2.6).

First THz QCL was demonstrated with SISP waveguide. SISP waveguide consists of a thin heavily doped plasma layer underneath the 10um thick active region, but on top of a semi-insulating GaAs substrate to eliminate substrate free carrier loss. Top of the ridge is covered with metal. The resulting mode is a compound mode bound to the top metal and the plasma layer as shown in Fig. 2.6. Confinement factor Γ for SISP waveguide is in the range of 0.1-0.5. For MM waveguide, 10um thick active region is immediately sandwiched between two metal layers. Such device structure is fabricated through wafer bonding. The mode in a MM waveguide is almost completely confined in the active region so the confinement factor Γ is almost 1. Free carrier loss is also minimized in MM waveguide.

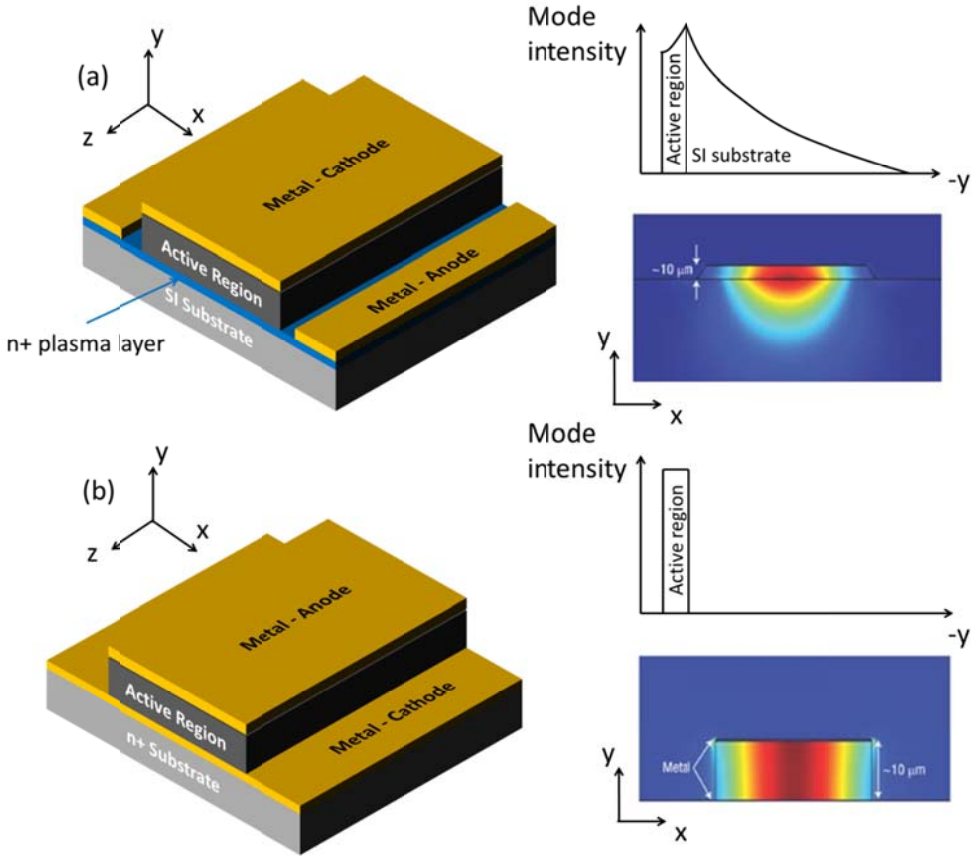

Figure 2.6, Schematic of device geometry (left), z direction 1D mode profile (right top) and xy plane cross section mode profile (right bottom) for (a) semi-insulating surface plasmon waveguide and (b) metal-metal waveguide. Adapted from Ref. [33]

MM waveguide minimize waveguide loss by increase Γ to almost unity. Moreover, due to impedance mismatch of subwavelength mode profile, MM waveguide facet reflectivity (0.5-0.9) is a lot higher than SISP waveguide (0.32), which reduces mirror loss. So the best T_{max} results are mostly MM waveguide devices. The drawback of MM waveguide is complicated fabrication process, poor slope efficiency and poor far field due to impedance mismatch. SISP waveguide is usually used in high power THz QCL. The advantage of SISP waveguide is its higher outcoupling efficiency, which is a

result of its lower facet reflectivity. Additionally, SISP waveguide produce a much better far field pattern compared with MM waveguide.

2.2.3 THz QCL High Temperature Operation

With active region and waveguide structure discussed above, THz lasing became possible, but only at low temperature. There are a number of factors degrading THz QCL performance as temperature rises and eventually cause it to cease lasing. For intersubband laser transitions from the upper laser state u to the lower laser state l, the peak gain g scales as $g \propto \Delta n_u f_{ul}/\Gamma$, where f_{ul} is the oscillator strength, Δn_{ul} is the population inversion and 2Γ is the full width at half maximum of the transition linewidth. The population inversion Δn_{ul} relies on having a relatively long upper level lifetime τ_u, selective electron injection, and fast extraction. The upper state lifetime τ_u is dominated by longitudinal optical (LO) phonon scattering of thermal electrons given by the expression $\tau_u^{-1} \propto \exp(-E_{LO}/kT_e)$, where E_{LO} is LO phonon energy, T_e is electron temperature which is usually 50-100K higher than lattice temperature. As temperature increases, activated phonon scattering will significantly degrade τ_u. Another degradation mechanism is thermal backfilling. It refers to the backfilling process of electrons from the injector state to the extractor state and lower lasing state, either by thermal excitation or by reabsorption of LO phonon. This is also a thermally activated process that increases with temperature. Moreover, at higher temperature, the transition linewidth broadens hence the injection/extraction selectivity degrades. These are main limiting factors for high temperature operation of THz QCLs. Record lasing temperature so far is 199.5K.

Fig. 2.7 is a summary of reported THz QCLs maximum lasing temperature versus their lasing frequency. Different symbol stands for different active region scheme and

solid symbols stand for CW operation while hollow symbols stand for pulsed operation. T_{max} is improved from 50K to current record of 199.5K. Improvement is achieved with innovations on both active region design and waveguide design. Resonant phonon design shows best temperature among all three types of design. CSL device never exceed liquid nitrogen temperature (77K) and BTC is limited below 120K. Because miniband in BTC and CSL is very narrow so that a few kT could seriously degrade the population inversion. Resonant phonon design is relatively insensitive due to a larger separation (~36meV). Implementation of Metal-Metal waveguide produced the most significant improvement on T_{max} by maximizing confinement factor and minimizing waveguide loss and mirror loss. Metal first used to sandwich active region was gold and later switched to copper which has higher conductivity to further reduce loss. Best T_{max} results so far exclusively use a combination of RP design and copper-copper waveguide.

Researchers are now trying to push this T_{max} towards temperatures accessible by thermoelectric coolers (~240K) and beyond. We have experimentally investigated two new active region designs to improve T_{max}.

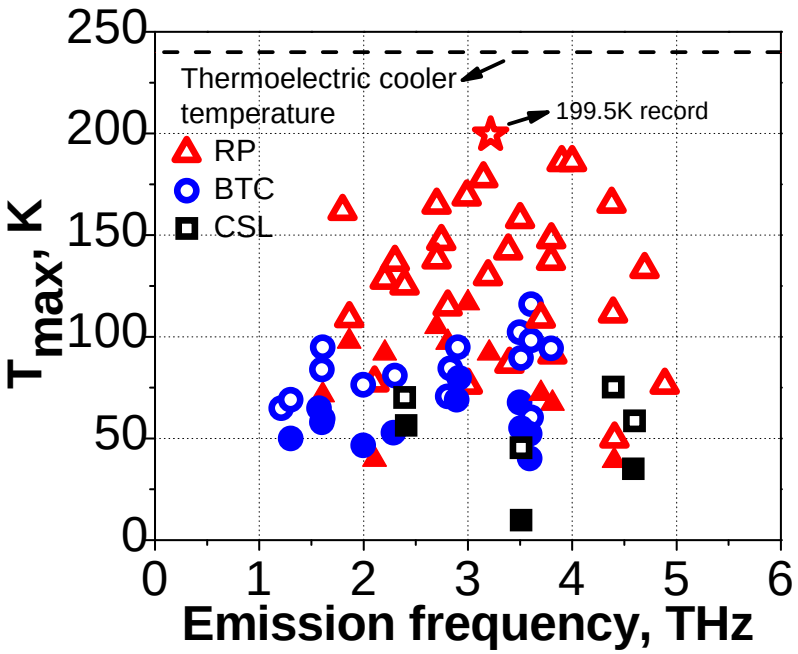

Figure 2.7, Summary of reported THz QCL maximum operation temperature versus lasing frequency. Different symbols represent different types of active region design

2.3 THz QCL with Variable Barrier Height

This section reviews our investigation of potential improvements in temperature performance achievable with THz QCLs with active region containing barriers of various heights.[34] Although the maximum operating temperature of experimentally-tested devices did not exceed the 199.5K record, our results demonstrate that terahertz quantum cascade laser designs with variable barrier heights provide a viable alternative to the traditional active region designs with fixed barrier composition.

2.3.1 Variable Barrier Height

Three-well RP QCL designs based on the GaAs/AlGaAs material system, using 15% aluminum content in the barriers have shown so far best T_{max} results[19, 35, 36]. Fig. 2.8 shows the conduction band diagram of an optimized three-well RP design. Latest improvement of RP design T_{max} relies on optimization of the "diagonality".

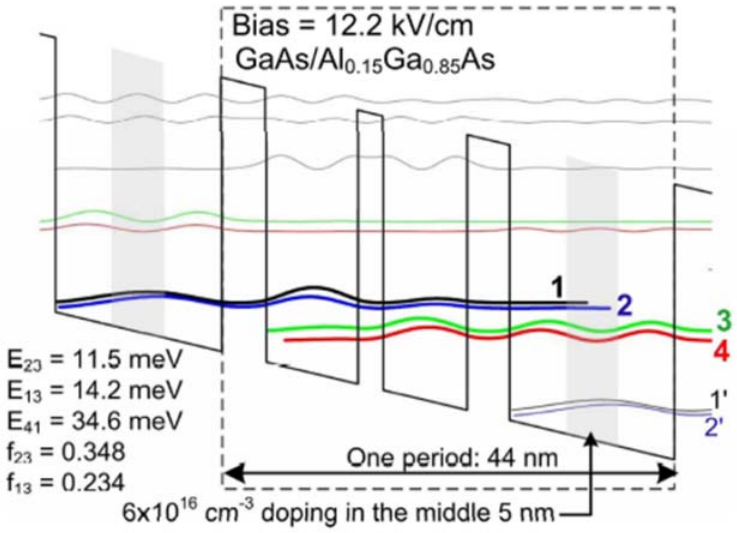

Figure 2.8, Conduction band diagram, calculated electron energy levels and wave functions for the T_{max}=199.5K THz QCL based on three-well resonant phonon design. Adapted from Ref. [19]

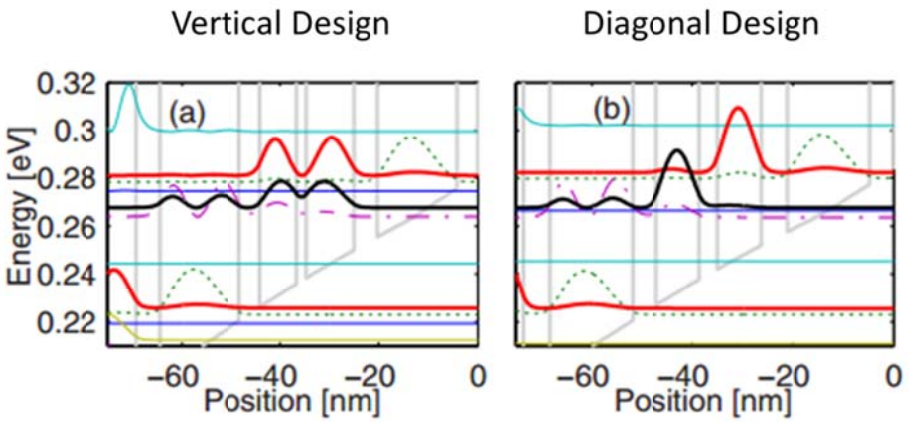

Figure 2.9, Conduction band diagram, calculated electron energy levels and wave functions for (a) vertical THz QCL RP design and (b) diagonal THz QCL RP design. Adapted from Ref. [37]

Diagonality refers to the degree of overlap between the two lasing states. Fig. 2.9 (a) and (b) show a vertical design with strong overlap and a diagonal design with reduced overlap. There are tradeoffs between vertical and diagonal designs in terms of oscillator strength and injection/extraction selectivity. Small spatial overlap in a diagonal design is expected to improve the electron injection efficiency into the upper laser state and suppress electron leakage from the upper laser state to the downstream injector, which helps to increase population inversion. However, the oscillator strength of a diagonal design is reduced compared with a vertical design. As a result, a vertical design is expected to provide higher gain at lower operating temperatures, when the LO phonon scattering is suppressed and the electron injection is not degraded by broadening. However, diagonal transitions may have advantages at higher operating temperatures since it has better performance of preserving population inversion as temperature increases. Simulations have shown that for designs emitting above 3.5 THz, diagonal structures offer advantages at operating temperatures below 200 K. These results provided a basis of optimization of THz QCL T_{max} from ~160K to ~200K.

The optimization of f_{ul} and diagonality, as well as electron injection and extraction efficiency is principally performed by adjusting well and barrier thicknesses. The design in [19] marks the state of the art of such optimization, however, the room for further improvement by changing layer thicknesses is limited. We proposed that varying the barrier heights in the QCL structure may introduce new degree of freedom in a THz QCL design and may help to boost the maximum operating temperature. Since the AlGaAs barriers are lattice matched to the GaAs substrate for effectively any aluminum fraction, AlGaAs/GaAs THz QCLs with variable barrier heights can be easily produced experimentally.

2.3.2 Simulation Results

We started with the 199.5K structure[19] as a reference and developed two new designs with variable barrier heights. The new designs were optimized based on semiclassical ensemble Monte-Carlo simulations (EMC) in collaboration with Prof. Christian Jirauschek group in the Technical University of Munich[37, 38]. An attempt was made to introduce only limited structure modifications to be able to make a comparison of performance to the reference structure.

The layer sequences of one period of the active regions in Angstrom are (subscripts indicate Al contents in AlGaAs barriers) $43_{.15}/160_0/41_{.15}/72_0/46_{.075}/82_0$ and $43_{.15}/142_0/54_{.05}/18_{.15}/81_0/20_{.15}/91_0$, for design 1 and 2 respectively. The simulated conduction band diagrams of two consecutive stages of the structures under applied operating bias voltage are shown in Fig. 2.10. In the optimization process, the structures have been biased approximately at these voltages and the layers have been changed in order to control the lasing frequency, injection anticrossing and oscillator strength. Table

1 is a summary for band diagram information of all three designs at 200K. Table 2 is a summary for transport properties of all three designs at 200K under the condition of maximum current density.

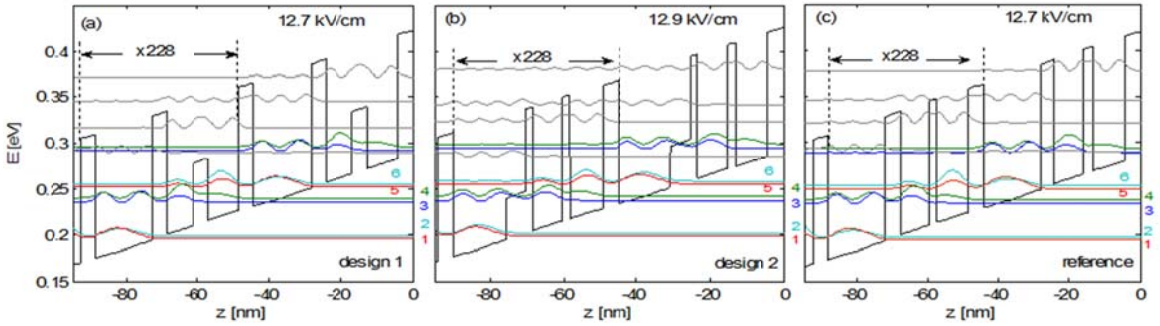

Figure 2.10, Conduction band diagram and relevant energy state wavefunctions of the two laser designs, design 1 (a) and design 2 (b) and the reference structure (c).

For design 1 (Fig. 2.10(a)), the width of the middle barrier in the lasing double well is increased while the height is reduced. The injection well, barrier and extraction barrier are kept the same as the reference. The varying barrier is a unique property of design 1, which allows for the diagonal transitions to be kept while the oscillator strength is increased. EMC simulations show an increased oscillator strength ($f_{54,design1} \approx 0.378$) and injection efficiency ($\eta_{5,design1} \approx 50.9$ %. Definitions for η_j can be found in Ref. [39]) as compared to the Ref. [19] ($f_{54,reference} \approx 0.293$ and $\eta_{5,reference} \approx 45.6$ %). Furthermore, the lowered barrier height in the active region has also the role to reduce interface roughness scattering.[38]

For design 2 the extraction barrier is replaced by a step barrier. Good internal quantum efficiency was reported for the step barrier design in Ref. [40]. We implement the step barrier in our design 2 and adjust it to increase the extraction coupling and decrease the lifetime τ_4 of the lower laser state. The EMC results show an increase of the oscillator strength and injection efficiency to $f_{54,design2} \approx 0.601$ and $\eta_{5,design2} \approx 54.2$ %. Step

barrier designs can reduce parasitic current before threshold by localizing the states at low bias, however, for design 2 the thin extraction barrier introduces other parasitic channels that cancel this effect. The lifetime τ_4 for design 2 has the smallest value among all three designs, showing possible advantage in lower laser state depopulation. However, the introduced parasitic channels lower the relative depopulation rate r_4/r_0, where $r_0=J/(e_0 n_{2D})$ is a measure for the overall scattering strength in the structure.

	f_{osc}	f_{osc}^{54}	e_{34}[meV]	e_{35}[meV]	e_{36}[meV]	e_{46}[meV]	e_{56}[meV]
Design 1	0.744	0.378	4.8	4.5	1	1.28	2.8
Design 2	0.959	0.601	5.6	5.5	1.1	1.35	2.8
Ref.	0.617	0.293	5	4.3	1	1.24	2.8

Table 2.1 Overview of oscillator strengths and anticrossings for the three designs at 200K. $f_{osc}= f_{osc}^{54}+ f_{osc}^{64}$ is the total oscillator strength,, and f_{osc}^{54} is the main lasing transition oscillator strength. e_{34},e_{35}, e_{36},e_{46} and e_{56} are full state alignment anticrossings between the level 3,4,5 and 6.

	p_6[%]	p_5[%]	p_4[%]	η_5[%]	η_4[%]	J[kA/cm^2]	r_4/r_0	τ_4[ps]
Design 1	32.3	39.1	15.9	50.9	32.1	1.764	3.87	0.703
Design 2	32.4	36.4	15.5	54.2	27.2	2.099	3.33	0.688
Ref.	32.0	40.1	14.5	45.6	30.9	1.674	4.08	0.703

Table 2.2 Comparison of carrier transport parameters for the three designs at 200K, extracted from EMC simulations at maximum current density. p_4, p_5, and p_6 are the populations for the different levels. η_5 and η_4 are the injection efficiencies into the upper and lower laser level. J is the maximum current density. r_4/r_0 is the normalized total outscattering rate from level 4 to lower-lying levels, with $r_0^{-1} = e_0 n_{2D}/J$, being the average dwell time of an electron in a period. τ_4 is the lifetime of level 4.

Fig. 2.11 plots the simulated I-V characteristics for all three designs at a lattice temperature of 200K. For both design 1 and design 2, higher simulated current results from an increase of the oscillator strength (Table 2.1) and parasitic channels (Table 2.2). Furthermore, higher simulated gain for designs 1 and 2 also shows that the parasitic channels could be overcome by the increased oscillator strength which is directly proportional to gain. Design 1 has higher current as a result of reduction of the barrier height in the lasing double well, and the increase of oscillator strength provides a stronger coupling of the lasing states which increases the current. We can also observe how similar the shapes of the current-voltage curves are, since the modifications were minimal and therefore the physics of design 1 has only slightly been adjusted. The current for design 2 is strongly increased due to the strong coupling of the lower laser level with the extraction level and the increased oscillator strength.

By varying the barriers, the coupling of continuum states from the higher minibands to the lasing states of the adjacent period can have an influence on lasing.[41] In the design process a special care has been taken to keep the higher minibands similar to that of the reference structure. Additionally, the energetic distance of the lasing states from high miniband states are not changing significantly for the different designs, therefore in the EMC simulations the latter have been neglected.

Fig. 2.12(a) plots the simulated gain spectra at a lattice temperature of 200K for all three designs. Both new designs are predicted to have higher peak gain than the reference structure at 200K. We see a strong improvement of the gain for design 2 and a moderate improvement for design 1. All these improvements come from the increased oscillator strengths, while the occupations are not changed significantly. For design 1, the improved injection and slightly increased current has helped to preserve almost the same inversion (lowered only by ~ 6% as compared to the inversion in the reference). Design

2 also roughly preserves its inversion (lowered by ~ 15 % as compared to the inversion in the reference) due to a reduced lifetime of the lower laser state. The increase of the oscillator strengths is larger than the decrease of the inversion thus we get improvements for the gain. Fig. 2.12(b) shows the calculated maximum peak gain versus temperature for the two new designs. If we assume a virtual loss of 40 cm-1 as in Ref. [38], the expected T_{max} are expected to be improved by ~15K and ~40K for design 1 and design 2, respectively.

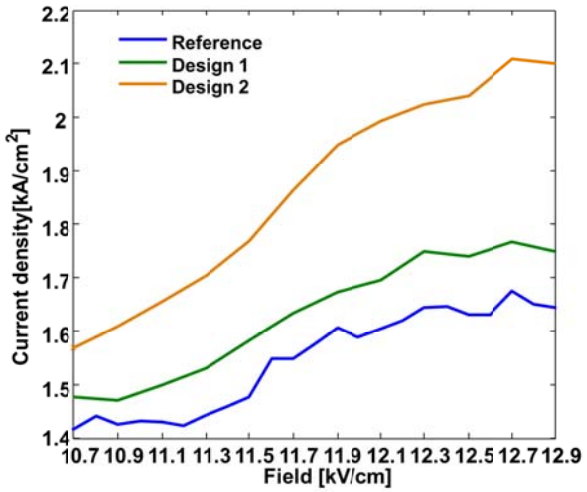

Figure 2.11, Simulated current-voltage characteristics of new designs and the reference at 200K

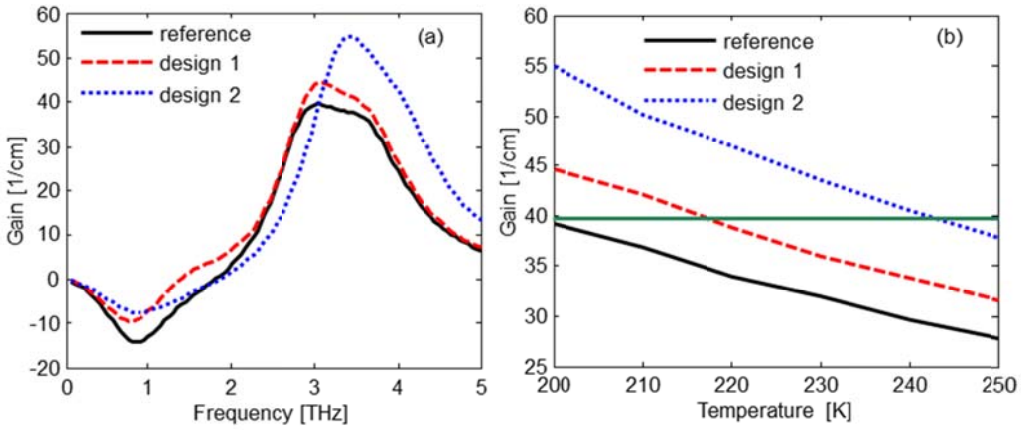

Figure 2.12, (a) Simulated gain spectra at a lattice temperature of 200K calculated using EMC simulations for the reference structure and its two modifications. (b) Peak gain versus temperature calculated for the three structures in (a) using EMC simulations.

Overall, EMC simulations indicate that both designs 1 and 2 produce more gain compared to the reference structure at high temperatures. The expected T_{max} are approximately 215K and 240K for design 1 and design 2, respectively.

2.3.3 Wafer Growth and Device Processing

Both design 1 and design 2, together with the 199.5 K reference structure,[19] were grown at the National Research Council of Canada in the V90 VG Semicon Molecular Beam Epitaxy (MBE) system on semi-insulating (001)-oriented GaAs substrates. Arsenic dimers were generated using Veeco Mark V valved cracker source, while two Veeco SUMO cells were used to supply gallium and a dual-filament cell with 40cc conical crucible was used for aluminum. Both Ga sources were used to grow GaAs at 0.25 nm/s, as well as for the 7.5% or 5% AlGaAs barriers, while only one Ga source was used for the growth of the 15% AlGaAs barriers. To facilitate direct comparison the same approach was used for the growth of the reference structure. Thus the growth conditions

for the latter were not identical to the original structure which demonstrated T_{max} of 199.5 K, for which only one Ga cell and one Al cell was used for the growth of GaAs at 0.23 nm/s and growth of 15% AlGaAs. Flux drift compensation was employed during the growth.[42] High Resolution X-ray Diffraction measurements revealed that layer thicknesses for all three structures were within 0.5% of the target parameters. The active region thickness was kept at 10 μm. Contact layers structure and QCL active region doping were kept in the same manner as in the 199.5K reference[2] to ensure the same loss for all structures. More specifically, for all our structures, the injector well is doped to 6×10^{16} cm^{-3} in the middle 50 Å section and the active region is sandwiched between 100 nm of 5×10^{18} cm^{-3} bottom n+ GaAs layer and the top stack of 50 nm of 5×10^{18} cm^{-3} and 10 nm of 4×10^{19} cm^{-3} n+ GaAs layers capped with 3.5 nm LT-GaAs passivation layer.[18]

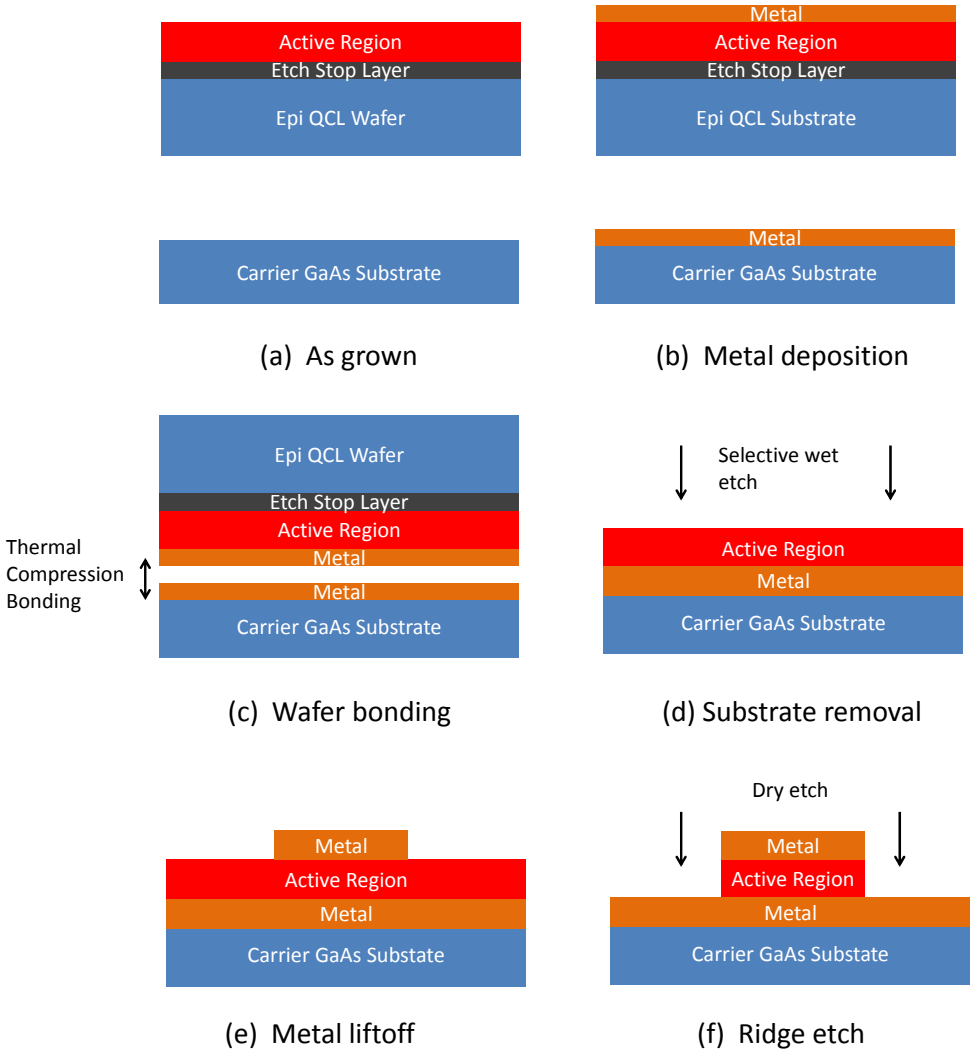

Figure 2.13, Fabrication process for Metal-Metal waveguide THz QCL using wafer bonding

All three wafers were processed into copper-copper double metal waveguide devices under the same conditions. The fabrication process flow is shown in Fig. 2.13. Another GaAs wafer is needed as a carrier or receptor. A metal layer sequence Ta/Cu/Ti/Au (10nm/350nm/10nm/400nm) was deposited on top of both the MBE-grown QCL wafer and the carrier wafer. Copper is used to form metal-metal waveguide. The

gold layer is used to facilitate Au-Au bonding which has low bonding temperature than Cu-Cu bonding. The epi chips were flipped and bonded to carriers using Au-Au thermo-compression bonding. Bonding temperature is kept low at 325C to minimize copper diffusion into the active region. After bonding, the sample substrate was selectively removed using $NH_4OH:H_2O_2$ solution. An $Al_{0.55}Ga_{0.45}As$ layer in between the active region and the substrate serves as an etch stop layer and was removed after substrate removal using hydrofluoric acid. The top n+ contact layer was removed to further reduce the waveguide loss. A metal stack Ta/Cu/Ti/Ni (10nm/300nm/10nm/100nm) was deposited and patterned through a lift-off process to form 120-μm-wide contacts for the future laser ridges. Copper metal is for the waveguide confinement while nickel layer is used as a self-align dry etch mask for subsequent ridge etch. Cl_2/BCl_3 plasma dry etch was then employed to etch the laser ridges. Fig. 2.14 shows an SEM picture of processed metal-metal waveguide THz QCLs. The device substrates were then thinned down to ~200μm, backside metal contact (Ti 10nm / Au 50nm) was deposited, and the wafers were cleaved into ~1.5 mm long laser bars, indium soldered on copper heat sinks, and mounted in a cryostat for measurements.

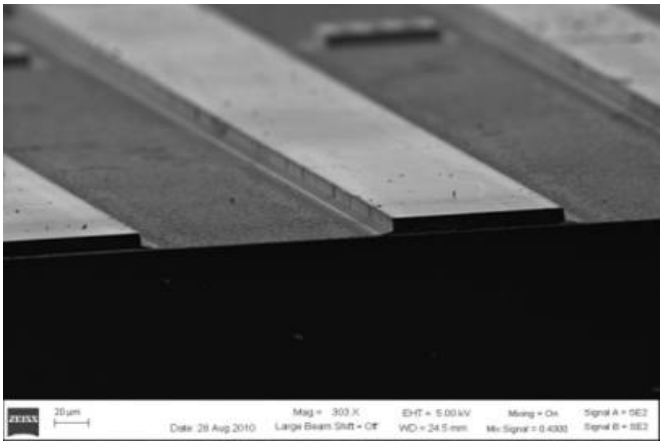

Figure 2.14, SEM image of metal-metal waveguide devices

2.3.3 Experimental Results

Testing was carried out in pulsed mode with 100 ns pulses at a 5 kHz repetition rate. The power was measured with a calibrated helium-cooled Si bolometer using an optical setup with two 2-inch-diameter off-axis parabolic-mirrors: one with focal length of 50 mm to collimate the light from the device and the second one with 100 mm focal length to refocus the light onto the detector. Spectra were measured using a Fourier-transform infrared spectrometer (FTIR). Output power-current (L-I) characteristics of the devices are presented in Fig. 2.15. Lasing spectra at 78K is shown in Fig. 2.16. The maximum operating temperatures were measured to be 191 K, 188 K, and 176 K for the reference, design 1, and design 2 devices, respectively. Design 1 has a T_{max} very close to that of the reference structure, while T_{max} of design 2 degrades considerably, in contrast with EMC predictions

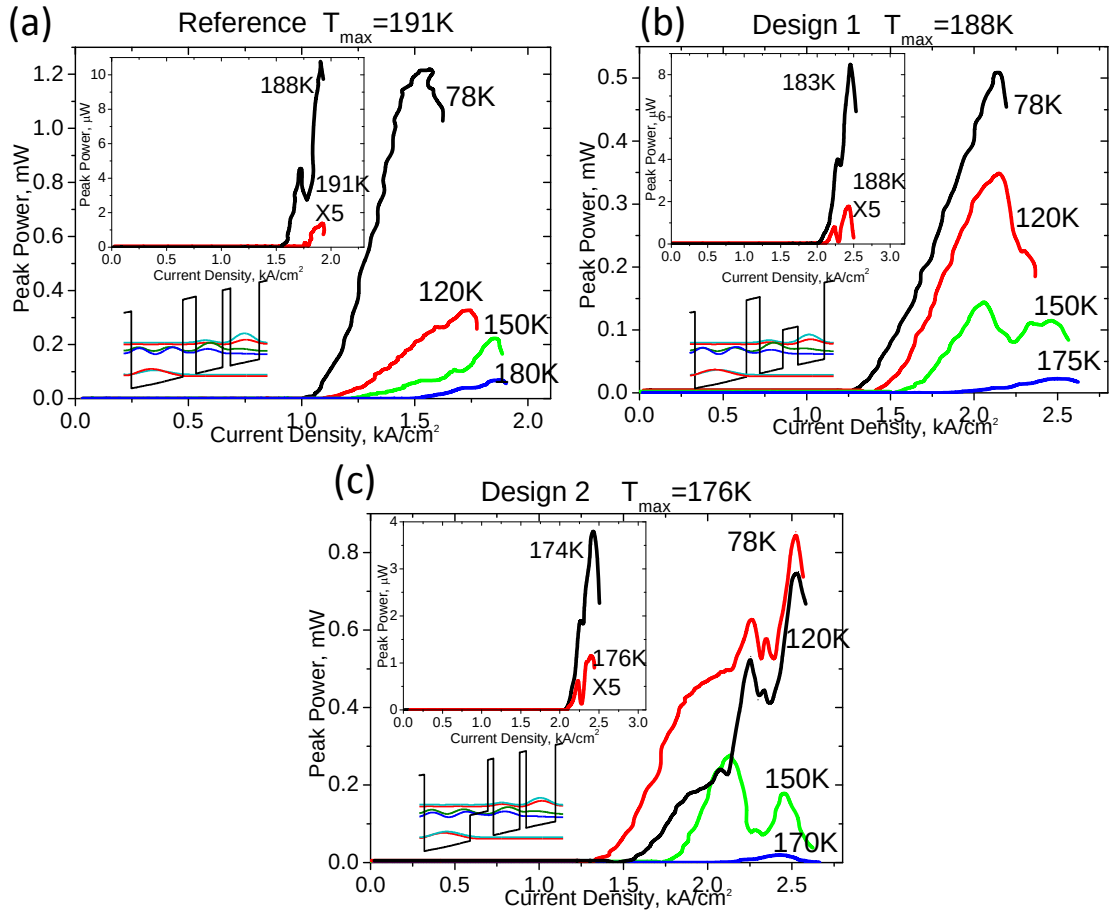

Figure 2.15, THz output power vs. current density (L-I) at different heat sink temperatures. THz power data was not corrected for collection efficiency. Insets: L-I characteristics close to T_{max}. Panels (a), (b) and (c) represent results of the reference structure, design 1, and design 2, respectively.

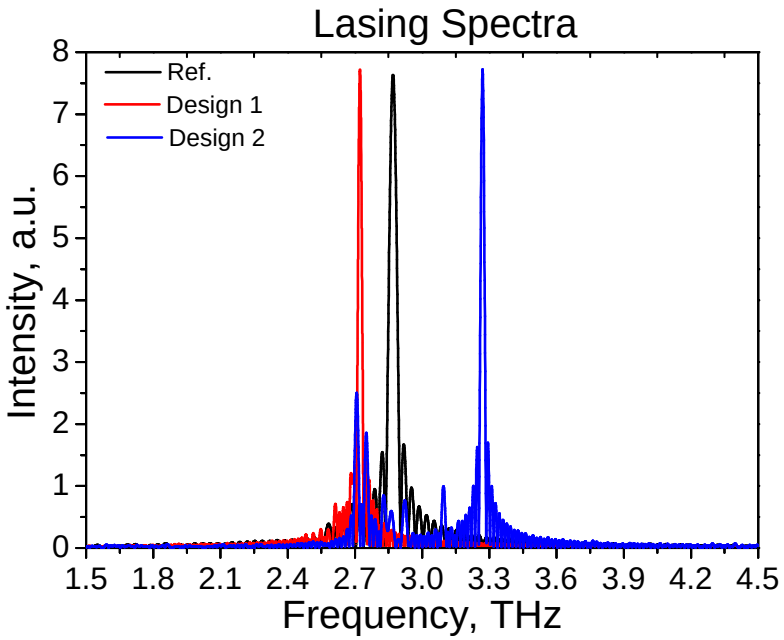

Figure 2.16, Lasing spectra for all 3 designs at heatsink temperature of 78K near the maximum power output.

Fig. 2.17 plots the threshold current density versus temperature. The threshold current density of design 1 is almost constantly 25% higher than that of the reference. Since the sheet doping density per QCL period in all structures was the same and the injection/extraction barrier thickness and composition is identical for design 1 and the reference structure, the higher current density may be attributed to parasitic channels due to the reduced barrier height in the active region resulting in an increased coupling of the states.

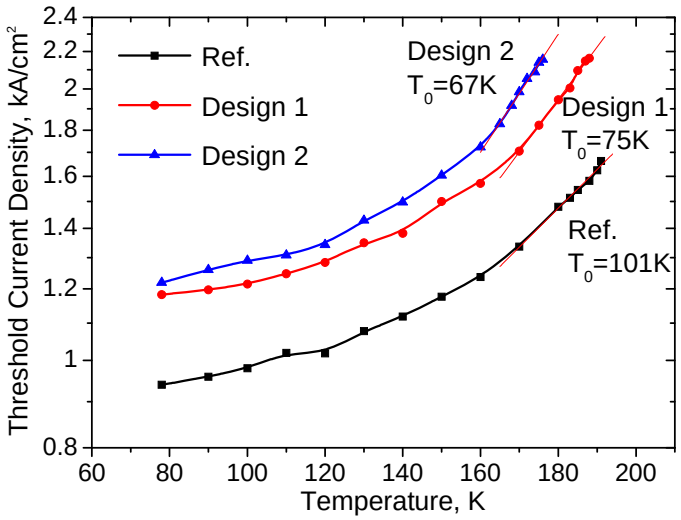

Figure 2.17, Threshold current density vs. temperature for the three designs tested.

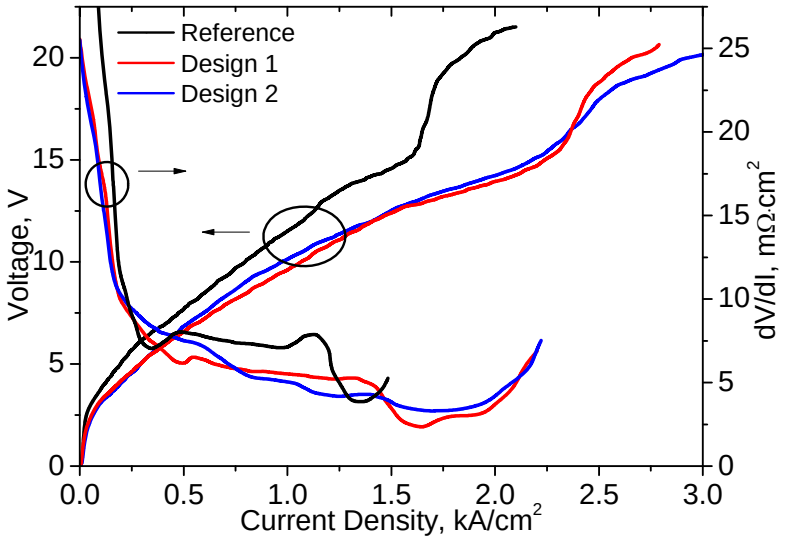

Figure 2.18, Current density-voltage (I-V) characteristics and differential resistance versus current density (dV/dI-I) data for the three designs tested at 150K.

Fig. 2.18 shows the current-voltage (I-V) characteristics and dV/dI-I characteristics for all structures at 150K. The dV/dI-I characteristics for the design 1 as well as for the reference structure show a clear differential resistance drop at the beginning of lasing. The relative size of this drop is a measure of the difference of upper

and lower radiative state lifetime and also a measure of injection efficiency.[20, 43] The small differential resistance drop in design 2 is an indication of poorer injection efficiency, compared to the first two designs. At the end of the tunneling resonance, onset of high differential resistance is more gradual in design 2. The high differential resistance region is also narrower and the differential resistance is relatively low. These are all indications of degraded selectivity of injection and extraction. EMC simulations show that the oscillator strength of design 2 increases a lot, compared to the reference structure that leads to superior performance at higher temperatures. However, these results could be inaccurate due to the limitations of our design approach.

The discrepancies between theory and experiment from the theoretical side can be due to the number of energetic states or due to the imprecise material parameters considered. The EMC simulations here have used 4 energetic states, which give a simplified model for the designs. Moreover, our simulation does not consider leakage to continuum, aperiodicity of the biased QCL stages (i.e. domain formation) as well as parameter uncertainties (percentage of donors that are ionized, interface roughness parameters) and lack of effects like higher-order scattering events and tunneling. Further refinement of EMC simulation parameters is needed to improve its predictive power for the step barrier design.

2.3.3 Summary and future work

To summarize, the new designs with variable barrier height did not achieve maximum operating temperatures superior to that of the reference record structure, however, the maximum operating temperature of design 1 was very similar to that of the reference laser. The results indicate that variation of aluminum fraction in barriers during

device growth does not result in significant laser performance deterioration and using barriers with variable aluminum fractions in the THz QCL active region is a viable approach to enhance the design space for THz QCLs. Experimental data is expected to help improving simulation accuracy.

2.4 Optical Tuning of THz QCL

In the field of THz spectroscopy, there are cases requiring high peak power or average power of THz output. For example, tip enhanced spectroscopy demonstrated in [44] is readily applied to THz range. In this case, over 500 mW of peak power is required. For room-temperature THz DFG-QCL sources (see Chapter 3), broad tenability has been demonstrated with an external cavity setup. However, due to the nonlinear process efficiency, the output power is limited to milliwatts level. Even with the potential for further improvements, this technology is unlikely to meet the need of 500 mW THz peak power output. In such cases, cryocooled THz QCLs with record peak power of over 1W becomes the only available option. So far, tuning range of THz QCL is still limited under 500 GHz. This section describes an external optical tuning method we proposed to tune THz QCL which potentially has no limit on tuning range. Preliminary experimental results will be presented. Although tuning has not been achieved yet, current results support the feasibility of this method. Further improvement and optimization is required for this idea to work.

2.4.1 Lasing Wavelength Control

In semiconductor lasers, lasing wavelength is usually controlled by building a grating section (periodically corrugated waveguide structure) into the laser. As shown in

Fig. 2.19., there are two types of gratings: distributed feedback (DFB) grating and Distributed Bragg Reflection (DBR) grating. These periodic structures are able to provide wavelength dependent feedback and achieve single wave lasing. The effectiveness of DFB/DBR grating is characterized by "coupling strength". The coupling strength need to be higher than a certain value to achieve single wavelength lasing. Details of DFB grating will be readdressed in Chap. 4. Spectral tuning of DFB or DBR laser is usually done by thermally induced or carrier induced refractive index change. Another way of tuning is based on an external grating configuration. (Fig. 2.19) Selective feedback is determined by grating pitch and relative angle to laser. Tuning of lasing wavelength is achieved by changing the relative angle of grating to laser cavity. Compared to temperature tuning which can be done compactly with current injection, external grating tuning is bulky and requires precise alignment.

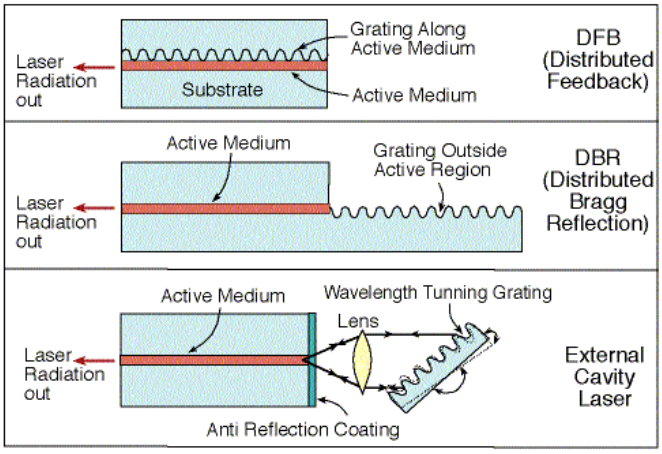

Figure 2.19, Schematic of DFB, DBR and external grating setup for laser wavelength selection.

2.4.2 Optically induced refractive index shift

Conventional tuning methods like temperature tuning and external cavity tuning find difficulty to be applied to THz QCL. For the temperature tuning, the tuning range scales with lasing frequency because it is based on pure thermally induced index shift. For III-V semiconductor, index temperature coefficient at THz frequency is on the order of 1×10^{-4} per Kelvin. Therefore, tuning range is limited to a small portion (1~2%) of lasing frequency, and best result is 30Ghz[45]. For the external cavity setup, it is difficult to focus a large fraction of the beam diffract from external grating back to the laser cavity due to the subwavelength cross section of a THz QCL device. Only coarse tuning is reported using this method[46]. Another result of 330 Ghz tuning is demonstrated by a novel method of tuning transverse modal wavevector[47], based on a sophisticated MEMS system. None of these results achieve tuning over 400 Ghz. We need to explore new way for the tuning task.

This idea originates from the results of optically tuned mid-IR QCL[48], which reported tuning the mid-IR QCL wavelength by shining near-IR light onto the active region. The incoming near-IR photon energy is set higher than the active region material bandgap in order to generate electron-hole pairs. Generated excessive electrons increase the free carrier absorption loss. Then the real part of refractive index will change according to the Kramers Kronig relationship. (For free carrier absorption and refractive index calculation, only electrons are considered because holes have higher effective mass and lower response to electromagnetic field.) In Ref. [48], index shift of 6.5×10^{-4} was obtained by 5×10^{15} cm^{-3} excessive electron concentration, at wavelength around 9.2um. In the THz region, since free carrier absorption scales quadratically with wavelength, refractive index changes more rapidly with electron concentration. Index of GaAs at THz frequency is given by Drude model:

$$\epsilon(\omega) = \epsilon_{GaAs} + i\frac{n_{carrier}e^2\tau}{\omega m^*(1 - i\omega\tau)} \tag{2.1}$$

$$\mathrm{n} = \mathrm{Re}\left(\sqrt{\epsilon}\right) \tag{2.2}$$

where ϵ_{GaAs} is 12.96, τ is relaxation time which is 0.1ps for highly doped GaAs and 0.5ps for lightly dope GaAs, m^* is effective mass $0.067m_0$ ω is the EM wave frequency and $n_{carrier}$ is the free carrier density, n is the real part of refractive index. With small carrier density change, index change is approximately proportional to carrier density change:

$$\Delta\mathrm{n} \propto \Delta n_{carrier} \tag{2.3}$$

where n is refractive index and $n_{carrier}$ is carrier density. Calculation shows 2.5×10^{15} cm^{-3} of excessive electrons will induce a real index change of about 0.05. We propose to spatially modulate the pumping light incident on the laser to generate a periodic modulation of refractive index inside the laser cavity, as shown in Fig. 2.20. This modulation can be done by projecting a grating image on the laser cavity (Fig. 2.21). Fig. 2.22 is an image taken by CCD camera showing a clear projected grating pattern on laser ridge. This pattern is projected by an objective lens and a photomask with grating patterns. If the grating is strong enough to achieve single mode lasing, lasing wavelength can then be tuned by varying the grating projection parameters. This optically generated grating is only possible in THz QCL as a benefit of its long wavelength.

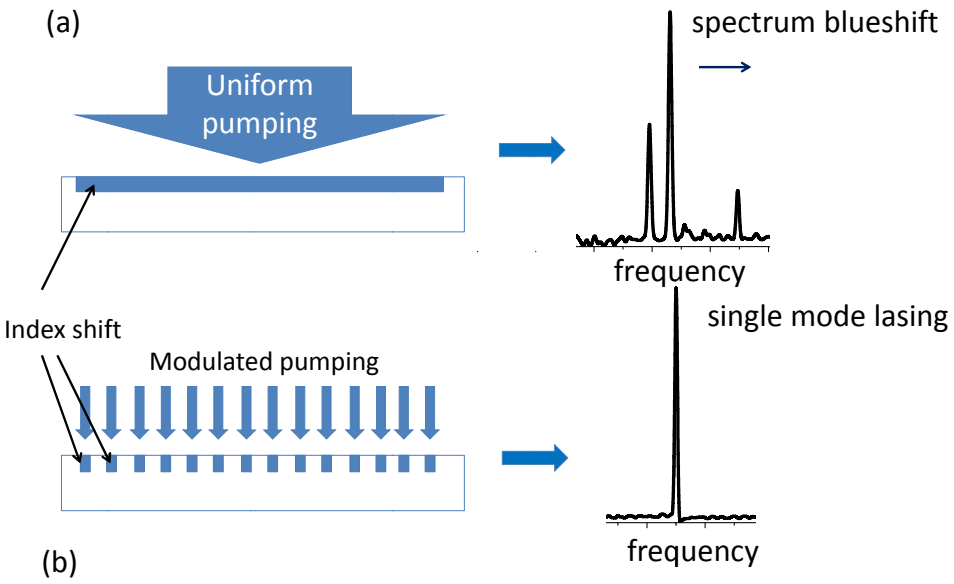

Figure 2.20, Illustration of (a) uniform pumping and spectrum blueshift induced by uniform pumping (b) periodically modulated pumping and possible single mode lasing if grating is strong enough

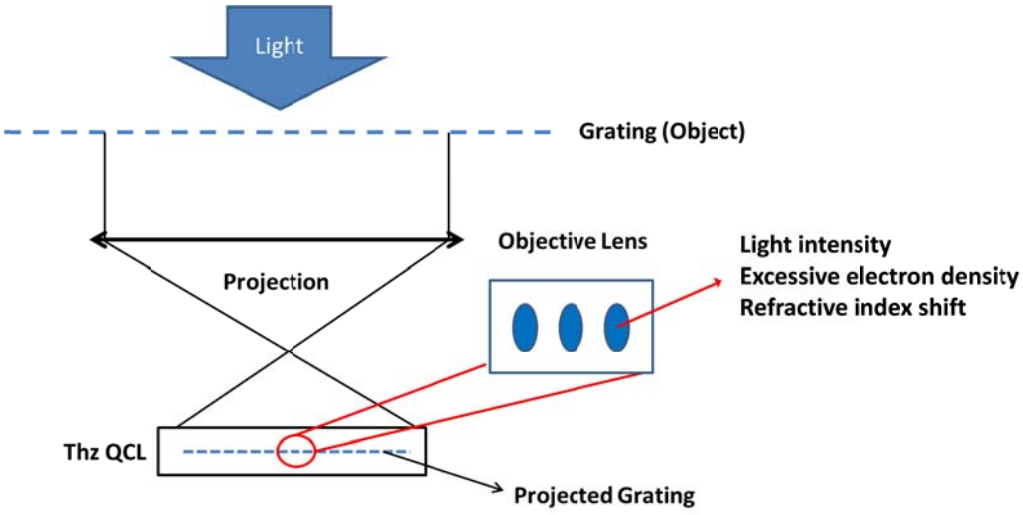

Figure 2.21, Schematic showing grating projection onto a THz QCL using an objective lens and a grating object.

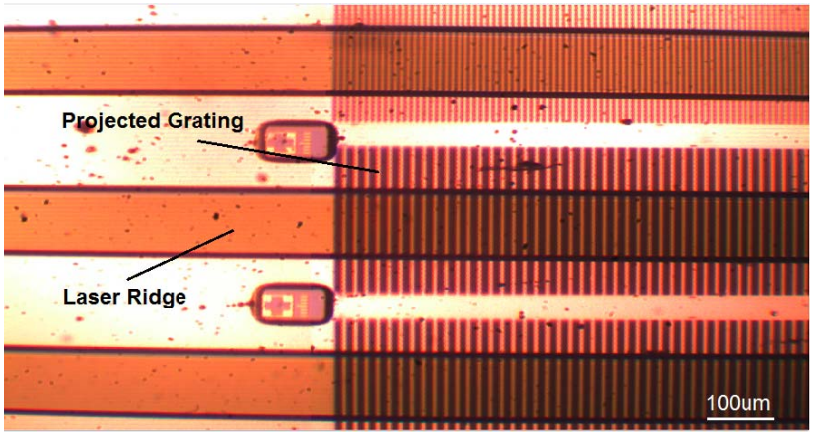

Figure 2.22, Top view image of laser ridges and projected grating patterns taken by a CCD camera. Laser ridge and grating patterns are indicated.

2.4.3 Metal-stripes waveguide

For a THz QCL, either with SISP waveguide or MM waveguide, there is a metal layer covering the top of the ridge. Metal is not only electrical contact but also a waveguide component. However, metal is not transparent to light. We need to open windows for pumping light to enter the active region. We proposed to use metal stripes shown in Fig. 2.23 to replace the top continuous metal layer.

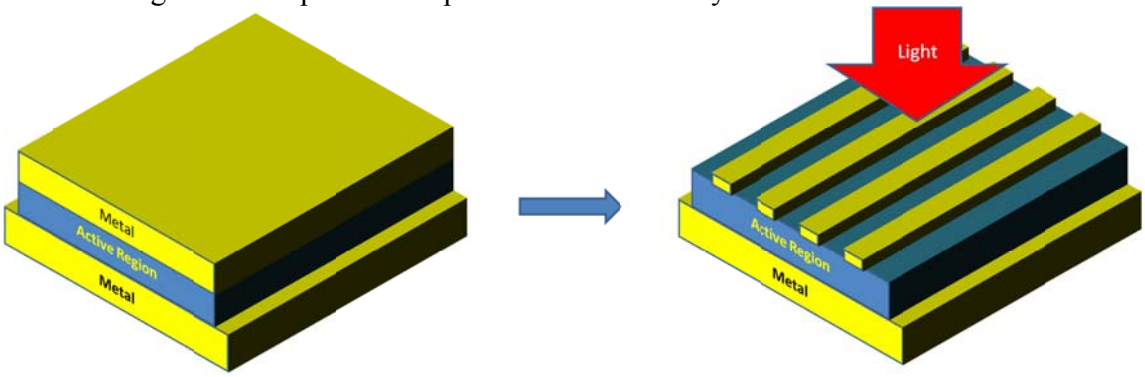

Figure 2.23, Schematic of metal-metal waveguide with continuous metal (left) and metal stripe (right) on top. Metal stripes allow transmission of light incident from top

We simulated the modal loss and mode profile for this metal stripes structure. For 1um wide 300nm thick gold stripes with 1um spacing on top, THz mode is still confined in the active region and the modal loss increases by less than 10% (from ~31cm^{-1} to ~34cm^{-1} for a typical device described in section 2.3.3). Simulated mode profiles are shown in Fig. 2.24. The transmittance of near-IR light (800nm) into active region is calculated to be ~60% if incident light is polarized perpendicular to the stripes. Subwavelength metal stripes are expected to allow higher transmission. However, it is not adopted due to fabrication difficulty. This metal stripes structure is also applicable to SISP waveguide.

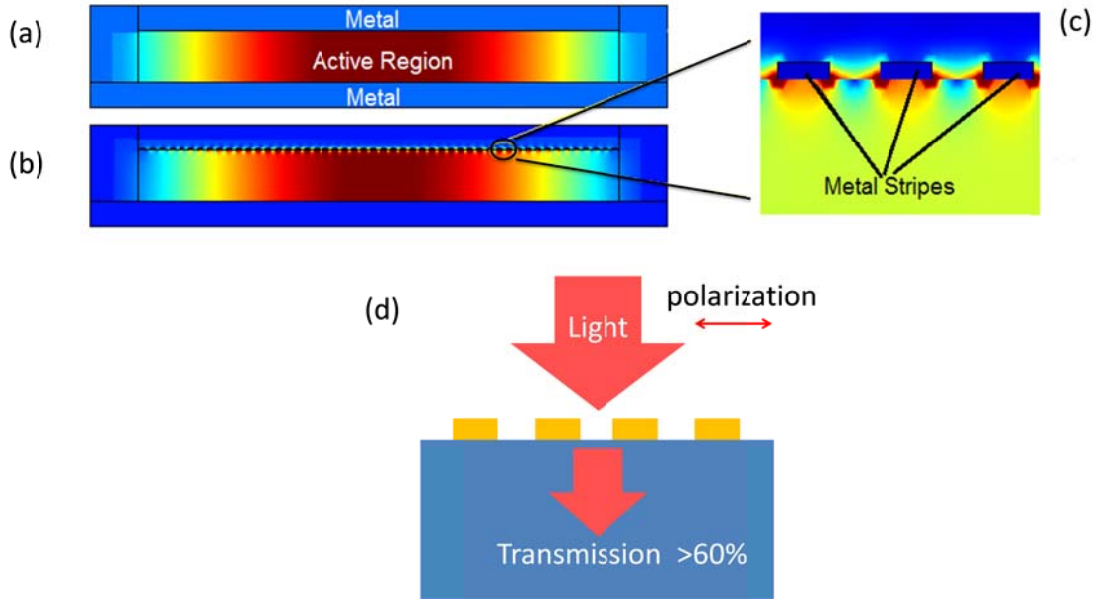

Figure 2.24, Simulated mode profile for (a) continuous metal–metal waveguide and (b) metal stripes waveguide. Panel (c) is detail mode profile near the surface metal stripes. Panel (d) illustrates transmission of pumping light through the metal stripes structure.

2.4.4 Modulation transfer: diffraction limit and carrier diffusion

Spatial modulation of illumination involves a projection process of a grating. During the process of converting the object grating to a periodic distribution of electrons/refractive index shift in a THz QCL active region, a number of mechanisms will degrade the final effective modulation of electron concentration. This is similar to the concept of modulation transfer function in photolithography. If this feature broadening is wider than a quarter of a grating period (Fig. 2.25), the effective modulation will be significant degraded. At least two mechanisms will contribute to the degradation: diffraction and carrier diffusion.

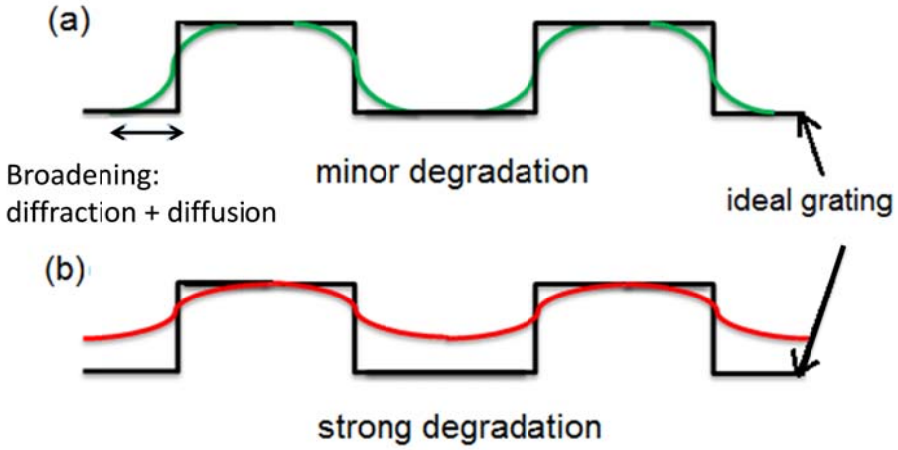

Figure 2.25, Schematic illustrating (a) a minor degradation of modulation, (b) a strong degradation caused by broadening wider than a quarter grating period

First mechanism is the diffraction limited image resolution. A simplest projection system is a microscope objective. An objective is usually characterized by magnification factor and Numerical Aperture (NA). In this case, the objective is used in the reversed way as compared to in a microscope, i.e. to minify an object, which is similar to projection photolithography. The grating image resolution limit is given by:

$$\mathrm{r} = \frac{0.61\lambda_0}{NA} \tag{2.4}$$

where λ_0 is free space wavelength (of illumination light). Better image resolution could be achieved by high NA objective. However, NA is limited by depth of focus (DOF), which measures the tolerance of placement of the image plane:

$$\mathrm{DOF} = \frac{\lambda_0}{NA^2} \tag{2.5}$$

Too high NA will pose difficulty on alignment. We choose a 10X objective with 0.22 NA. Then diffraction related degradation is r≈2.7λ_0

Second mechanism is carrier diffusion. Diffusion is an intrinsic property of semiconductor and cannot be easily engineered. Diffusion length is given by:

$$\mathrm{L} = \sqrt{D\tau} \tag{2.6}$$

Assuming THz QCL is operated at 77K, τ of GaAs is reported 1ns[49]. D at 300K is 10cm^2/s. Applying Einstein relation and assuming μ_{77K}/μ_{300K}≈10, we can have D_{77K}≈25cm^2/s. Then diffusion length L is calculated ~1.6um for GaAs at 77K.

To sum up, the total broadening will be 2.7λ_0+1.6μm. If pumping light wavelength is 800nm, the total broadening will be ~3.8μm. First order grating period for 3THz frequency is ~15μm. Broadening is comparable to a quarter of a grating period. So diffraction and diffusion will not seriously degrade the index modulation. Actually experimental data indicated that the diffusion length is much shorter than this calculated value hence degradation on modulation is not significant.

2.4.5 Grating coupling strength and pumping intensity

For a DFB grating, its coupling constant κ is given by:

$$\kappa = \frac{2\Gamma\Delta n}{\lambda_0} \tag{2.7}$$

where λ_0 is the free space wavelength of the laser, Γ is the mode overlap factor with the grating. In our case, $\Gamma\Delta n$ induced by optical pumping is proportional to average excessive carrier generated in the active region. For a typical THz QCL cavity length L of 2mm, if ΓΔn=0.05 (corresponds to an average excessive carrier density 2.5×10^{15} cm^{-3}), coupling strength κL at 3THz is calculated to be 2.0, which is strong enough for a DFB grating.[50] Higher coupling strength can be obtained by increasing the pumping intensity.

Excessive carrier density is given by the steady state rate equation:

$$\Delta n_{carrier} = \Delta p_{carrier} = R\tau \tag{2.8}$$

where R is number of photons absorbed per unit volume per unit time. Typical THz QCL cavity dimension is: thickness t=10um, ridge width w=100um and cavity length L=2mm. To induce an average excessive electron density of 2.5×10^{15} cm^{-3}, the pumping power needed is:

$$P = \frac{\Delta n_{carrier} Lwt}{\eta\tau} h\upsilon \tag{2.9}$$

where $h\upsilon$ is the incident photon energy of 800nm near-IR light, η is the transmission through the top metal stripes which is simulated 60%, and τ is minority carrier lifetime

which is 1 ns at 77K. The pumping power is calculated to be 2.1W, which corresponds to an intensity of 1050W/cm^2. 2W of near-IR power can be generated by a semiconductor diode laser. A complete setup of this external tuning method is shown in Fig. 2.26. Projection grating pitch of ~140μm is designed for a THz frequency ~3THz. A laser with 3W of peak power is expected to generate enough coupling to achieve single mode lasing.

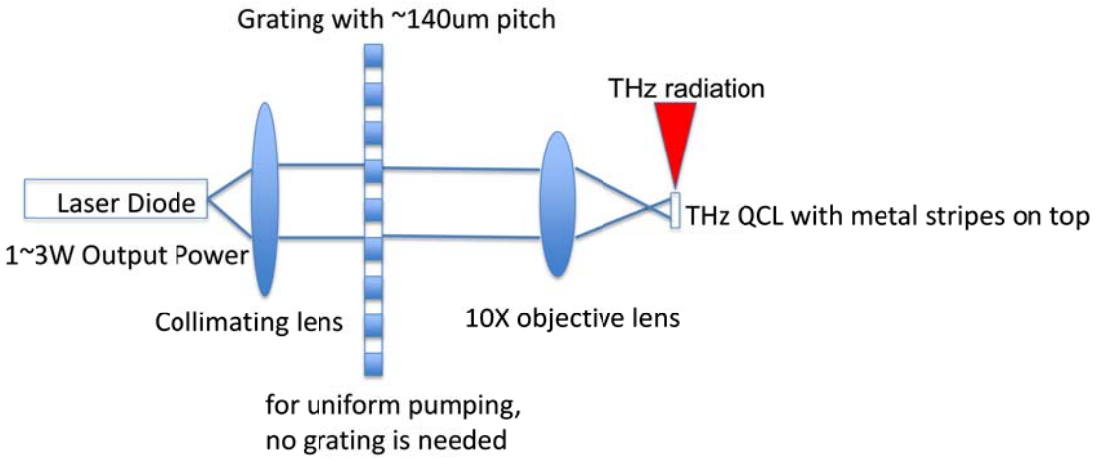

Figure 2.26, Schematic of the entire optical tuning setup for THz QCL. For uniform pumping, grating should be removed

2.4.6 Free carrier absorption: bulk absorption layer

We first applied this method to a metal-metal waveguide device fabricated with the variable barrier height wafer (design 1) described in previous section. Single mode lasing was not observed. Uniform illumination was performed to estimate the excessive carrier density by measuring the wavelength blueshift.[48] Wavelength shift under uniform pumping can be expressed as:

$$\frac{\Delta\lambda}{\lambda} = \frac{\Gamma\Delta n}{n_{modal}} \tag{2.9}$$

where λ is wavelength of lasing mode, $\Gamma\Delta n$ is the effective modal index change, n_{modal} is the modal index. However, wavelength blueshift is not observed. The possible explanation is as follows: Index shift relies on the free carrier response to EM field. In a superlattice structure, electron energy levels are fully quantized so that electrons don't response to longitudinal E-field as free carriers do. As a result, the material index does not follow Drude model. Index of a superlattice structure seems to be insensitive to carrier density according to our results. The entire waveguide of our meta-metal THz QCL is superlattice structure so that lasing wavelength shift upon optical pumping is not observed. Wavelength shift observed in Ref. [48] should be attributed to the presence of bulk InGaAs layer. To solve this problem, we decided to add a 1μm thick GaAs layer on top of active region as shown in Fig. 2.27. Absorption length of pumping light in GaAs is below 500nm so that absorption will mostly occur in this layer to generate free carriers.

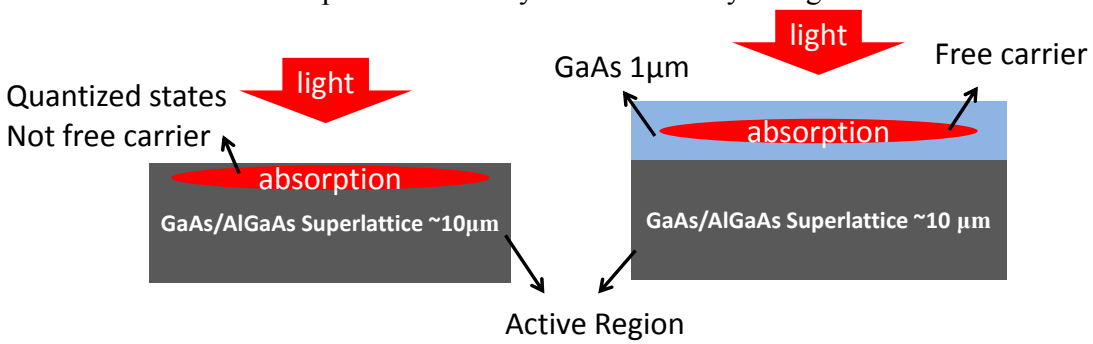

Figure 2.27, Schematic shows the 1μm GaAs layer added on top to absorb pumping light and generate free carriers.

2.4.7 Experimental Results

A THz QCL wafer with top 1μm GaAs layer wafer was grown at University of Leeds by Prof. Linfield Group. We chose a SISP waveguide structure instead of metal-metal waveguide structure. Mode overlap with the grating in a SISP structure is reduced by a factor of ~0.4. But we believe a lower facet reflectivity compared to metal-metal

structure is beneficial for grating wavelength selection. Wafer is grown on a semi-insulating GaAs substrate. The complete structure consists of (from bottom to top) a 250 nm undoped GaAs buffer layer, an undoped 300 nm $Al_{0.5}Ga_{0.5}As$ etch-stop layer, a 600 nm n+ GaAs surface plasma layer (3.5×10^{18} cm^{-3}), 10μm bound to continuum active region similar to design in Ref. [21], 1μm low doped ($5\times10^{15}cm^{-3}$) GaAs layer and 100nm n+ ($5\times10^{18}cm^{-3}$) GaAs contact layer. Wafer is processed into SISP devices with top metal layer patterned into stripe structure describe before (Fig. 2.28). Devices are 200μm wide and 1.5mm long. Testing was carried out in pulsed mode with 40 ns pulses at a 3 kHz repetition rate under 78K. The power was measured with a calibrated helium-cooled Si bolometer. Spectra were measured using a Fourier-transform infrared spectrometer (FTIR). Pumping near-IR light is generated by an 808nm laser diode. Testing setup is as illustrated in Fig. 2.26. Single mode lasing was not observed so only uniform pumping results will be presented (no grating was used in the setup). Wavelength blueshift under uniform illumination was observed. This confirms the effectiveness of GaAs absorption layer. Index shift is found to be too small for a DFB grating. Further improvement is required to produce higher index shift.

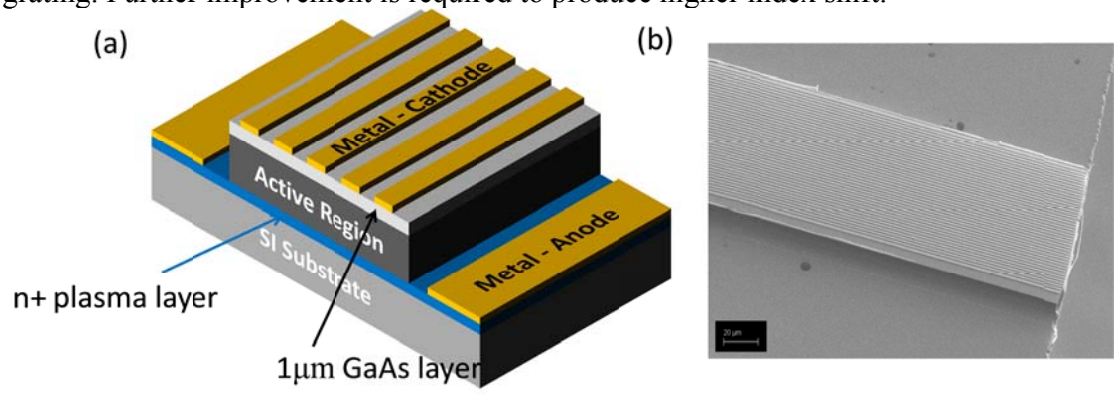

Figure 2.28, (a) Schematic of our SISP device with top GaAs absorption layer and metal stripes. (b) SEM image of our device

Fig. 2.29 shows the comparison of L-I-V characteristics between devices with continuous metal and metal stripes on top. Threshold current increase is less than 10%. Lasing spectra are shown in Fig. 2.30. These results confirm that replacing continuous metal with metal stripes will not seriously degrade device performance.

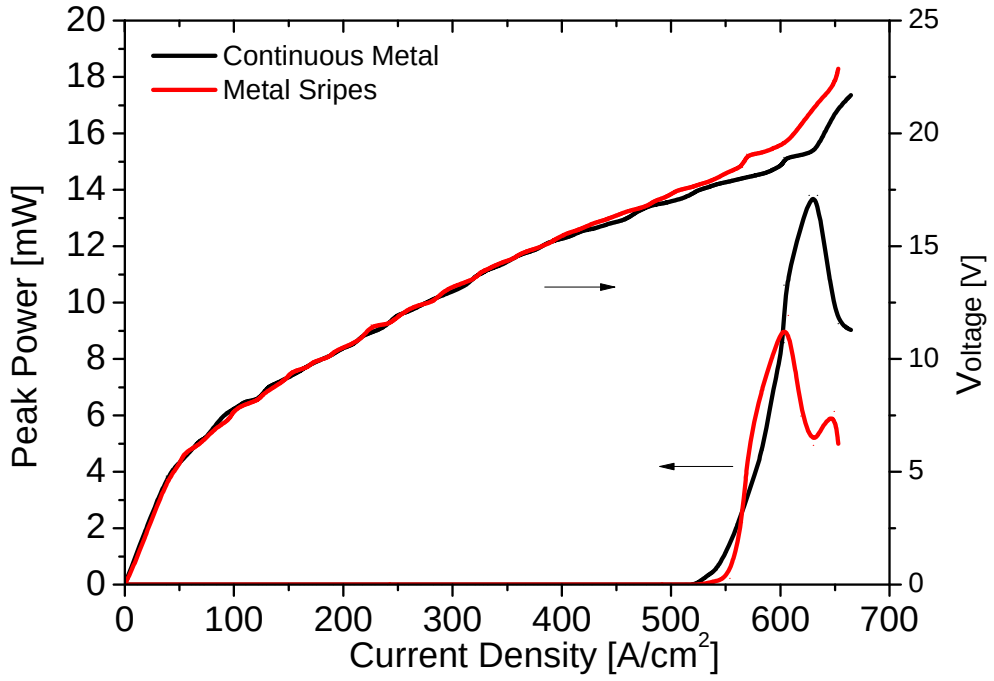

Figure 2.29, L-I-V characteristics of devices with continuous metal and metal stripes on top at 78K.

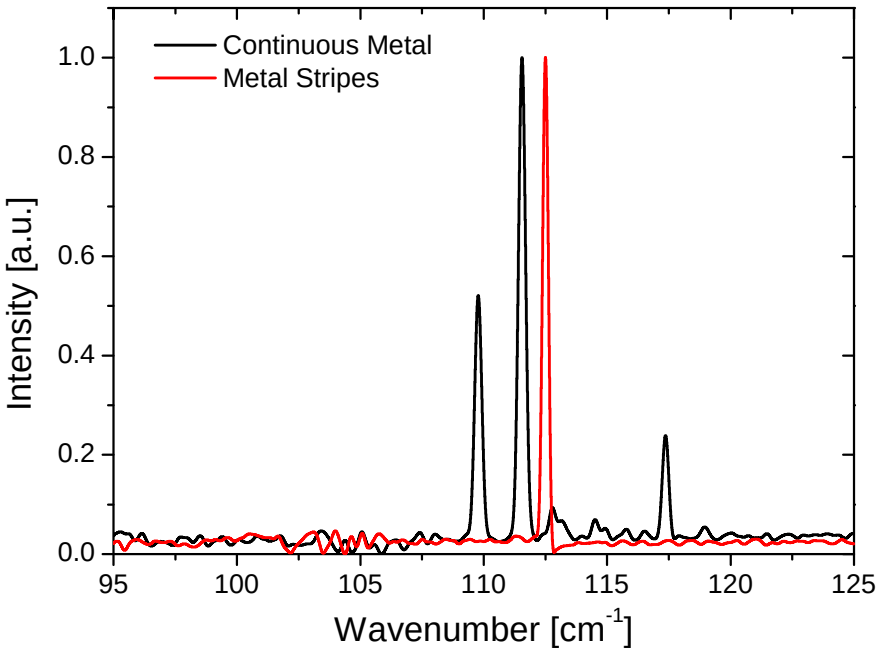

Figure 2.30, Lasing spectra of devices with continuous metal and metal stripes on top at 78K.

Fig. 2.31 shows the wavelength blueshift upon uniform optical pumping. With 3W of incident power, lasing wavelength is shifted by 0.043cm^{-1}. This wavelength shift corresponds to a 0.03% relative index change, which is 15 times lower than expected. This index change is too small to produce a strong enough DFB grating. Plugging these results and other device parameters into Eqn. (2.9), we can have the carrier recombination lifetime τ=67ps. This number is much lower than the number we used for our calculation (1ns). The advantage of short lifetime is shorter diffusion length which relieves grating degradation problem. However, short lifetime significantly reduces the expected excessive carrier density and index shift. This short lifetime could be due to the high field through the entire device. High E-field drives the generated electrons to rapidly leave the laser cavity and results in an ultrashort lifetime. To obtain higher index shift, we need to either increase the pumping power or scale the device dimension down to increase the

pumping intensity. A 30 times enhancement on pumping intensity is required for this method to work based on the data we obtained.

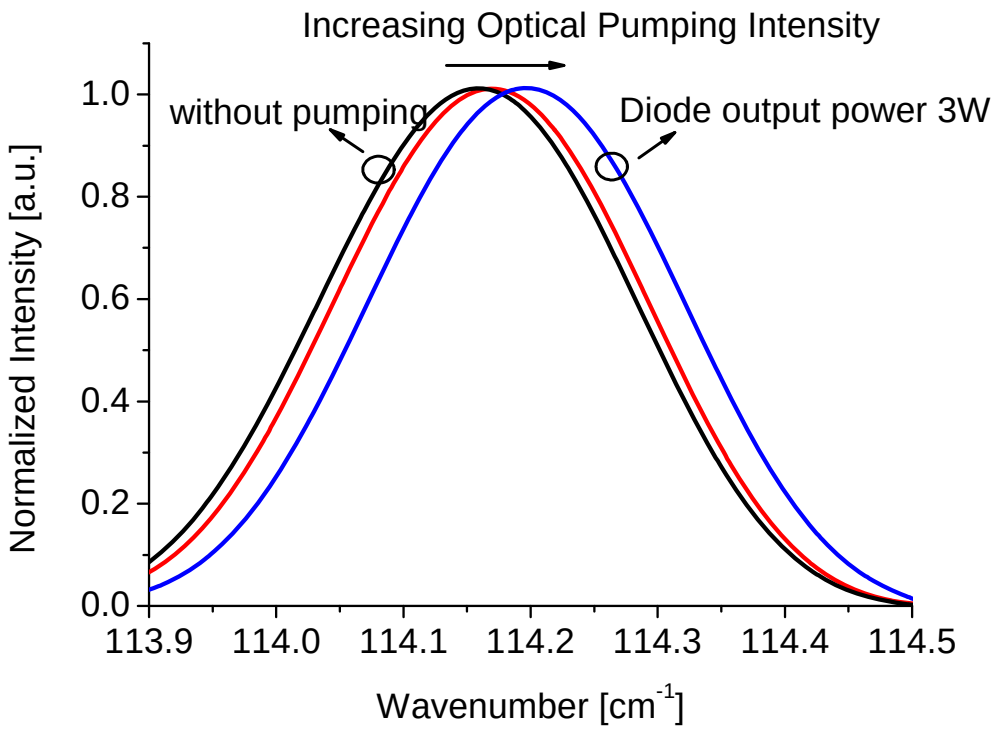

Figure 2.31, Spectra blueshift of a particular lasing mode under different optical pumping level

2.4.8 Summary and future work

To summarize, we proposed a tunable THz QCL setup as shown in Fig. 2.26. Top metal layer of THz QCL is patterned into metal stripes to allow pumping light enter active region. Pumping light is spatially modulated through a projection system. A DFB grating with strong coupling is expected to be generated by this pumping. Tuning can be achieved by either changing the object grating or changing the distance between objective and QCL. Preliminary results show that a 30 times higher pumping intensity is required for this idea to work. In the future work, we need to increase the pumping power and

focus pumping light more tightly on a smaller device. High power laser diode and better focusing optics is required. We believe these improvements will eventually enable us to broadly tune a THz QCL.

Chapter 3: Terahertz Difference Frequency Generation Quantum Cascade Laser Array

Difference frequency generation (DFG) in mid-IR QCL is another candidate for compact THz source with room temperature operation capability. It was first demonstrated by Belkin et al in 2007[23] at low temperature and later improved to room temperature operation.[24] This chapter starts with working principles of THz DFG QCLs. Then our monolithic tunable THz DFG QCL individual device with ~580Ghz tuning range will be presented.[51] Lasing wavelength is tuned by thermally induce refractive index shift via electrical pumping, eliminating any moving parts. We follow the linear array approach to expand the tuning range. We developed an independent current pumping method and successfully improve the individual device yield to almost 100%. A 10-device THz DFG QCL array covering 1.9-3.9 THz was demonstrated.[52]

3.1 THz DFG QCL

3.1.1 Nonlinear Process and Giant Nonlinear Effect in Superlattices

In contrast to THz QCL, high power room temperature cw lasing QCL has been achieved in mid-IR range. QCL active region is inherently an nonlinear medium so that

A portion of this work has been published in 1) A. Jiang, S. Jung, Y. Jiang, K. Vijayraghavan, J. H. Kim and M. A. Belkin, "Widely tunable terahertz source based on intra-cavity frequency mixing in quantum cascade laser arrays," Applied physics letters 106(26), 261107 (2015). A. J. performed device processing and all measurements as well as analyzed experiment data. S. J., Y. J. and J. H. K. helped with device processing. K.V. designed the wafer. M. A. B. supervised the project. 2) S. Jung, A. Jiang, Y. Jiang, K. Vijayraghavan, X. Wang, M. Troccoli and M. A. Belkin, "Broadly tunable monolithic room-temperature terahertz quantum cascade laser sources," Nature Communications 5(2014). S.J. performed device processing all measurement and data analysis. A.J., Y.J. helped with device design and processing. K.V. performed wafer design. X.W and M. T. performed wafer growth. M. A. B. supervised the project.

THz radiation could be generated through nonlinear difference frequency process from mid-IR pumps to THz radiation: $\omega_3 = \omega_1 - \omega_2$, inside a mid-IR QCL. The basis of this idea is the nonlinear response of materials to electromagnetic radiation.

The polarization response of a material to an electromagnetic field is given by:

$$\vec{P} = \varepsilon_0 \chi^{(1)} \vec{E} + \varepsilon_0 \chi^{(2)} \vec{E}^2 + \varepsilon_0 \chi^{(3)} \vec{E}^3 + \cdots \quad (3.1)$$

where ε_0 is vacuum permittivity, $\chi^{(n)}$ is the n^{th} order susceptibility and E is the electric field. High order term is usually negligible and only the first linear term is considered. In the case of high incident intensity, high order terms become significant. Here we are only interested in second term. $\chi^{(2)}$ is common for crystals with no centrosymmetry. Typical high $\chi^{(2)}$ material includes $LiNbO_3$, KDP etc. with $\chi^{(2)}$ in the range of 1-40pm/V. Significant nonlinear effect usually requires a light intensity above 1GW/cm^2.

Considering an incident wave with two frequency components:

$$E = E_1 e^{i\omega_1 t} + E_1 e^{i\omega_2 t} + c.c. \quad (3.2)$$

where E_i is the field amplitude and c.c. stands for complex conjugate. The second term in Eqn. 3.1 is given as:

$$P = \varepsilon_0 \chi^{(2)} ({E_1}^2 e^{i2\omega_1 t} + {E_2}^2 e^{i2\omega_2 t} + 2E_1 E_2 e^{i(\omega_1+\omega_2)t} + 2{E_1}^* E_2 e^{i(\omega_2-\omega_1)t} + c.c.) + 2\varepsilon_0 \chi^{(2)} (E_1 {E_1}^* + E_2 {E_2}^*) \quad (3.3)$$

The fourth term corresponds to the difference frequency generation. The polarization response can be considered as point dipole radiation sources. Radiation at frequency of $\omega_3 = \omega_1 - \omega_2$ should be observed at proper directions that satisfy phase matching condition.

To obtain highly efficient nonlinear process, high field strength (light intensity) and high nonlinear susceptibility are required. In a DFG THz QCL, this process occurs inside mid-IR QCL active region. Light traveling inside a QCL ridge is tightly confined and could reach an intensity of 1MW/cm^2， which could hardly be achieved through

focusing providing same mid-IR power level. Nevertheless, 1MW/cm^2 is still far below typical 1GW/cm^2 intensity threshold for nonlinear optics. This gap is bridged by the most important concept of this device: a QCL active region could be tailored to produce several orders of magnitude higher nonlinearity compare to common nonlinear materials. This giant nonlinearity is an attractive property based on intersubband transition and can be engineered into superlattice structure. As mentioned before, intersubband transition has an atomic like (delta function like) joint density of states. Moreover, spacing between these states can be tuned by changing well thickness. That mean it is possible to prepare a system with energy levels in resonance with incoming wave. When the incoming pumps wavelength aligns with the resonant frequency of a system, the nonlinear response can be dramatically enhanced.

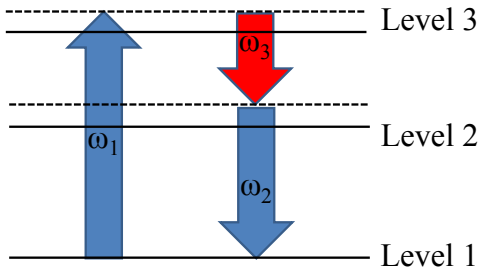

Figure 3.1, (a) Schematic illustrates nonlinear difference frequency process in a 3-level system.

Rigorous expression of $\chi^{(2)}$ can be derived using quantum mechanical perturbation method. The $\chi^{(2)}$ expression of a three level system (Fig. 3.1) is given as:[53]

$$\chi^{(2)}(\omega_3 = \omega_1 - \omega_2) = \frac{e^3}{h^2 \varepsilon_0} \frac{z_{12} z_{23} z_{31}}{\omega_3 - \omega_{32} + i\Gamma_{32}} \left(\frac{N_1 - N_3}{\omega_1 - \omega_{13} + i\Gamma_{31}} + \frac{N_1 - N_2}{-\omega_2 - \omega_{12} + i\Gamma_{21}} \right) \quad (3.4)$$

where ω_i is the photon energy/frequency, ω_{ij} is the transition energy/frequency between level i and level j, ez_{ij} is the dipole transition matrix element, Γ_{ij} is the transition linewidth broadening and N_i is the electron population density of state i. As the photon energies approaches the separations between energy levels, real part in the denominator becomes close to zero and $\chi^{(2)}$ will be greatly enhanced relative to the off resonance case. Typical numbers of $\chi^{(2)}$ in such a quantum well system ranges from 10^4 pm/V to 10^6 pm/V,[26, 54] which is 1000 to 10000 times of the values of common nonlinear materials (1-40 pm/V). With this enhancement, DFG process inside a QCL active region becomes a practical approach to generate THz radiation.

Implementation of the giant nonlinearity in QCL is based on bound to continuum type active region. Bound to continuum design with defect state as upper state and miniband as lower state intrinsically possesses strong nonlinearity for THz DFG and can be further optimized for particular case. An example of active region design is shown in Fig. 3.2. Usually, two different stacks are used. The reason is that the sweet spot i.e. the maximum of nonlinearity is typically around 3-4 THz while a single stack BTC design cannot provide such a broad gain bandwidth. A second stack with shifted spectral gain peak is needed to generate a broad enough gain bandwidth. A dual stack design with two stacked active region designs is shown in Fig. 3.2(b). So far, best performance THz DFG QCLs are mostly based on such dual stack design.

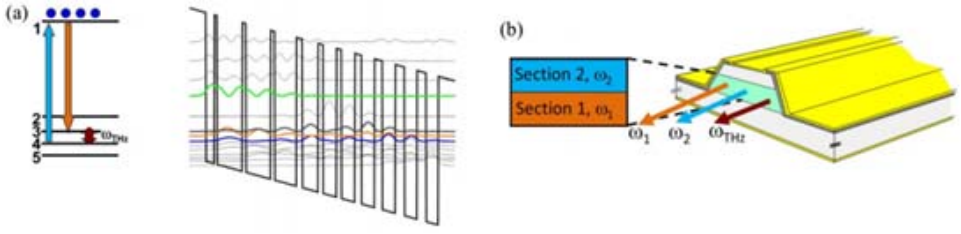

Figure 3.2, Schematic of (a) Active region with integrated giant nonlinearity. (b) Device geometry of THz DFG QCL

3.1.2 Cherenkov Phase Matching[25]

Nonlinear process can be understood in the way that material nonlinear polarization is radiating as dipole antenna array. This antenna array has a phase variation determined by pump waves. To receive the radiation at a direction that these antenna sources constructively add up, a phase matching condition has to be satisfied.

In the case of THz DFG, $\overrightarrow{k_{polarization}} = \overrightarrow{k_1} - \overrightarrow{k_2}$. $\left|\overrightarrow{k_1} - \overrightarrow{k_2}\right| \approx \frac{n_g \omega_{THz}}{c}$ is determined by group index n_g at mid-IR pump frequency. Due to material dispersion, usually $n_g \neq n_{THz}$. Therefore, a phase matching scheme is required. Two phase matching scheme are illustrated in Fig. 3.3. First THz DFG QCL was demonstrated with a collinear modal phase matching scheme (Fig. 3.3(a)). The waveguide structure was engineered to shift n_{THz} to match n_g. Perfect phase matching could be achieved using this approach. However, it suffers from strong free carrier absorption along the waveguide. The power of this process is given by:[53]

$$\mathrm{W}(\omega_{THz} = \omega_1 - \omega_2) = \frac{\omega_{THz}^2}{8\varepsilon_0 c^3 n_1 n_2 n_3} \left|\chi^{(2)}\right|^2 \frac{W_1 W_2}{S_{eff}} l_{coh}^2 \tag{3.5}$$

where l_{coh} is the coherence length given by:[53]

$$l_{coh} = \frac{1}{\left(\left|\overrightarrow{k_{THz}} - \left(\overrightarrow{k_1} - \overrightarrow{k_2}\right)\right|^2 + (\alpha/2)^2\right)^{1/2}} \tag{3.6}$$

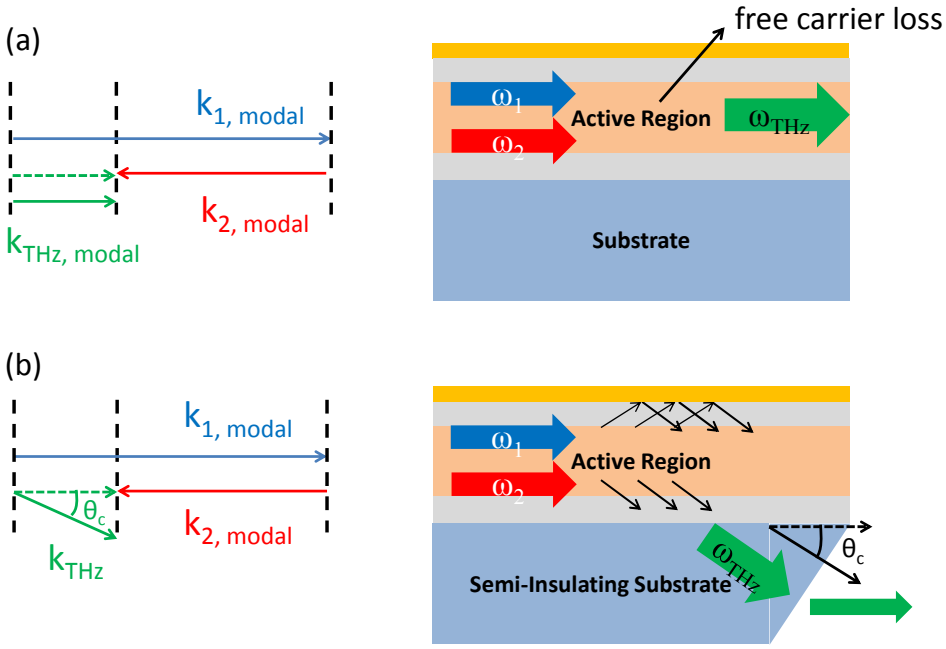

Figure 3.3, Schematic of (a) modal phase matching and (b) Cherenkov DFG extraction scheme. Arrows in (b) indicate Cherenkov radiation towards both top and bottom

W_i, n_i, and k_i are the power, refractive index, and the wave vector of the beam at frequency i, respectively, α stands for the waveguide loss at DFG frequency, and S_{eff} is the effective area of interaction. Even with modal phase matching condition: $\left|\overrightarrow{k_3} - \left(\overrightarrow{k_1} - \overrightarrow{k_2}\right)\right| \approx 0$, l_{coh} is still limited to ~100μm by high THz waveguide loss α due to strong free carrier absorption. Most of the THz power generated is reabsorbed during propagation. To solve this problem, intra-cavity Cherenkov extraction scheme is developed to efficiently extract THz radiation.[25]

Cherenkov radiation refers to the situation that phase velocity/phase variation rate of the radiation source in a medium is faster than the phase velocity of the generated radiation. A constructive phase relation could be obtained at an angle relative to the direction of the source phase velocity. In the case of THz DFG QCL, THz frequency refractive index of InP is higher than the mid-IR group index for the active region, which

means the phase velocity of nonlinear polarization is faster than THz radiation phase velocity in the substrate. Therefore, a Cherenkov phase matching solution exists. As shown in Fig. 3.3(b). THz radiation is emitted at Cherenkov angle θ_C given by:

$$\theta_C = cos^{-1}\left(\frac{|\overrightarrow{k_1} - \overrightarrow{k_2}|c}{n_{Thz}\omega_{Thz}}\right) \tag{3.7}$$

where n_{THz} is the substrate refractive index. THz wave is emitted into to the substrate (also towards the top, shown in Fig. 3.3(b)). A side current injection scheme is used so that we can use semi-insulating substrate to eliminate free carrier absorption (Fig. 3.4(a)). Since Cherenkov wave towards the ridge top will reflect back, active region thickness need to be carefully engineered to avoid destructive interference. To extract THz wave, substrate is polished at the end (Fig. 3.3(b)) to avoid total reflection. Typical θ_C is around 20° . Substrate is usually polish at 30° to refract THz radiation to the forward direction.

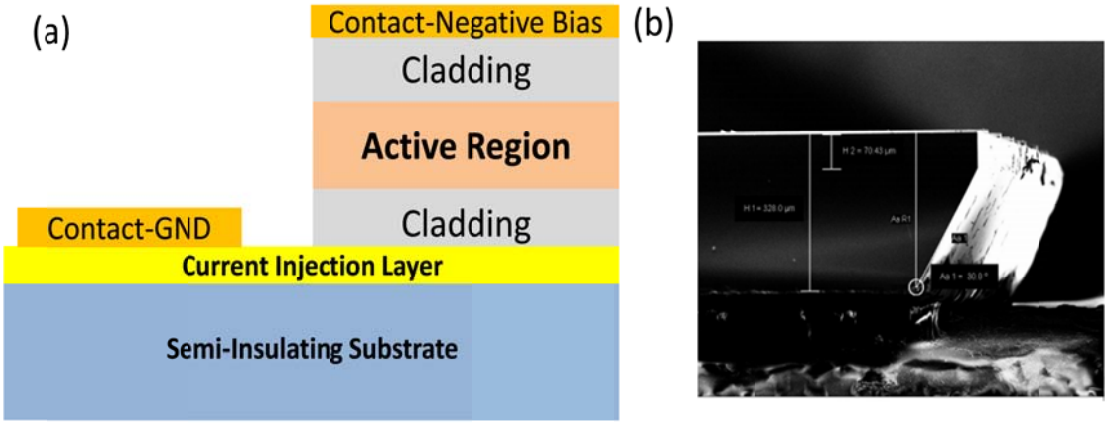

Figure 3.4, (a) Schematic of side current injection scheme (b) SEM image of a Cherenkov THz DFG QCL with polished substrate

With this Cherenkov phase matching, the THz power output is improved by approximately a factor of 10.[25] Moreover, by using Cherenkov phase, the phase

matching condition is relaxed. For modal phase matching, phase matching condition can only be satisfied within a small spectral range. As a result, a widely tunable THz DFG QCL becomes possible with Cherenkov phase matching.

3.2 MONOLITHIC TUNABLE THZ DFG QCL

Spectral tuning of DFG QCL from 1 to 6 THz[29] has been demonstrated by fixing one mid-IR frequency with DFB grating and tuning the second frequency using an external diffraction grating. It could also be achieved using dual external grating setup.[55] However, this system is bulky and requires precise alignment of optical component. A monolithic source is always desired because it is compact and reliable. Our group demonstrated a monolithic THz DFG QCL with 580 GHz tuning range.[51] The device is electrically tuned with no moving parts.

3.2.1 Dual Wavelength Lasing

FP mode devices without wavelength selection scheme emit multiple wavelength in mid-IR hence multiple wavelength THz emission. The commonly used DFB grating for diode lasers is also used for mid-IR QCL as a built-in wavelength selection solution. To obtain single mode THz emission, two mid-IR pumps are needed for DFG. Two gratings with different grating period need to be fabricated on one device ridge to achieve dual wavelength lasing. Mixed grating is another approach,[56] which is not of interest here. Conventional buried DFB grating based DFG QCL has been demonstrated[57]. In contrast to buried DFB grating, our device is based on surface DFB grating,[26] which has different working principle and has a number of advantages. Details of surface DFB grating will be discussed in Chapter 4.

Typical device structure and lasing spectra are shown in Fig. 3.5. Two surface DFB gratings are usually designed at the optimal depth around 140nm and fabricated to one device ridge. Two mid-IR wavelengths are designed symmetrically distributed relative to the gain bandwidth to achieve balanced mid-IR pump power. Laser is lasing in dual color mode and single mode THz radiation is obtained.

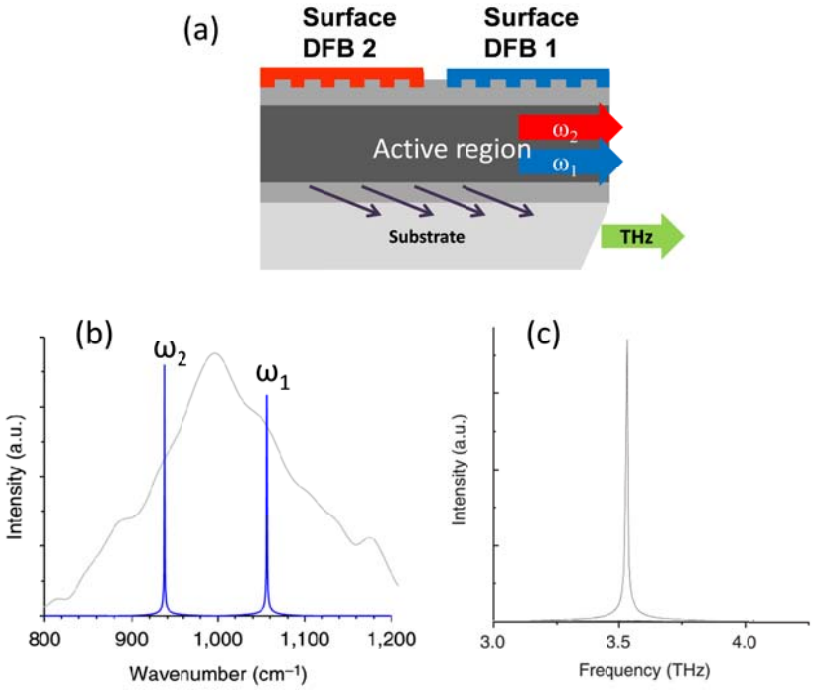

Figure 3.5, (a) Schematic of our THz DFG QCL geometry with two surface DFB grating sections (b) mid-IR lasing spectrum, grey line is the gain spectrum (c) THz emission spectrum

3.2.2 Thermal Tuning through Local DC Current Heating

THz frequency is determined by the two difference of mid-IR pumps, so tuning THz requires tuning ω_1 and ω_2 independently. Monolithic tuning is usually done by carrier injection or thermal effect induced refractive index change. In such a dual grating

device, to tune one pump without affecting the other one, local heating by current injection is needed.

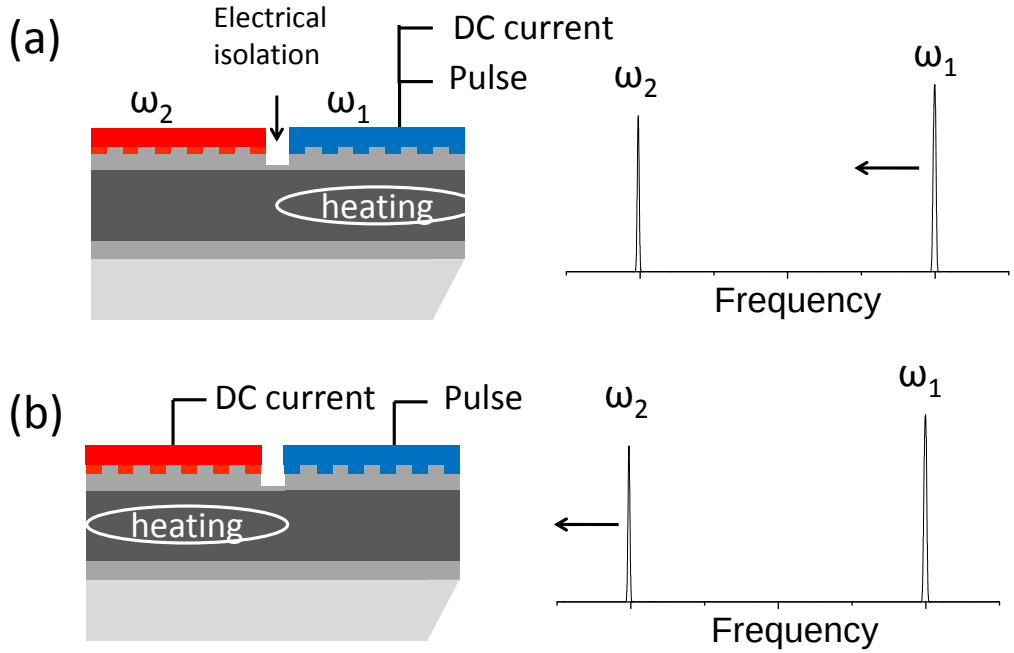

Figure 3.6, (a) DC current is applied to front section. High frequency mid-IR pump redshifts. (b) DC current is applied to back section. Low frequency mid-IR pump redshifts.

Our proof-of-principle device geometry is shown in Fig. 3.5. It consists of two sections: the 1.2 mm long front section with a grating designed to select high ω_1 mid-IR pump frequency and the 1.2 mm back section with the grating designed to select low ω_2 pump frequency. The two sections are separated by a 300μm gap etched through the heavily doped top waveguide layer to electrically isolate two sections. So each section in Fig. 3.5(a) can be independently biased. The laser is operated by applying pulsed current to the front section only (designed for ω_1). The back grating section is left passive. Tuning is achieved by applying DC bias to either the front or the back section.

As shown in Fig. 3.6, redshift of THz emission frequency is done by applying DC current to the front section to redshift the high-frequency mid-IR pump while blueshift is done by applying DC current to back section to redshift the low-frequency mid-IR pump. Achieved THz tuning results are shown in Fig. 3.7(a). A total tuning range of 0.58 THz or over 15% of THz center frequency is achieved in our devices. The red oval indicates the mode hop gap, which happens when applying DC current to back section. To fill this gap and achieve the fine tuning, a second DC bias was applied to the front section to shift the high frequency mode towards the long wavelength side. Continuous single-mode tuning near the mode-hope points is achieved as shown in the inset of Fig. 3.7(b).

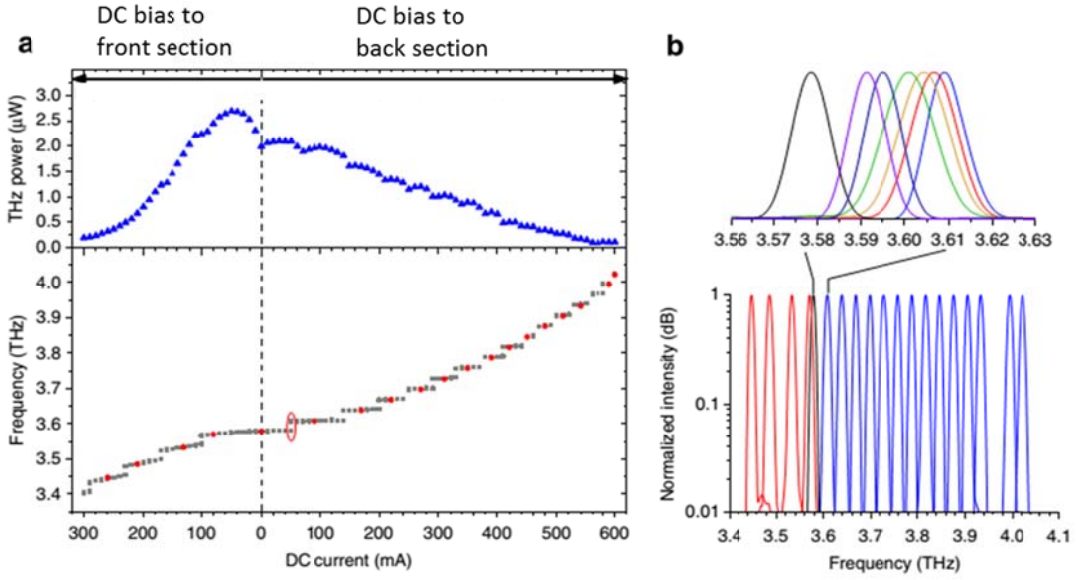

Figure 3.7, (a) Details of THz emission tuning (bottom) and peak THz power (top) of the device as a function of DC current applied to either front or back section. Red circles are experimentally measured positions of THz emission frequencies as shown in (b). The red oval indicates the mode hop gap filled by the fine tuning shown in (b). (b) Electrical tuning of THz emission. Shown are THz spectra for various DC biases applied to the back section (blue) or front section (red). THz emission spectrum from a device without DC bias applied is shown in black. Top inset: Fine tuning of THz emission around the mode-hop point. Adapter from Ref. [51]

3.3 BROADLY TUNABLE SOURCE: THZ DFG QCL ARRAY

To expand the spectral coverage, we demonstrate a compact monolithic terahertz source continuously tunable from 1.9 THz to 3.9 THz with the maximum peak power output of 106 μW at 3.46 THz at room temperature.[52] The source consists of an array of 10 THz DFG QCLs described in previous section. To increase fabrication yield and achieve high THz peak power output in our devices, a dual-section current pumping scheme is implemented using two electrically isolated grating sections to independently control gain for the two mid-IR pumps.

3.3.1 THz DFG QCL Array

There are different approaches to increase tuning range. THz DFG-QCLs with larger tuning range of 2.6-4.2 THz were demonstrated by Razeghi group using a three-section device configuration with one section controlling the wavelength of one mid-IR pump via a distributed Bragg reflector grating and the other two sections providing tuning of the second mid-IR pump based on Vernier tuning mechanism in a sampled grating.[58] We note that single-mode operation of tunable QCLs based on sampled gratings is very challenging and the side mode suppression ratio in these devices is typically worse than 10-20 dB.[59, 60]

We follow the QCL array approach, first demonstrated for monolithic mid-IR tuners,[51] to produce monolithic THz source with continuous spectral tuning from 1.9 to 3.9 THz. We integrate 10 monolithic THz DFG-QCL tuners, (Fig. 3.8) each designed for a slightly different center THz emission frequency, in a single laser array.

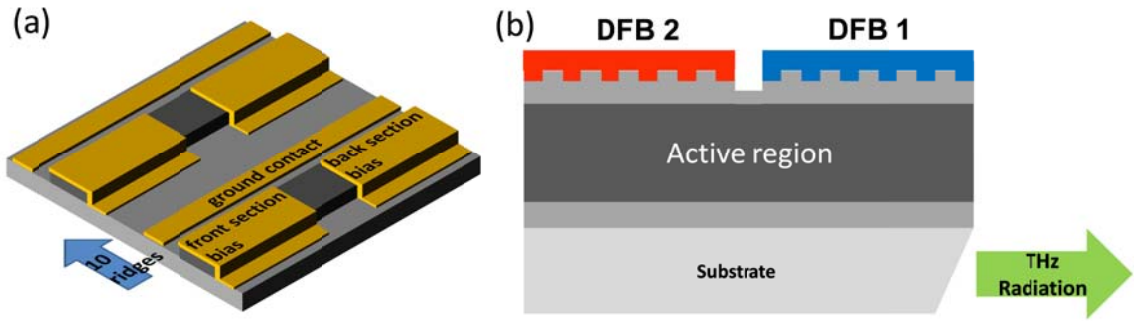

Figure 3.8, (a) Schematic of a 10-ridge THz DFG-QCL array (only two ridges are shown). (b) Schematic of an individual device structure with the two DFB section and the direction of THz output shown.

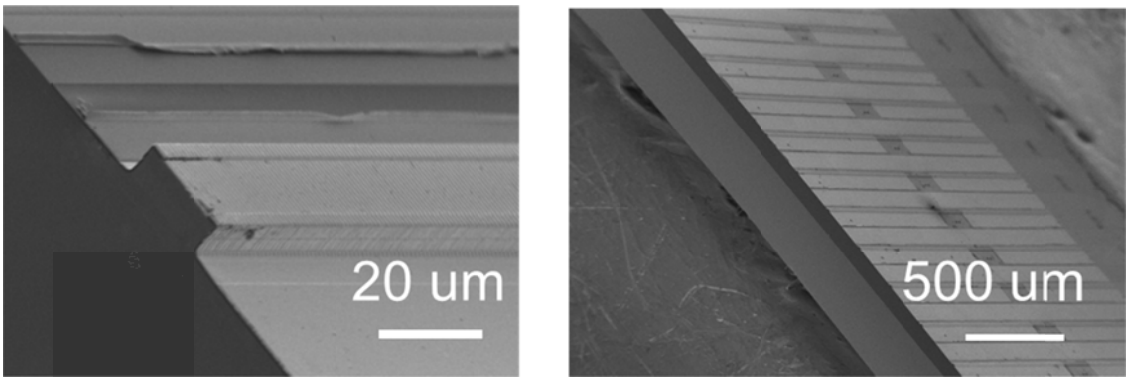

Figure 3.9, SEM images of (a) an fabricated individual THz DFG-QCL device and (b) fabricated THz DFG QCL array.

Figure 3.9 shows the SEM image of a THz DFG-QCL array. The array consists of ten 22-μm-wide ridge-waveguide THz DFG-QCLs, each designed to emit at a specific THz frequency spanning 1.9-3.9 THz range. The structure of an individual device in the array is shown in Fig. 3.8(b). All devices are based on surface DFB grating. Grating periods are in the range from 1.4 μm to 1.6 μm; grating duty cycle is set to 50%. The gratings are defined in the top cladding layer and are approximately 145 nm deep. Such etching depth was computed to provide nearly the same coupling constant of ~11 cm^{-1} for both mid-IR pumps, based on the analysis in Ref. [61]. The grating in the front section of

the device is designed for short wavelength (ω_1) mid-IR pump selection and the grating at the back section is designed for long wavelength (ω_2) mid-IR pump selection. Each grating section is 1.2-mm-long and the two sections are separated by a 300 μm gap for electrical isolation.[51]

The device wafer is grown by a commercial foundry on a semi-insulating InP substrate. The layer sequence is similar to that of the devices reported in Ref. [26]. An array of ridge waveguide devices with two surface DFB gratings and Cherenkov extraction scheme is fabricated. Devices are tested at room-temperature with 70 ns current pulses at 40 kHz repetition frequency. Mid-IR and THz power are measured using thermopile and calibrated bolometer, respectively, from the front facet using a nitrogen-purged setup with two 2-inch-diameter off-axis parabolic-mirrors: one with focal length of 50 mm to collimate the light from the device and the second one with 100 mm focal length to refocus the light onto the detector. Recorded mid-IR power is corrected for an estimated 70% collection efficiency of our setup; THz power is not corrected for any collection efficiency. Fourier-transform infrared spectrometer (FTIR) is used for spectral measurements.

3.3.2 Independent Control of Gain

Dual-wavelength mid-IR lasing is required to produce THz DFG output. Due to gain competition, dual color DFB lasing requires very similar threshold gain for both of frequencies, which is difficult to achieve in practice.[29] To fabricate a 10-element DFB THz DFG-QCL array fabrication with any reasonable yield, we need to be able to fabricate individual dual-color devices with nearly 100% yield. To that end, we implement independent control of the net gain for the two mid-IR pumps in our devices

using the configuration shown in Fig. 3.10. The two grating sections shown in Fig. 3.10 are connected to 50-Ω coaxial power lines in series with 50 Ω resistors that provide

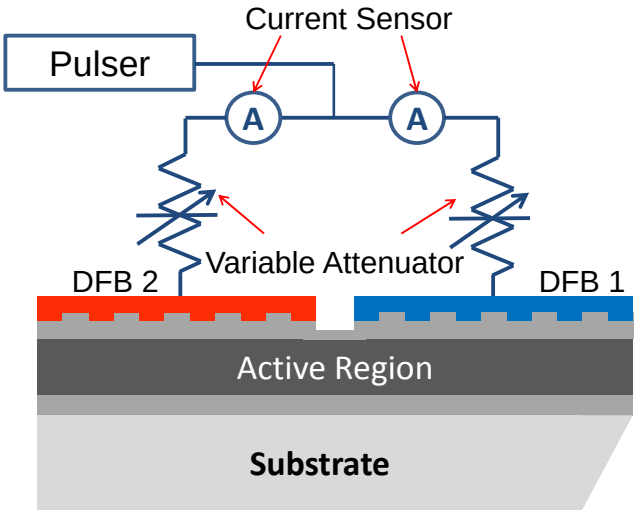

Figure 3.10, Device biasing scheme. Shown are the front DFB section for the short wavelength mode selection (right), the back DFB section for the long wavelength mode selection (left), and the electrical biasing scheme with variable attenuators. Power and spectrum measurements are all taken from the right facet.

impedance matching (differential resistance of QCLs at operating bias is only a few Ohms). The power lines are connected to the power supply through 50-Ω-impedance-matched variable attenuators.[62] The power supply is made of a DEI HV1000 pulse generator (IXYS Colorado Corp.) connected to a 1000V DC voltage source (Kepco Corp.). Current are measured using coil current sensors. In this biasing configuration, we can control the portion of current from the power supply that goes to the front and back device section by adjusting attenuation values on the two attenuators.

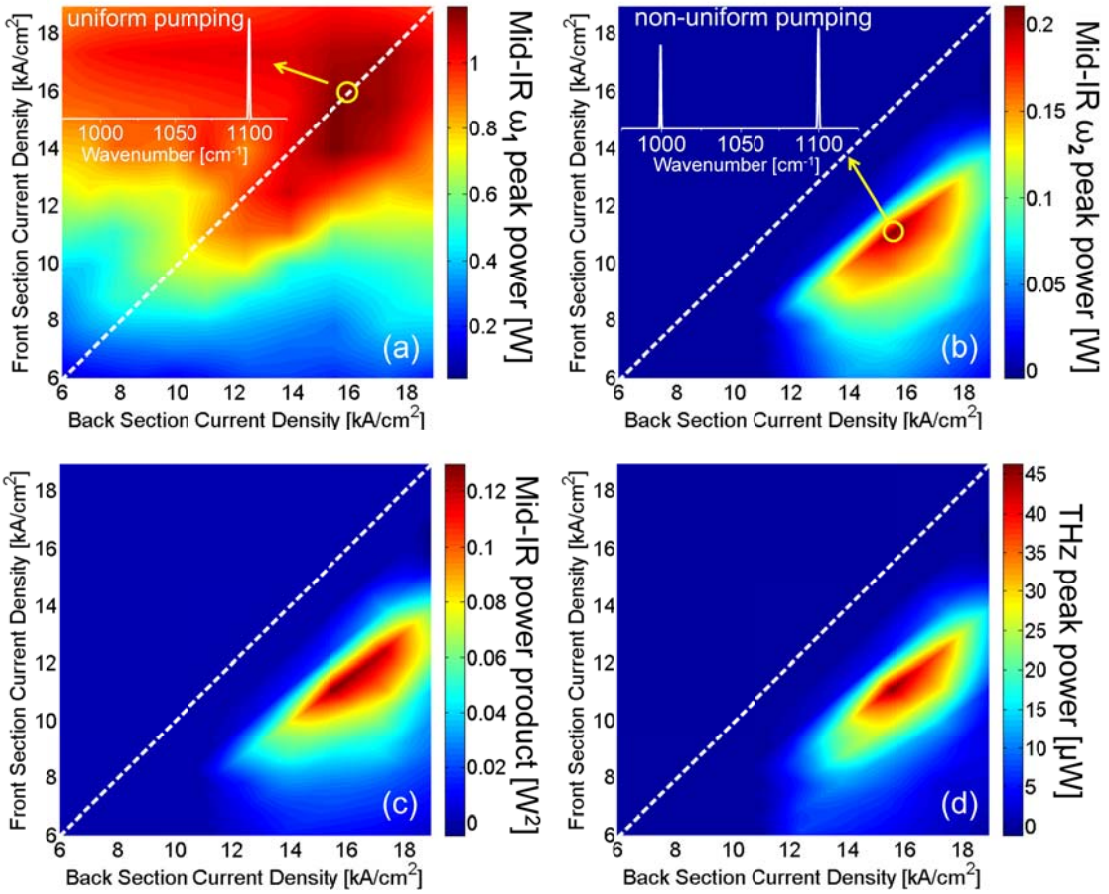

Figure 3.11, (a) Peak power output of the short-wavelength mid-IR pump, (b) peak power output of the long-wavelength mid-IR pump, (c) the product of the peak powers of the two mid-IR pumps, and (d) peak THz power output as a function of current density through the front and back sections of the device #6 in the array. White dashed line in (a)-(d) corresponds to the uniform current pumping situation. Insets in panels (a) and (b) display mid-IR emission spectra of the device for the injection current densities through the front and back section indicated by yellow circles in the panels.

Independent control of the current density through the two grating sections is crucially important to enable dual-color lasing with high yield. Figure 3.11(a-d) plots the power of mid-IR pumps, collected from the front facet of the device, and THz output for device #6 in the array designed for emission at 3 THz. This device performance is typical for the other elements in our array. Panels 3.11(a) and 3.11(b) show the power of the

short wavelength (ω_1) and long wavelength (ω_2) mid-IR pumps, respectively, as a function of current density through the front and back sections of the device. Mid-IR inference filters (Spectrogon, Inc.) were used to separate the pump powers. Figure 3.11(a) indicates that the device predominantly lases at the short wavelength ω_1, which implies that the threshold gain at ω_1 is lower than that at ω_2. White dashed line in all the panels in Fig. 3.11 represents the uniform current pumping condition (same current density for both sections) and only one mid-IR pump is lasing in this case. To enable dual-color mid-IR emission, we need to apply different current bias to the front and the back section as shown in Fig. 3.11(b). To provide further detail of the device mid-IR performance, insets in Fig. 3.11(a) and 3.11(b) show the emission spectra of the laser for the case of uniform pumping density at 16 kA/cm^2 and non-uniform pumping density with 12 kA/cm^2 pump current through the ω_1 DFB section and 16 kA/cm^2 pump current through the ω_2 DFB section, respectively. Figures 3.11(c) and 3.11(d) show the product of the two mid-IR output powers and the power of THz output of the device #6 as a function of the current density through the two DFB sections. As expected, THz radiation is generated only when both mid-IR pumps are lasing. Maximum THz power is measured to be 46 μW for this device.

To understand the results in Fig. 3.11 we note that the mid-IR modes ω_1 and ω_2 only interact strongly with front and back gratings, respectively. Neglecting feedback from cleaved mirrors ω_1-mode is expected to be localized predominantly in the front DFB section, while the mode at ω_2 is expected to be localized predominantly in the back DFB section. Thus, stronger electrical pumping of the front (back) section is expected to predominantly increase the round-trip gain of the ω_1 (ω_2) pump. The feedback from the cleaved facets, which are uncoated in case of our devices, may distort the mode distribution.[51, 63] Detailed theoretical analysis of our device performance in this case is

beyond the scope of this paper. We note, however, that even in the presence of facet reflections, the ω_1- and ω_2-mode distribution along the laser waveguide is expected to remain dissimilar and the two modes are expected to benefit differently from the front- and back-section pumping.

Similar search of optimal combination of pump current densities through the two DFB sections for maximum THz output is performed for other devices in the array. As a result, dual-color lasing and THz output is achieved for all devices in the array. We emphasize that fewer than 50% of our devices showed dual-color mid-IR emission under uniform pump density and thus dual-section pumping was crucial for high yield THz DFG-QCL array fabrication.

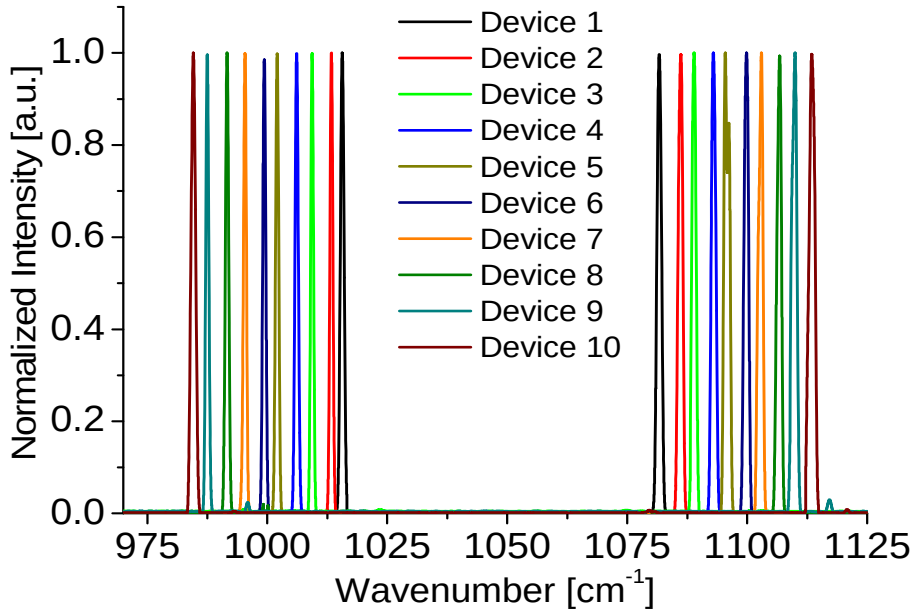

Figure 3.12, Normalized mid-IR emission spectra of all 10 devices in the array recorded at optimal currents densities through the two DFB sections in each device.

Fig. 3.12 plots the mid-IR lasing spectra of the entire 10-ridge array. The mid-IR pump frequencies are selected so as to produce THz emission lines spaced by

approximately 210 GHz. Spectral tuning of mid-IR frequencies ω_1 and ω_2 and hence THz frequency $\omega_{THz}=\omega_1-\omega_2$ is achieved by applying DC bias current to either the front or the back DFB section of the device through a bias tee as described in Ref. [51]. Fig. 3.15 shows the THz emission of all devices in the array with zero DC bias (solid lines) and with DC bias applied to front section only (dashed lines) so as to produce THz emission precisely in-between the emission lines of the array at zero DC bias. Maximum THz output for each line is also shown. Maximum THz peak power from the array was recorded to be 106 μW for a device #8 at zero DC tuning bias with a mid-IR-to-THz conversion efficiency of 0.4 mW/W^2, similar to that observed in external-cavity THz DFG-QCL systems.[29] Mid-IR L-I-V characteristic of device #8 under uniform current pumping condition is shown in Fig. 3.13. Fig. 3.14 plots the THz output and THz conversion efficiency vs current for device #8 under uniform current pumping condition. Fig. 3.16 shows continuous tuning capability of our array source. Fig. 3.16(a) shows emission spectra of the device #8 for different DC tuning bias currents applied to the front DFB section. Tuning range is wide enough to cover the gap between the emission frequencies of the two adjacent devices in the array. Figure 3.16(b) shows further details of the DC current tuning around the circled region in Fig. 3.16(a). As discussed in Ref. [51], due to cleaved facet reflectivity, mid-IR pumps experience mode-hoping which leads to a gap in THz frequency tuning. As further described in Ref. [51], continuous THz tuning can still be obtained by applying a second DC bias to the back DFB section. The experimental demonstration is presented in Fig. 3.16(c).

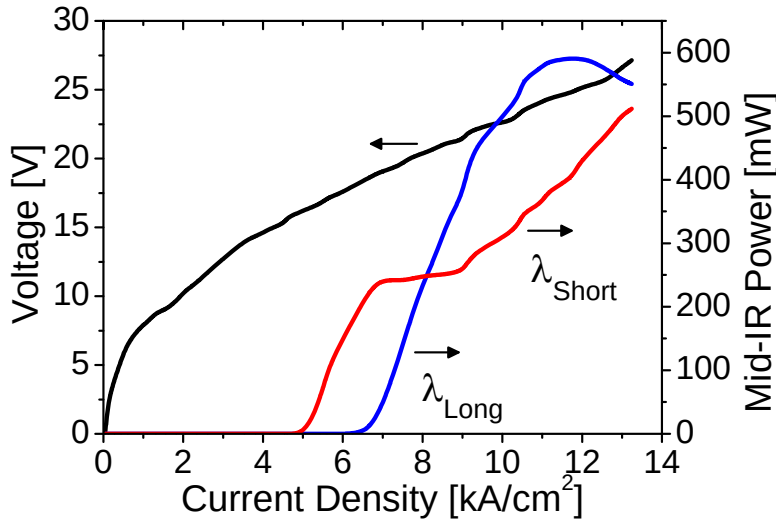

Figure 3.13, Two Mid-IR pump output power vs current and current – voltage characteristic of device #8 under uniform current pumping condition (designed for DFG emission at 3.46 THz at zero DC bias).

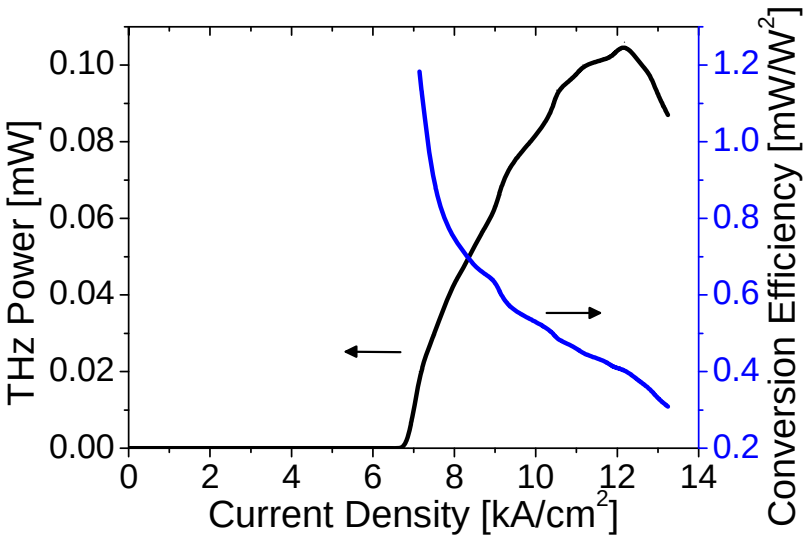

Figure 3.14, THz output and THz conversion efficiency vs current for device #8 under uniform current pumping condition.

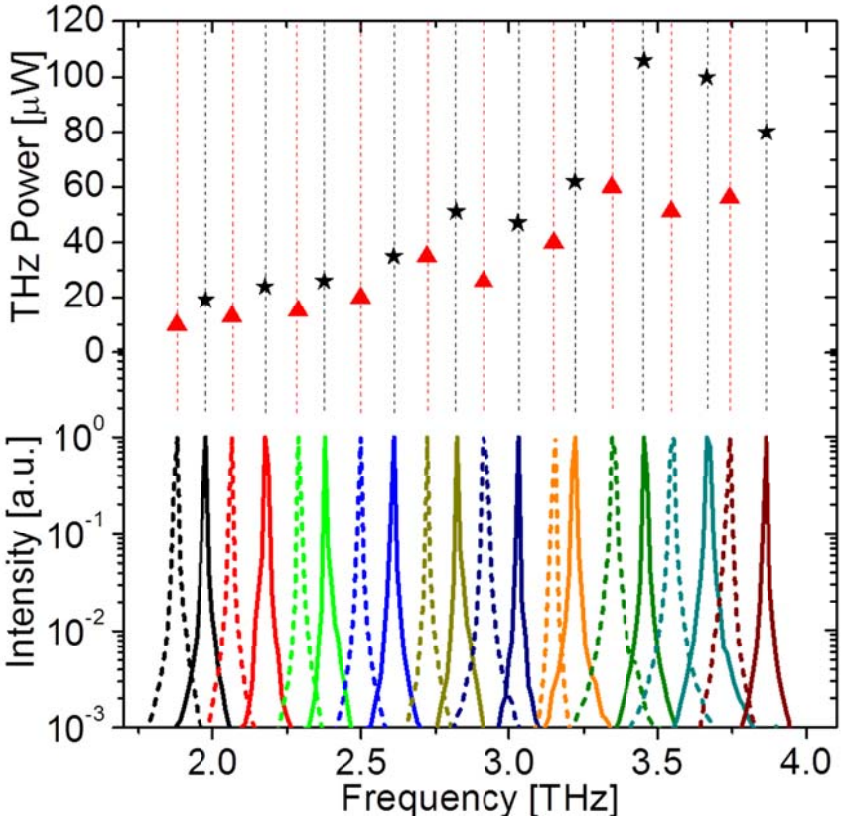

Figure 3.15, THz emission spectra (bottom panel) and the maximum THz peak power (top panel) for all devices in the array without applying DC bias for tuning (solid lines and stars) and with DC tuning bias applied to the front grating section so as to produce THz emission in-between the emission lines of the array at zero DC bias (dashed lines and triangles).

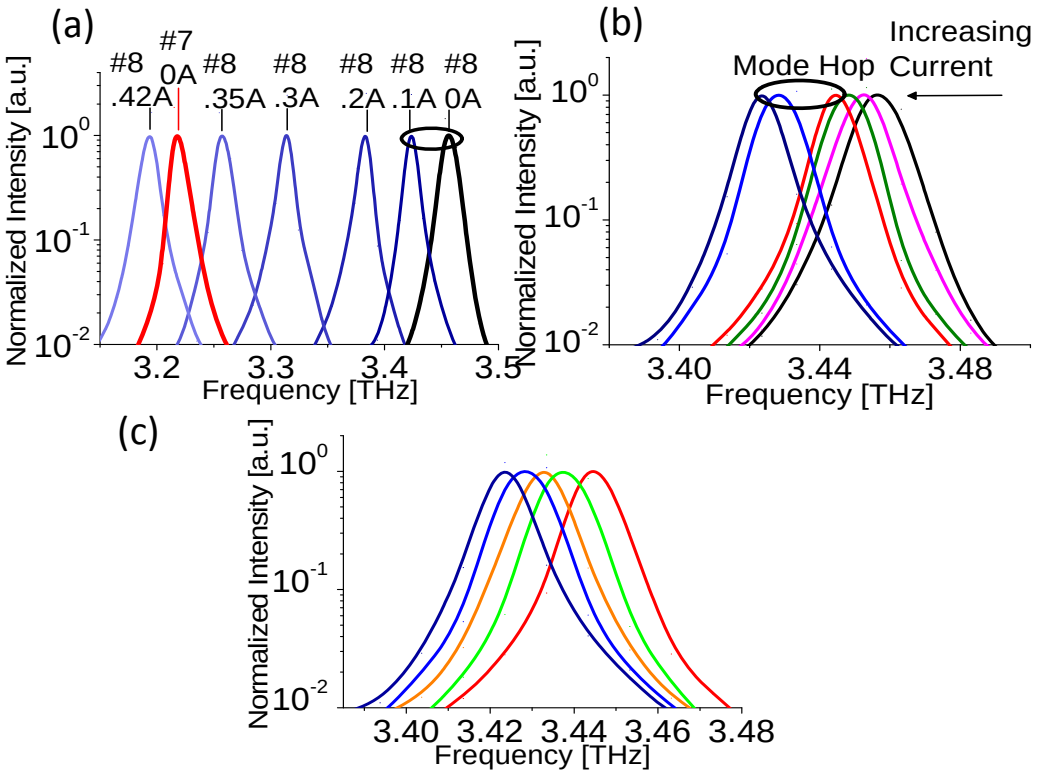

Figure 3.16, Mode-hope free THz tuning using device #8 in the array as an example. (a) Emission spectra of device #8 in the array for different values of DC tuning current though the front section. Also shown is the THz emission spectrum of the adjacent device #7 at zero DC tuning current. (b) THz tuning behavior of device #8 around the region circled in panel (a). Mode hoping is observed around 3.43 THz. (c) Mode-hope-free tuning of device #8 within the circled region shown in (b) by applying DC bias to both the front and the back DFB sections of the device #8. From left to right, the spectra shown in (c) correspond to the front/back DC tuning current of 110 mA/0 mA, 100 mA/0 mA, 100 mA/50 mA, 140 mA/100 mA, and 90 mA/0 mA.

3.3.3 Summary and future work

To summarize, we demonstrated continuously-tunable monolithic room-temperature THz DFG-QCL source made of an array of 10 DFG-QCL devices. Independent current pumping scheme for two grating sections was implemented to enable

dual-color mid-IR pump emission in all devices in the array with nearly 100% yield. The array achieves the maximum THz peak power output of 106 μW at 3.46 THz and provides continuous spectral coverage between 1.9 and 3.9 THz. Further improvement of tuning range is expected by increasing the number of lasers in the array and/or by further increasing the frequency spacing between the emitters in the array. We expect that, similarly to tunable mid-IR sources based on QCL arrays,[64-66] tunable THz sources based on this technology will provide a compact low-cost THz source option for spectroscopic applications.

Chapter 4: Longitudinal Integration of Single Mode mid-IR Quantum Cascade Lasers

Widely tunable mid-IR is equally important as THz range for sensing and spectroscopy applications. Owing to the great success of QCL in mid-IR range, compact and convenient QCL sources are as mature as near-IR diode lasers. Widely tunable source has been demonstrated in various ways: linear array of DFB devices,[67] multi-section sampled-DBR devices,[60, 68] external cavity tuned devices,[69, 70] surface emitting arrays[66] etc. Among these, array source is the simplest for fabrication. This chapter describes our work on improving both yield and far field of linear QCL array using our surface DFB grating, independent current pumping and longitudinal integration scheme. This is inspired by our results from THz DFG QCL. Surface DFB grating improves wavelength selection yield to almost 100%. On the other hand, independent current pumping enables a single ridge to emit different wavelength upon pumping condition, which helps to reduce device number in an array and improve far field. Surface DFB grating coupling mechanism as well as its design procedure will be discussed in this chapter. Array of mid-IR QCLs which can emit more than one wavelength (one at a time) is demonstrated, using surface DFB grating and a longitudinal integration scheme.

4.1 Broadly Tunable Mid-IR QCL Source Overview

Broadly tunable mid-IR sources are necessary for spectroscopy applications. Currently, mid-IR QCL active region can be designed to produce a gain bandwidth of ~600 cm^{-1}.[71, 72] Tunable source research is mostly focused on the aspect of tuning method and solution. Most widely tunable result is demonstrated with an external grating.[69, 70] In these systems, QCL is incorporated with an external cavity with a rotating

diffraction grating that provides tunable single wavelength operation. These systems are bulky, complicated and require high quality antireflection coating and precise alignment. A monolithic source is always preferred. Multi-segment QCL based on vernier effect between two sampled DBR gratings are demonstrated with over 200 cm^{-1} of tuning range.[68] However, due to its complexity, yield is limited by mode hopping and fabrication challenge. Linear array of DFB devices with different design wavelength is the most straightforward solution.[67, 73] 32-device array covering 90 cm^{-1} has been demonstrated with over 95% yield. Fig. 4.1 shows the 32-device array SEM image and lasing spectra. Peak power of this array is ~25mW. Recently, an array of surface emitting QCL has been demonstrated based on DBR gratings and a second order extractor.[66] Output power of this surface emitting array requires further improvement.

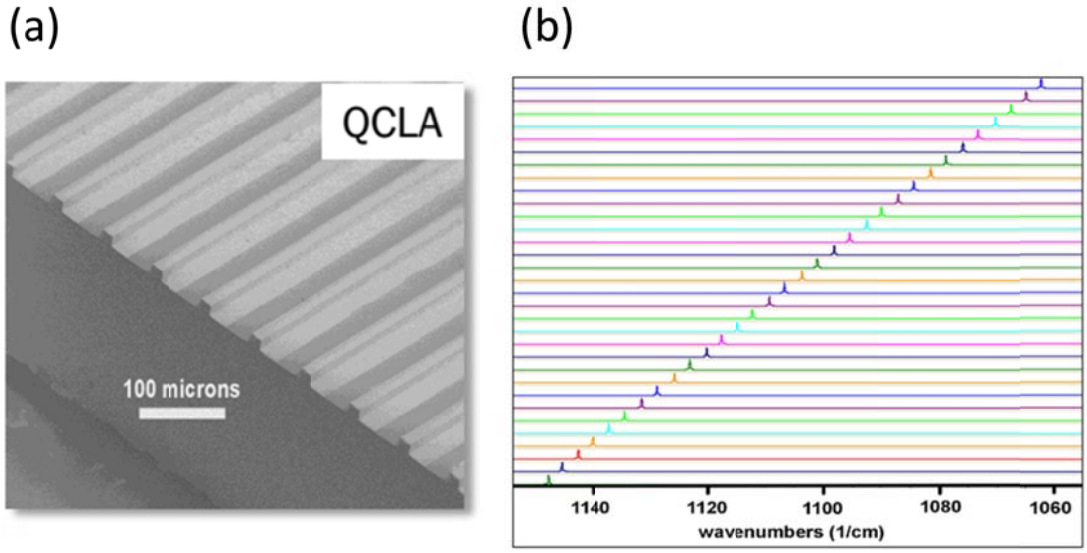

Figure 4.1, (a) SEM image of a 32-device QCL array (b) lasing spectra of 32-device QCL array. Adapted from Ref. [67]

4.2 SURFACE DISTRIBUTED FEEDBACK GRATING

Linear array shown in Fig. 4.1 is the simplest solution for broadly tunable monolithic source. Ref. [67] describes the design and fabrication to build a DFB QCL array with high yield. Accurate placement of lasing wavelength is the key for success. Buried DFB grating inherently has two degenerate modes so that additional discrimination mechanism is required for reliable wavelength selection. We use surface DFB gratings instead of buried grating. In the THz DFG QCL array work, we observed that wavelength selection yield is close to 100% for surface grating, which is highly desired for array construction. Moreover, cladding regrowth is not necessary for a surface grating device. The effectiveness of surface DFB grating is a unique feature of mid-IR QCL. The working principle and design rule will be presented.

4.2.1 Buried DFB grating and mode degeneracy

For conventional buried DFB grating, as shown in Fig. 4.2(a), periodic corrugation is fabricated into the waveguide layer near the active region. The grating has to be buried close the waveguide core to enhance interaction with light and produce enough coupling. So a cladding layer regrowth is always needed which makes the device fabrication complicated and costly.

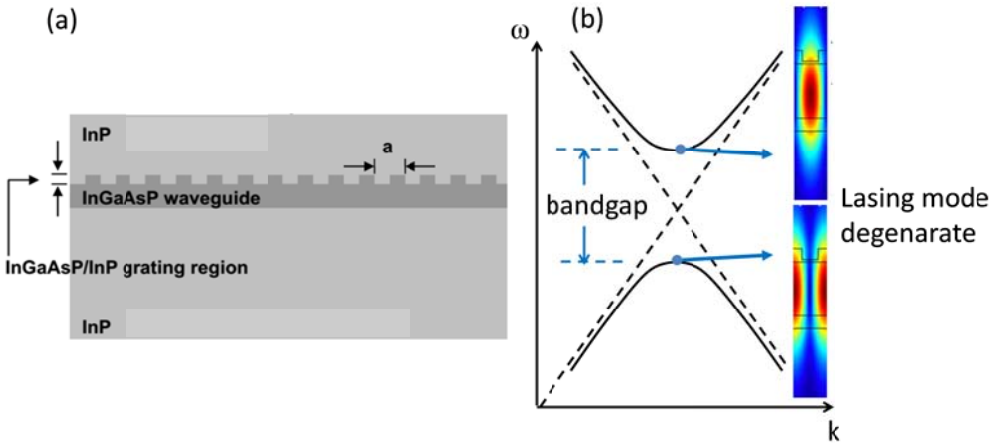

Figure 4.2, (a) Schematic of a buried DFB grating. (b) photonic band structure of a buried DFB grating and the mode profile of the two degenerate band edge modes

The photonic band structure of conventional DFB grating is shown in Fig. 4.2(a). A bandgap is generated through the coupling between two counter-propagating modes. As a result of coupling, the two modes at the band edge will have lower lasing threshold. One of the two modes will start lasing first. Thus single wavelength lasing is realized. Coupling constant κ defined in section 2.4.5 is proportional to this bandgap and can be given as:

$$\kappa = \frac{\varpi_g n}{2c} \tag{4.1}$$

where ω_g is the bandgap (in frequency), n is the modal index, c is speed of light. This expression is equivalent to the definition in section 2.4.5 for pure index coupled DFB grating. The product of κ and cavity length L is used as a parameter to measure the discrimination of the two band edge modes against other modes. κ is essentially proportional to the grating depth. Typically, κL is designed to be greater than 2.[50] However, if no other discrimination mechanism is introduced, which one out of the two

will lase is unpredictable. It randomly depends on the cleaved facet position[67] and the worst case is that two modes will lase simultaneously as pumping current increases. This mode degeneracy results in uncertainty on lasing wavelength and becomes a critical issue that limits the yield of individual device for array construction. Extra effort is required to solve this problem. In Ref. [67], degeneracy is removed by 1) designing the grating to the overcouple regime, $\kappa L=11$; 2) introducing loss couple component by using different doping level for grating peak and trough region. A yield of 95% was achieved by applying these additional engineering steps. The drawbacks of using overcoupled grating is very long laser cavity (3.5mm) and low slope efficiency.

4.2.2 Surface DFB grating coupling mechanism

In our device, we use surface DFB gratings instead. Gratings are fabricated on top of the ridge. So, no regrowth is needed. And more importantly, mode degeneracy no longer exists. In a diose laser, grating on the ridge top is not likely to work since mode is confined in the waveguide core and surface corrugation cannot interact with the mode to produce coupling. Surface DFB grating works in the way that surface plasmon mode bounded to the top contact metal serves as an intermediator to couple two counter-propagating modes and generate a stopband like conventional DFB does. For this surface grating to work, two conditions have to be satisfied: TM polarized light and longer wavelength (mid-IR or longer). Mid-IR QCLs meet both requirements.

Theory of surface grating was clarified in Ref [74] . Surface DFB grating is a periodic corrugation of metal built into the laser cladding layer, as shown in Fig. 4.4. The critical part is the role of surface plasmon mode in this surface grating. Surface plasmons (SPs) are well known as a surface wave exists at the interface between metal and

dielectric interface. Its E-field is predominantly polarized perpendicular to the interface, so it interacts only with TM polarized light. In a diode laser, light is TE polarized so surface grating is not applicable. For a QCL, as a result of transition selection rule, light generated through intersubband transition is TM polarized and could interact with surface plasmon.

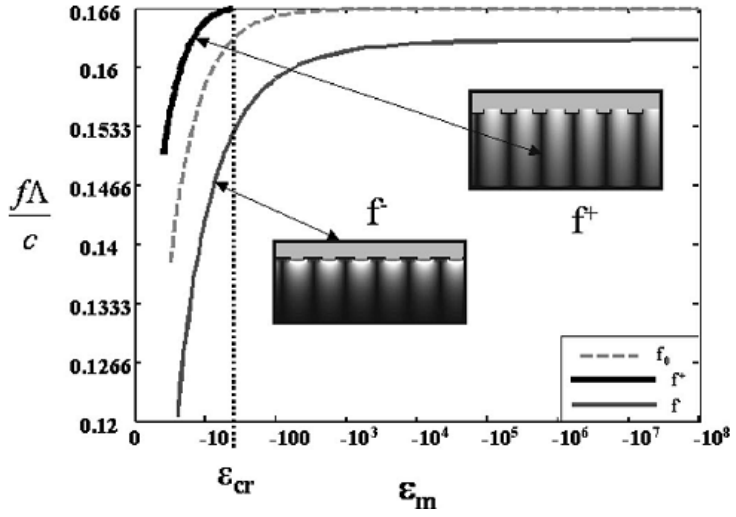

;

Figure 4.3, Dispersion of f^+ and f^- vs dielectric permittivity. Dashed line is the corresponding frequency of a surface plasmon on a flat metal. Insets are mode profiles of f^+ and f^-. Adapted from Ref. [74]

If a periodic structure is fabricated into the metal surrounded by homogeneous dielectric material, in principle, a stopband will form for SP modes, which is similar to DFB grating in a dielectric medium. Fig. 4.3 shows E-field intensity of the two eigenmodes f^+ and f^- of a metal grating in a homogeneous dielectric material. As expected, their E-fields are localized to grating peaks and grating troughs respectively. Fig. 4.3 also plots the frequencies of these two modes as a function of metal permittivity for a fixed grating depth. It shows that beyond a certain value of ε_m, f^+ mode disappears, which corresponds to an unbounded solution. The entire mid-IR range is in this high $|\varepsilon_m|$

region. Consequently, only f^- remains in the mid-IR range. Only one remaining plasmon mode simplifies the interaction between waveguide mode and plasmon mode. The missing f^+ mode eventually leads to the non-degeneracy for wavelength selection.

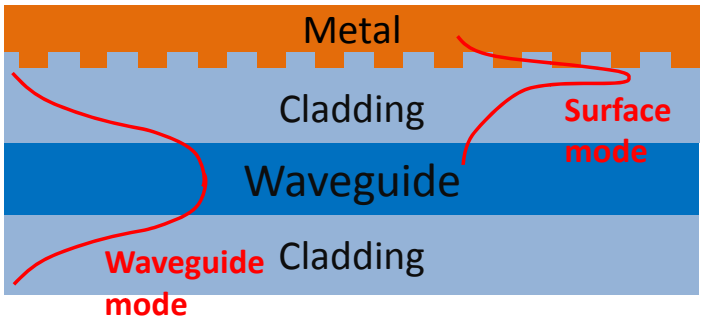

Figure 4.4, Schematic of a surface DFB grating structure, showing the surface mode and waveguide mode

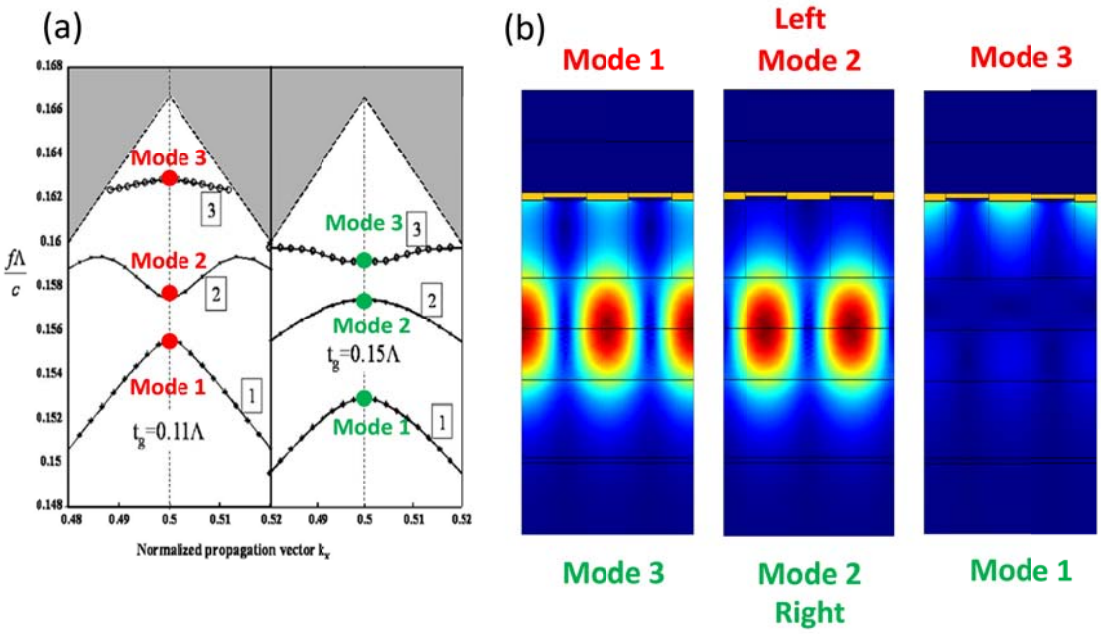

Figure 4.5, (a) photonic band structure for surface DFB structure with two different grating depth, Adapted from Ref. [74] (b) mode profile of the three band edge modes indicated in (a)

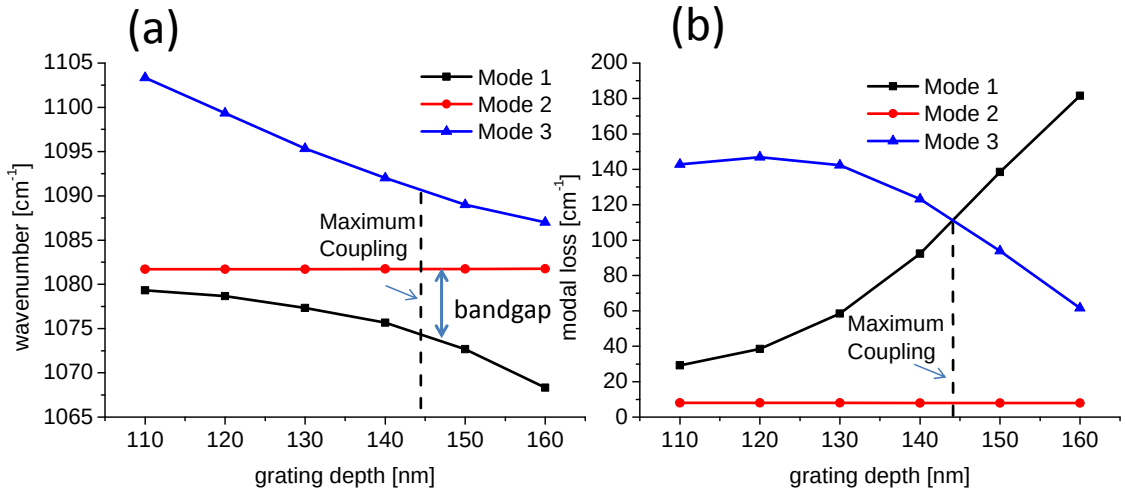

Figure 4.6, (a) typical dependence of the band edges mode frequencies on grating depth (b) band edge modal loss versus grating depth. Dashed line corresponds to the maximum coupling condition

As shown in Fig. 4.4, if a waveguide structure is introduced instead of a homogenous medium, a waveguide mode will come into interaction with the surface plasmon mode. Interaction between them results in distinct property. Simulated photonic band structures for different grating depth are shown in Fig. 4.5(a). Three modes are found at the edge of Brillouin zone. Mode profile is plotted in Fig. 4.5(b). Typical dependence of the band edges mode frequencies and their modal loss on grating depth are plotted in Fig. 4.6(a) and (b), respectively. Regarding the E-field maxima, the lowest frequency mode 1 and highest frequency mode 3 are localized at the grating peaks. The intermediate frequency mode 2 is localized at the grating trough. Mode 2 is confined in the guiding layer and its frequency almost remains constant as grating depth changes. In contrast, mode 1 and mode 3 show different behavior. The physical interpretation as follows: Mode 3 and mode 1 result from the symmetric and antisymmetric coupling of the f^{-} surface mode with the waveguide mode. The strength of interaction changes with

grating depth. With shallow grating depth mode 3 is more like a surface mode and has larger frequency difference relative to mode 2 while mode 1 has more waveguide mode component and its frequency is closer to mode 2. Beyond a certain point, they swap. Due to the absence of f^{+}, mode 2 does not have surface mode component and behaves like a normal waveguide mode. Due to the high loss of surface component, modal loss of mode 1 and 3 is high, as shown in Fig. 4.6(b). Mode 2 becomes the only low loss mode and degeneracy no longer exists. Thus, wavelength selection is achieved by a combination of photonic bandgap and loss discrimination. So surface DFB grating is considered as a complex coupled DFB grating.

4.2.3 Surface DFB grating design

For surface DFB grating, coupling constant κ can be defined in similar manner as buried grating. Surface grating photonic band structure shows two bandgaps (Fig. 4.5 & 4.6): bandgap between mode 1 and 2 ω_{g12} and bandgap between 2 and 3 ω_{g23}, we can define bandgap $\omega_{g,surf}$ as:

$$\omega_{g,surf} = \min\{\omega_{g12},\omega_{g23}\} \tag{4.2}$$

and

$$\kappa_{surf} = \frac{\varpi_{g,surf} n}{2c} \tag{4.3}$$

$\omega_{g,surf}$ is maximized at the point $\omega_{g12}=\omega_{g23}$. It can be seen from Fig. 4.6(b) that loss discrimination is also maximized at this point. Experiment results also support that devices with greater $\kappa_{surf}L$ has better wavelength selection performance. However, we would like to point out that κ_{surf} here for surface grating is not the same as κ for buried index coupled DFB grating. Quantitative design rule for $\kappa_{surf}L$ is not yet clear for surface DFB grating (κL>2 for buried grating). Due to the complexity, detailed theory is beyond the scope of this thesis and requires further research. Discussion in the following text

relies on the positive correlation between $\omega_{g,surf}$ and wavelength selection capability. $\omega_{g,surf}$ ($\upsilon_{g,surf}$) is used to compare different designs.

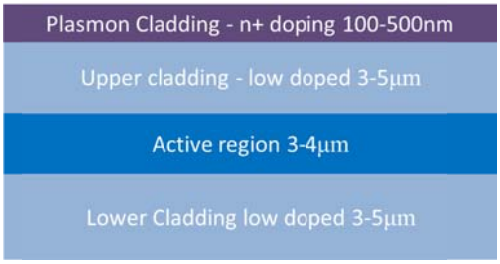

Figure 4.7, (a) Schematic of a typical mid-IR QCL waveguide design.

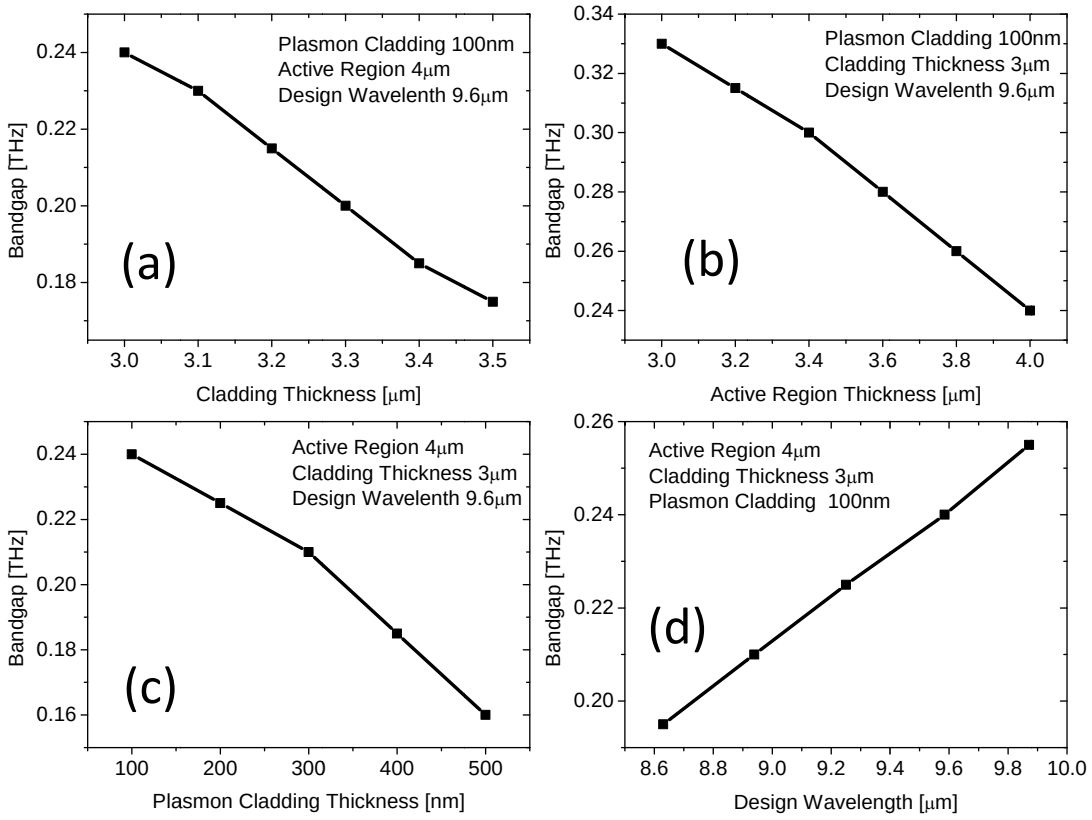

Figure 4.8, Calculated max $\omega_{g,surf}$ of a waveguide design as a function of (a) low doped cladding layer thickness, (b) active region thickness, (c) plasmon cladding thickness, (d) design wavelength

For buried DFB grating, higher grating coupling constant or photonic bandgap can be obtained by increasing grating depth. In contrast, the maximum $\omega_{g,surf}$ a wafer can reach is determined by the epi waveguide design and cannot be altered by wafer processing. Consequently, surface grating coupling strength needs to be taken into account for laser epitaxial design. We studied the dependence of $\omega_{g,surf}$ on waveguide design. A typical mid-IR QCL waveguide structure is shown in Fig. 4.7. Besides the low doped thick cladding layers sandwiching the active region, a highly doped (~10^{18} cm^{-3}) plasmon cladding layer is usually added on top of the upper cladding to push the mode towards the active region in order to reduce free carrier loss generated by metal contact on top. Since bottom cladding layer does not affect the surface grating much, layers requires attention are the active region, upper cladding and plasmon cladding.

Fig. 4.8 is a summary of how the possible maximum $\omega_{g,surf}$ of a waveguide design changes with these various layer thickness. We start from a standard structure with 3μm top and bottom cladding, 4μm active region thickness and 100nm plasmon cladding layer. We target for a design wavelength of 9.6μm and calculate the dependence of photonic bandgap on these parameters. Coupling decreases with increasing cladding layer thickness, plasmon layer thickness and active region thickness. For a fixed design, coupling increases with increasing wavelength. These trends can be explained as follows: Coupling arises from the interaction between surface mode and waveguide mode. Thinner active region, thinner cladding layer and longer wavelength will lead to more evanescent tail outside waveguide core, which tends to enhance the interaction. Plasmon cladding layer serves as a blocking layer for the evanescent tail so that thick layer will degrade coupling. Following these results, 3μm cladding and 100nm plasmon cladding layer is set as standard configuration of our QCLs. Active region thickness is left flexible

for other concerns including continuous wave operation, Cherenkov radiation efficiency of DFG QCL etc.

In the THZ DFG QCL described in the previous chapter and the mid-IR QCL presented in the subsequent section in this chapter, we use the same waveguide design: a 3.3μm active region, a 3μm cladding and a 100nm plamson layer. The mode frequency and modal loss dependence on grating depth are already plotted in Fig. 4.6. Grating depth is always targeted at 145nm. Grating length is set to be longer than 1.2mm for one grating period. Experimental results show that 1.2mm grating is long enough to ensure almost 100% yield on wavelength selection with 20dB side mode suppression ratio.

4.3 LONGITUDINAL INTEGRATION

Far field of an array source spreads over a broad angle. For a number of applications for QCL arrays, it is important to have a compact far-field. Overlapping the beams in the far field has been successfully demonstrated using wavelength beam combining with a suitable grating.[75] However, these systems are as complex as the external cavity tuning setup. With the surface DFB grating and independent gain control scheme, we see the possibility to integrate multiple wavelengths in one ridge and selecting the wavelength by changing current pumping condition. This integration is expected to significantly reduce the far field span of an array source. The ultimate goal is to integrate all wavelengths in an array into one ridge so as to achieve single lobe far field.

4.3.1 Array of 10 dual-single-mode mid-IR QCLs

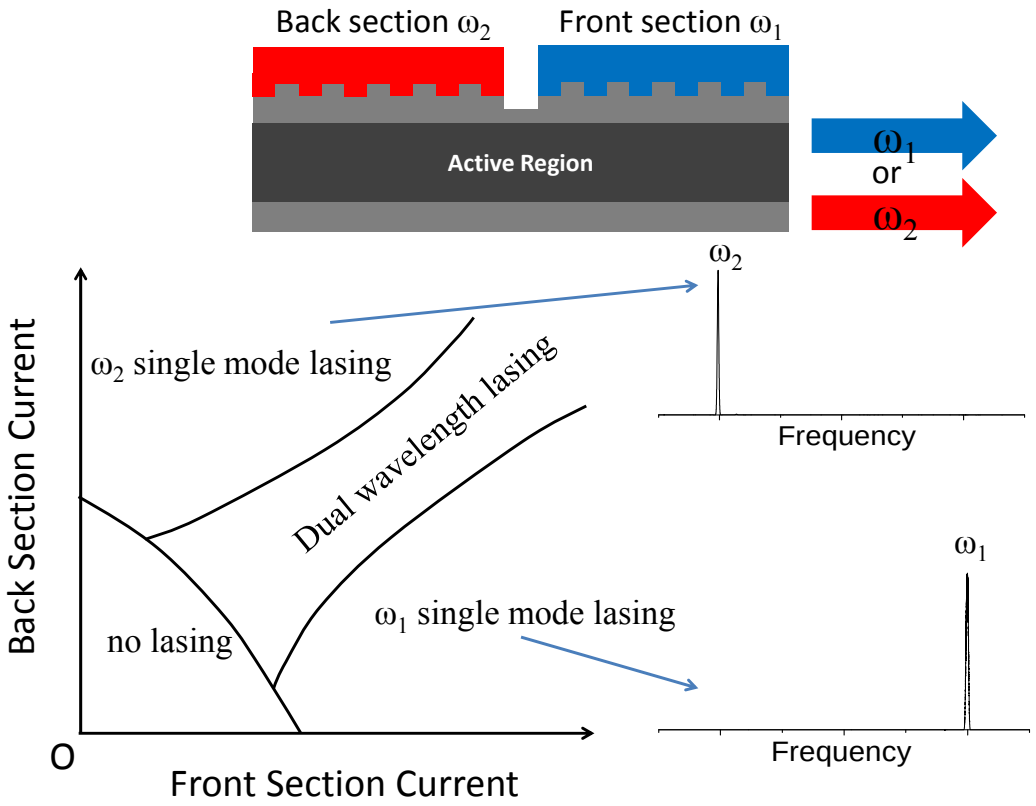

Figure 4.9, Schematic showing three different lasing mode regions on I_{front}-I_{back} plane. Lasing spectra of two indicated single mode region are plotted o the right. Depending on pumping condition, device structure shown on the top can emit either ω_1 or ω_2.

During the independent pumping testing of THz DFG QCL, we observed that depending on pumping condition the laser could be operated under three different modes: dual wavelength lasing, ω_1 single mode lasing and ω_2 single mode lasing. A typical partition of lasing modes on I_{front} (front section current) I_{back} (back section current) 2D plane is shown in Fig. 4.9. By controlling the current flow, one device is able to be operated in two different single modes. In the following text, we call this dual-single-mode QCL. We followed this idea and fabricated a 10 dual-single-mode mid-IR QCL

array. This array can emit 20 different wavelengths to cover a 100 cm^{-1} spectral range with 5 cm^{-1} spacing.

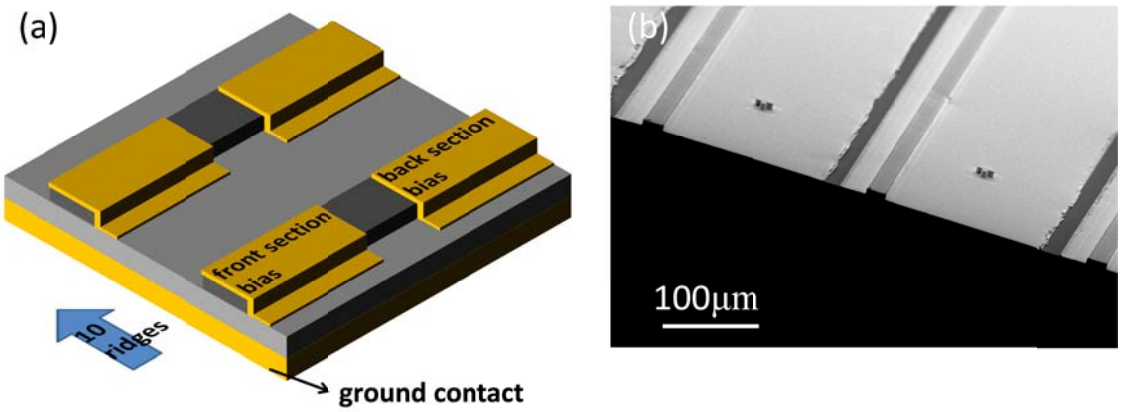

Figure 4.10, (a) Schematic of a 10-ridge dual-single-mode QCL array (only two ridges are shown). (b) SEM image of the fabricated QCL array

Fig. 4.10 shows the schematic and an SEM image of the array. Individual device structure (Fig. 4.9) is similar to the DFG QCL device except for a ground contact configuration. The array consists of ten 22-μm-wide ridge-waveguide QCLs, each ridge designed to emit two mid-IR wavelengths. The wafer epi design is same to the DFG QCL except that it is on a highly doped substrate. Substrate backside contact is used as a common anode and cathodes are made to the ridge top. All devices are based on surface DFB grating. The gratings are defined in the top cladding layer and are approximately 145 nm deep. For each device, the grating in the front section of the device is designed for short wavelength (from 1050cm^{-1} to 1100cm^{-1} with 5cm^{-1} spacing) and the grating at the back section is designed for long wavelength (from 1000cm^{-1} to 1050cm^{-1} with 5cm^{-1} spacing). So the entire array covers from 1000cm^{-1} to 1100cm^{-1}. Each grating section is 1.2-mm-long and the two sections are separated by a 300 μm gap for electrical isolation. An array of ridge waveguide devices is fabricated. Devices are tested at room-

temperature with 70 ns current pulses at 50 kHz repetition frequency. Independent pumping setup is same as the DFG QCL. Current is provided by one pulser and controlled by two RF attenuators. Mid-IR power are measured using thermopile from the front facet using two 2-inch-diameter off-axis parabolic-mirrors setup same as DFG QCL measurement. Recorded mid-IR power is corrected for an estimated 70% collection efficiency of our setup. Fourier-transform infrared spectrometer (FTIR) is used for spectral measurements.

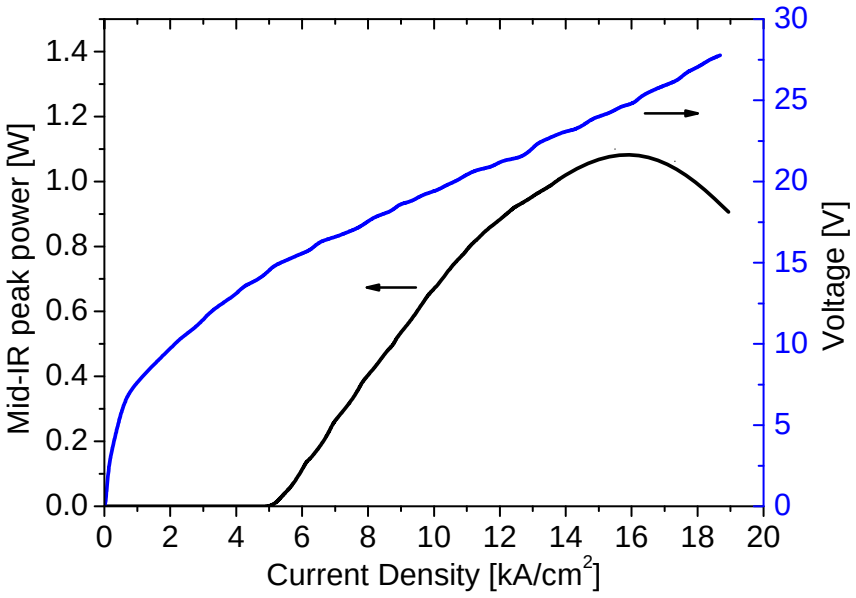

Figure 4.11, L-I-V characteristic of one device in the array

Fig. 4.11 shows the L-I-V characteristics of a device in the array. Maximum output peak power from one facet is over 1W. Fig. 4.12 shows the spectra and peak power of these 20 different wavelengths. 2D scan over the I_{front}-I_{back} plane is performed to each device to find two single modes. 20 single modes are obtained with 100% yield. The peak power and spectra are measured at the point the corresponding single mode power is maximized while the other mode is not lasing. Spectra emitted from the same ridge are

plotted in same color. Front section mode is plotted in dashed line while back section mode is plotted in solid line. Output power of these wavelengths has strong variation. A number of factors including gain spectrum, facet position, grating parameter etc. could affect the output power.

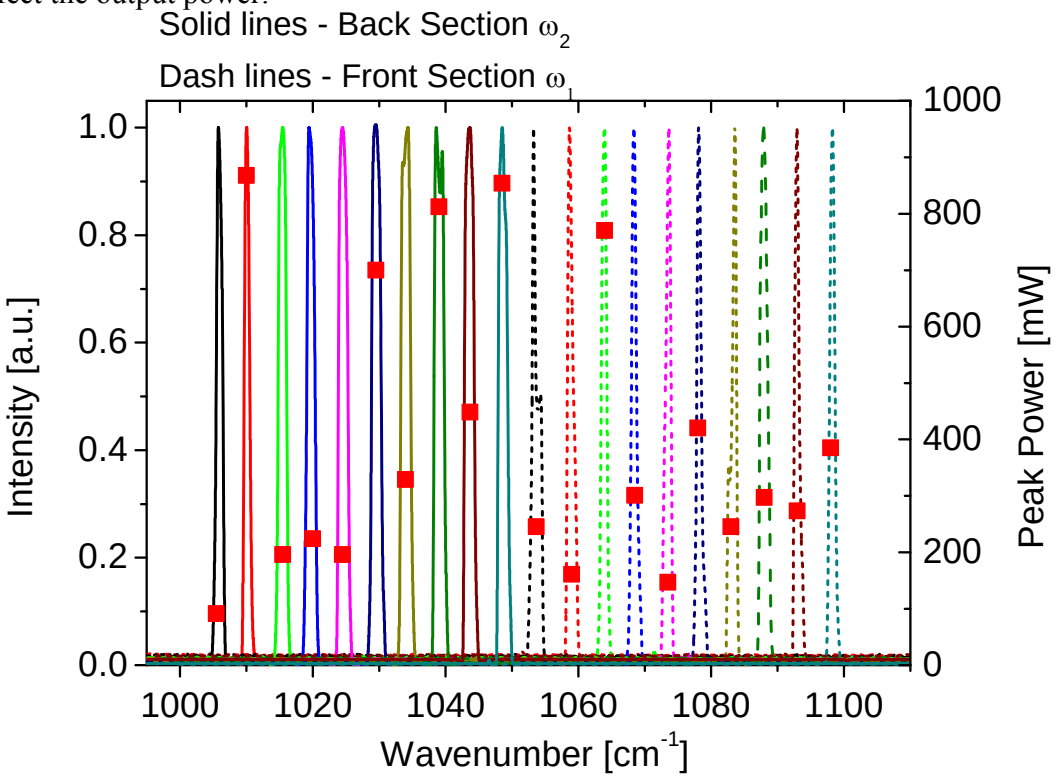

Figure 4.12, Mid-IR lasing spectra and peak power (red squares) for all 20 wavelengths. Spectra and power are recorded when the corresponding single mode emission line power is maximized. Spectra collected from the same ridge are plotted in same color. Mode selected by front section is plotted in dashed line while mode selected by back section is plotted in solid line.

4.3.2 Longitudinal integration of multiple grating sections

Based on this dual single mode result, we can extend this two-section configuration to more sections. This idea becomes practical only with surface grating.

Because with surface grating, cavity length of each section is much shorter (1.2mm) compared to buried rating (3.5mm). Even shorter section length is possible with modified grating and waveguide design. As show in Fig. 4.13(a), n sections with different grating periods can be fabricated in series on one ridge. They are electrically isolated by etching a gap in between adjacent sections so that current can be applied independently. Independent pumping scheme is similar to what we did for THz DFG QCL. Only one pulser is needed as current source. Current applied to each section is controlled by RF attenuators as shown in Fig. 4.13(b)

As shown in Fig. 4.13(b), to select the desired wavelength λ_m to lase, current higher than threshold is only applied to the corresponding section. Current below threshold is applied to all other sections to pump the entire device over lasing threshold. Following the discussion in 3.2.2, lasing mode is predominantly localized in the section under higher pumping level. So the wavelength selected by this section will be favored for lasing. Other sections are under lower pumping level so these wavelengths are expected to be suppressed.

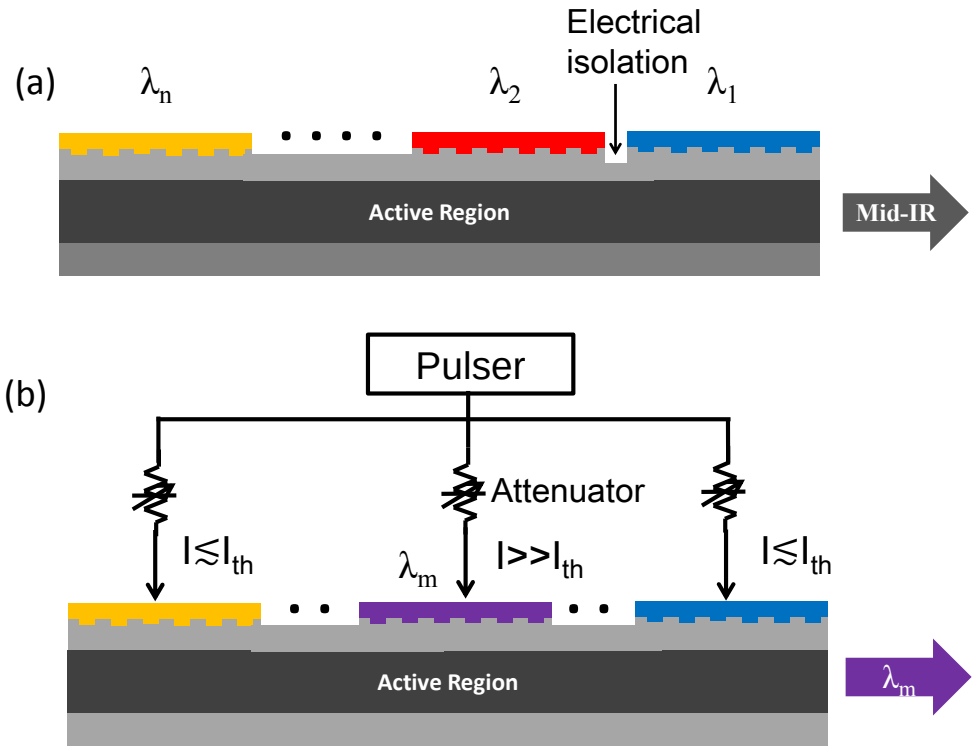

Figure 4.13, (a) Schematic of a n section device. (b) Independent current pumping scheme using RF attenuators and the current pumping condition to select a particular wavelength λ_m

Currently we have demonstrated a three section device. The device ridge is 18μm wide. It consists of three 1.3mm long grating sections separated by two 100μm gaps. Three gratings are designed for three different wavelengths with 35cm^{-1} spacing. The spectra and peak power shown in Fig. 4.14 are measured in the same way as the two-section device. The maximum output of each single mode drops significantly compare to the two-section device. Because with more sections integrated, mode competition among different mode becomes more intense. Single mode can only be obtained slight above the threshold of each section. To boost output power, better grating design or other improvement is required.

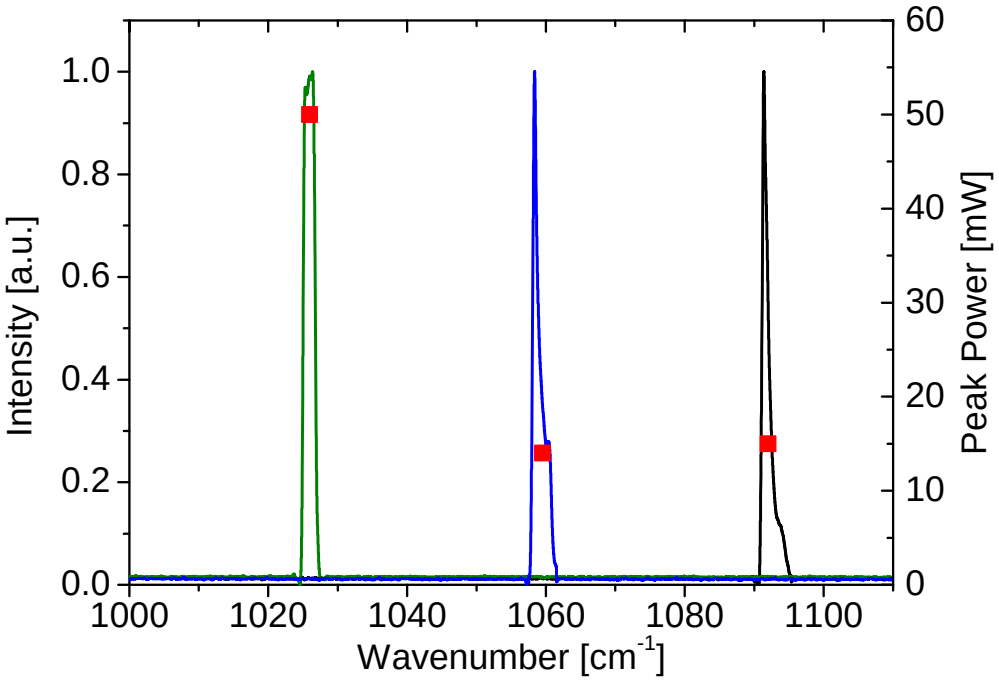

Figure 4.14, Mid-IR lasing spectra and peak power (red squares) of a 3 section device. Spectra and power are measured when corresponding single mode emission line power is maximized.

4.3.3 Summary and future work

To summarize, we proposed a longitudinal integration method of multiple single mode mid-IR QCLs. It is enabled by implementation of surface DFB grating and independent gain control of each grating section. We have demonstrated a dual-section array and a three-section device. Future work would be focused on integrating more sections and boosting output power. Further improvement could be obtained with better waveguide design. There are also other modifications that can improve power like introducing an active amplifying section at the outcoupling facet.

Chapter 5: Conclusion

5.1 SUMMARY

In this dissertation we presented our work on a number of different aspects with emphasis on developing broadly tunable THz semiconductor laser sources. Our experimental study proves variable barrier height active region design to be a viable approach to enhance the design space for THz QCLs. We proposed an external pumping method to improve the current undesirable tunability of THz QCL. Preliminary experimental results support the idea but further improvement on pumping light intensity is required for this method to work. We also developed a widely tunable THz source based on THz DFG QCL array. 10 THz DFG QCL devices are integrated on one chip to cover a wide spectral range. An independent gain control scheme is developed to achieve an almost 100% device yield for array construction. The success of surface DFB grating and independent gain control on THz DFG QCL can also be applied to mid-IR array source. We proposed longitudinal integration of mid-IR QCLs to reduce far field span of array source. Proof-of-principle devices with 2 and 3 sections are demonstrated.

References

[1] A. G. Davies, et al., "Terahertz spectroscopy of explosives and drugs," Materials Today, vol. 11, pp. 18-26, 2008.

[2] C. S. Joseph, et al., "Continuous wave terahertz transmission imaging of nonmelanoma skin cancers," Lasers in Surgery and Medicine, vol. 43, pp. 457-462, 2011.

[3] P. Lancaster, et al., "Surfing the spectrum–what is on the horizon?," British dental journal, vol. 215, pp. 401-409, 2013.

[4] P. F. Taday, "Applications of terahertz spectroscopy to pharmaceutical sciences," Philosophical Transactions of the Royal Society of London A: Mathematical, Physical and Engineering Sciences, vol. 362, pp. 351-364, 2004.

[5] A. Gowen, et al., "Terahertz time domain spectroscopy and imaging: emerging techniques for food process monitoring and quality control," Trends in Food Science & Technology, vol. 25, pp. 40-46, 2012.

[6] C. Jördens and M. Koch, "Detection of foreign bodies in chocolate with pulsed terahertz spectroscopy," Optical Engineering, vol. 47, pp. 037003-037003-5, 2008.

[7] P. H. Siegel, "THz instruments for space," Antennas and Propagation, IEEE Transactions on, vol. 55, pp. 2957-2965, 2007.

[8] S. Koenig, et al., "Wireless sub-THz communication system with high data rate," Nature photonics, vol. 7, pp. 977-981, 2013.

[9] L. A. Samoska, "An overview of solid-state integrated circuit amplifiers in the submillimeter-wave and THz regime," Terahertz Science and Technology, IEEE Transactions on, vol. 1, pp. 9-24, 2011.

[10] W. Steyaert and P. Reynaert, "A 0.54 THz signal generator in 40 nm bulk CMOS with 22 GHz tuning range and integrated planar antenna," 2014.

[11] H. Eisele, "State of the art and future of electronic sources at terahertz frequencies," Electronics letters, vol. 46, pp. 8-11, 2010.

[12] M. Tonouchi, "Cutting-edge terahertz technology," Nature photonics, vol. 1, pp. 97-105, 2007.

[13] G. K. Kitaeva, "Terahertz generation by means of optical lasers," Laser Physics Letters, vol. 5, p. 559, 2008.

[14] Y. J. Ding, "High-power tunable terahertz sources based on parametric processes and applications," Selected Topics in Quantum Electronics, IEEE Journal of, vol. 13, pp. 705-720, 2007.

[15] M. Scheller, et al., "Room temperature continuous wave milliwatt terahertz source," Optics Express, vol. 18, pp. 27112-27117, 2010.

[16] E. B. Petersen, et al., "Efficient parametric terahertz generation in quasi-phase-matched GaP through cavity enhanced difference-frequency generation," Applied physics letters, vol. 98, p. 121119, 2011.

[17] J. Faist, et al., "Quantum cascade laser," Science, vol. 264, pp. 553-556, 1994.

[18] R. Köhler, et al., "Terahertz semiconductor-heterostructure laser," Nature, vol. 417, pp. 156-159, 2002.

[19] S. Fathololoumi, et al., "Terahertz quantum cascade lasers operating up to∼ 200 K with optimized oscillator strength and improved injection tunneling," Optics Express, vol. 20, pp. 3866-3876, 2012.

[20] B. S. Williams, et al., "Operation of terahertz quantum-cascade lasers at 164 K in pulsed mode and at 117 K in continuous-wave mode," Opt. Express, vol. 13, pp. 3331-3339, 2005.

[21] L. Li, et al., "Terahertz quantum cascade lasers with> 1 W output powers," Electronics letters, vol. 50, pp. 309-311, 2014.

[22] B. S. Williams, et al., "High-power terahertz quantum-cascade lasers," Electronics letters, vol. 42, pp. 89-91, 2006.

[23] M. A. Belkin, et al., "Terahertz quantum-cascade-laser source based on intracavity difference-frequency generation," Nature photonics, vol. 1, pp. 288-292, 2007.

[24] M. A. Belkin, et al., "Room temperature terahertz quantum cascade laser source based on intracavity difference-frequency generation," Applied physics letters, vol. 92, p. 201101, 2008.

[25] K. Vijayraghavan, et al., "Terahertz sources based on Čerenkov difference-frequency generation in quantum cascade lasers," Applied physics letters, vol. 100, p. 251104, 2012.

[26] K. Vijayraghavan, et al., "Broadly tunable terahertz generation in mid-infrared quantum cascade lasers," Nature Communications, vol. 4, 2013.

[27] Q. Lu, et al., "Continuous operation of a monolithic semiconductor terahertz source at room temperature," Applied physics letters, vol. 104, p. 221105, 2014.

[28] Q. Qin, et al., "MEMS-based tunable terahertz wire-laser over 330 GHz," Optics letters, vol. 36, pp. 692-694, 2011.

[29] Y. Jiang, et al., "External cavity terahertz quantum cascade laser sources based on intra-cavity frequency mixing with 1.2–5.9 THz tuning range," Journal of Optics, vol. 16, p. 094002, 2014.

[30] M. Helm, Long wavelength infrared emitters based on quantum wells and superlattices vol. 6: CRC Press, 2000.

[31] S. Kumar, "Development of terahertz quantum-cascade lasers," Massachusetts Institute of Technology, 2007.

[32] R. Kazarinov and R. Suris, "Possibility of the amplification of electromagnetic waves in a semiconductor with a superlattice," 1971.

[33] B. S. Williams, "Terahertz quantum-cascade lasers," Nature photonics, vol. 1, pp. 517-525, 2007.

[34] A. Jiang, et al., "Experimental investigation of terahertz quantum cascade laser with variable barrier heights," Journal of Applied Physics, vol. 115, p. 163103, 2014.

[35] M. A. Belkin, et al., "Terahertz quantum cascade lasers with copper metal-metal waveguides operating up to 178 K," Optics Express, vol. 16, pp. 3242-3248, 2008.

[36] S. Kumar, et al., "186 K operation of terahertz quantum-cascade lasers based on a diagonal design," Applied physics letters, vol. 94, pp. 131105-131105-3, 2009.

[37] A. Mátyás, et al., "Temperature performance analysis of terahertz quantum cascade lasers: Vertical versus diagonal designs," Applied physics letters, vol. 96, pp. 201110-201110-3, 2010.

[38] A. Matyas, et al., "Improved terahertz quantum cascade laser with variable height barriers," Journal of Applied Physics, vol. 111, pp. 103106-103106-6, 2012.

[39] C. Jirauschek and P. Lugli, "Limiting factors for high temperature operation of THz quantum cascade lasers," physica status solidi (c), vol. 5, pp. 221-224, 2008.

[40] G. Scalari, et al., "Step well quantum cascade laser emitting at 3 THz," Applied physics letters, vol. 94, p. 041114, 2009.

[41] W. Freeman and G. Karunasiri, "Nonequilibrium electron leakage in terahertz quantum cascade structures," Physical Review B, vol. 85, p. 195326, 2012.

[42] M. Henini, Molecular beam epitaxy: from research to mass production: Newnes, 2012.

[43] C. Sirtori, et al., "Resonant tunneling in quantum cascade lasers," Quantum Electronics, IEEE Journal of, vol. 34, pp. 1722-1729, 1998.

[44] F. Lu, et al., "Tip-enhanced infrared nanospectroscopy via molecular expansion force detection," Nature photonics, vol. 8, pp. 307-312, 2014.

[45] S. Kumar, et al., "Surface-emitting distributed feedback terahertz quantum-cascade lasers in metal-metal waveguides," Optics Express, vol. 15, pp. 113-128, 2007.

[46] A. W. M. Lee, et al., "Tunable terahertz quantum cascade lasers with external gratings," Optics letters, vol. 35, pp. 910-912, 2010.

[47] Q. Qin, et al., "Tuning a terahertz wire laser," Nature photonics, vol. 3, pp. 732-737, 2009.

[48] S. Suchalkin, et al., "Optically tunable long wavelength infrared quantum cascade laser operated at room temperature," Applied physics letters, vol. 102, p. 011125, 2013.

[49] C. Hwang, "Doping Dependence of Hole Lifetime in n‐Type GaAs," Journal of Applied Physics, vol. 42, pp. 4408-4413, 1971.

[50] H. Kogelnik and C. Shank, "Coupled‐wave theory of distributed feedback lasers," Journal of Applied Physics, vol. 43, pp. 2327-2335, 1972.

[51] S. Jung, et al., "Broadly tunable monolithic room-temperature terahertz quantum cascade laser sources," Nature Communications, vol. 5, 2014.

[52] A. Jiang, et al., "Widely tunable terahertz source based on intra-cavity frequency mixing in quantum cascade laser arrays," Applied physics letters, vol. 106, p. 261107, 2015.

[53] R. W. Boyd, Nonlinear optics: Academic press, 2003.

[54] C. Sirtori, et al., "Far‐infrared generation by doubly resonant difference frequency mixing in a coupled quantum well two‐dimensional electron gas system," Applied physics letters, vol. 65, pp. 445-447, 1994.

[55] Y. Jiang, et al., "Two-Dimensional Pump Frequency Study of THz Generation in Mid-Infrared Quantum Cascade Lasers," in CLEO: Science and Innovations, 2015, p. STu1G. 5.

[56] Q. Lu, et al., "Room temperature terahertz quantum cascade laser sources with 215 μW output power through epilayer-down mounting," Applied physics letters, vol. 103, p. 011101, 2013.

[57] Q. Lu, et al., "Room temperature single-mode terahertz sources based on intracavity difference-frequency generation in quantum cascade lasers," Applied physics letters, vol. 99, p. 131106, 2011.

[58] Q. Lu, et al., "Widely tunable room temperature semiconductor terahertz source," Applied physics letters, vol. 105, p. 201102, 2014.

[59] S. Slivken, et al., "Sampled grating, distributed feedback quantum cascade lasers with broad tunability and continuous operation at room temperature," Applied physics letters, vol. 100, p. 261112, 2012.

[60] T. S. Mansuripur, et al., "Widely tunable mid-infrared quantum cascade lasers using sampled grating reflectors," Optics Express, vol. 20, pp. 23339-23348, 2012.

[61] M. Carras, et al., "Top grating index-coupled distributed feedback quantum cascade lasers," Applied physics letters, vol. 93, p. 011109, 2008.

[62] B. John, "Electrical Circuit Theory and Technology," Linocre House, Jordan Hill, Oxford OX2 8DP, vol. 200, pp. 391-395, 2003.

[63] L. A. Coldren, et al., Diode lasers and photonic integrated circuits vol. 218: John Wiley & Sons, 2012.

[64] P. Rauter, et al., "High-power arrays of quantum cascade laser master-oscillator power-amplifiers," Optics Express, vol. 21, pp. 4518-4530, 2013.

[65] E. Mujagic, et al., "Two-dimensional broadband distributed-feedback quantum cascade laser arrays," Applied physics letters, vol. 98, pp. 141101-141101-3, 2011.

[66] P. Jouy, et al., "Surface emitting multi-wavelength array of single frequency quantum cascade lasers," Applied physics letters, vol. 106, p. 071104, 2015.

[67] B. G. Lee, et al., "DFB quantum cascade laser arrays," Quantum Electronics, IEEE Journal of, vol. 45, pp. 554-565, 2009.

[68] S. Slivken, et al., "Extended electrical tuning of quantum cascade lasers with digital concatenated gratings," Applied physics letters, vol. 103, p. 231110, 2013.

[69] R. Maulini, et al., "External cavity quantum-cascade lasers tunable from 8.2 to 10.4 m using a gain element with a heterogeneous cascade," Appl. Phys. Lett, vol. 88, p. 201113, 2006.

[70] G. Wysocki, et al., "Widely tunable mode-hop free external cavity quantum cascade lasers for high resolution spectroscopy and chemical sensing," Applied Physics B, vol. 92, pp. 305-311, 2008.

[71] K. Fujita, et al., "Broad-gain ($\Delta\lambda/\lambda$ 0~ 0.4), temperature-insensitive (T 0~ 510K) quantum cascade lasers," Optics Express, vol. 19, pp. 2694-2701, 2011.

[72] K. Fujita, et al., "High-performance quantum cascade lasers with wide electroluminescence (~ 600 cm− 1), operating in continuous-wave above 100° C," Applied physics letters, vol. 98, p. 231102, 2011.

[73] B. G. Lee, et al., "Widely tunable single-mode quantum cascade laser source for mid-infrared spectroscopy," Applied physics letters, vol. 91, p. 231101, 2007.

[74] M. Carras and A. De Rossi, "Photonic modes of metallodielectric periodic waveguides in the midinfrared spectral range," Physical Review B, vol. 74, p. 235120, 2006.

[75] B. G. Lee, et al., "Beam combining of quantum cascade laser arrays," Optics Express, vol. 17, pp. 16216-16224, 2009.